

Master's thesis

2020

Jon A. Selnes

Master's thesis

NTNU
Norwegian University of
Science and Technology
Faculty of Natural Sciences
Department of Chemical Engineering

Jon A. Selnes

NiCo₂O₄ Catalyst on Commercial Low Surface Area and Synthesized High Surface Area CeO₂ For Catalytic Methane Abatement in Natural Gas Engines

June 2020



Norwegian University of
Science and Technology

NiCo₂O₄ Catalyst on Commercial Low Surface Area and Synthesized High Surface Area CeO₂ For Catalytic Methane Abatement in Natural Gas Engines

Jon A. Selnes

Chemical Engineering and Biotechnology

Submission date: June 2020

Supervisor: Hilde Johnsen Venvik, IKP

Co-supervisor: Jia Yang, IKP

Norwegian University of Science and Technology
Department of Chemical Engineering

Preface

This master's thesis is written in connection with the final year of the chemical engineering program at the Norwegian University of Science and Technology.

First, I would like to thank my supervisor, Professor Hilde Venvik, for her guidance and facilitation during the master period. I also want to thank my co-supervisor, Associated Professor Jia Yang, who has been very helpful in interpreting the experimental results. Moreover, I would also like to thank SINTEF researcher, Shirley Elisabeth Liland, for her correction of my results. In addition, I would like to thank Ph.d student, Junbo Yu, for his help with calibrating the LFC controller as well as facilitate the water injection system.

Finally, I would like to thank all the people around me who have made it possible for me to complete the study. Though, a special thanks to Ina K. Pedersen who has been very supportive over the past years.

Declaration of Compliance

I declare that this master's thesis is the result of independent work in accordance with the examination regulations at the Norwegian University of Science and Technology.

Trondheim, Norway

June 11, 2020



Jon Arve Selnes

Abstract

Greater utilization of natural gas as a marine fuel is seen as a possible part of the global, but also national, solution to reduce greenhouse gas emissions. However, this assumes that excess methane, which is not burned, is handled in an exhaust gas treatment system that converts it into CO₂. For this to succeed, it is necessary to develop a catalyst suitable for oxidation of methane at relatively low temperatures as well as in low concentrations. Moreover, challenging reaction conditions associated with a steam content up to 15 % of the feed must be surpassed. NiCo₂O₄ has previously shown good results in relation to this. However, to make better use of the catalyst, it has been attempted to use a support material that maintains the positive properties of NiCo₂O₄ while the material cost remains relatively low.

In this master thesis NiCo₂O₄ supported on low- and high surface area CeO₂ were investigated in relation to catalytic oxidation of methane. The catalytic activity was compared under dry and wet reaction conditions as well as in relation to pure NiCo₂O₄. Furthermore, high surface area CeO₂/H were synthesized through a Sol-gel based method suitable to produce support material of desired specifications without the use of a template. In addition, all the catalysts synthesized were impregnated according to the IWI impregnation method. The morphological properties of the catalysts and carrier materials were characterized by XRD, Raman spectroscopy, TPR, TGA and N₂-physorption.

From the experiments performed, it was found that the results obtained in the specialization project were reproducible, and that NiCo oxides achieve much higher activity when supported on CeO₂, regardless of the support structure. In addition, NiCo₂O₄ supported by low surface area CeO₂ shown to have high temperature stability and activity under dry reaction conditions. Furthermore, the results of NiCo₂O₄ synthesized on high surface area CeO₂ showed somewhat increased activity in favour of catalysts supported on low surface area CeO₂. However, in contrast the same catalyst showed signs of lower temperature stability and deactivation due to sintering. Activity experiments with wet reaction conditions revealed irreversible deactivation of the catalysts, most likely caused by structural changes of the support. In addition, comparison of supported-and unsupported NiCo₂O₄ suggested higher activity in favour of supported NiCo oxides. Moreover, the bulk activity of NiCo₂O₄ on high and low surface area CeO₂ showed greater NiCo oxide utilization on low surface area support. Based on this and the XRD result it was suggested that an unknown interaction between CeO₂ and NiCo₂O₄, that has not yet been studied, cause nearly equal dispersion of NiCo oxides on CeO₂ regardless of support structure. Conclusively, the results obtained were promising in terms of activity and stability with respect to catalytic oxidation of excess methane from LNG driven vessels.

Sammendrag

Større utnyttelse av naturgass som marint brensel blir sett på som en mulig del av den globale, men også nasjonale løsningen med tanke på å redusere utslipp av klimagasser. Dette forutsetter midlertidig at overskuddsmetan som ikke forbrennes omdannes til CO_2 ved hjelp av etterbehandling av avgassene. For at dette skal være mulig er det nødvendig å utvikle en katalysator som egner seg til oksidasjon av metan ved relative lave temperaturer samt ved små konsentrasjoner og under utfordrende reaksjonsforhold der innholdet av vanddamp er opptil 15 % av føden. NiCo_2O_4 har tidligere vist gode resultater i forhold til dette. Men for å utnytte katalysatoren bedre har det blitt forsøkt å benytte et støttemateriale som opprettholder de positive egenskapene til NiCo_2O_4 samtidig som at materialkostnadene ikke øker.

I denne masteroppgaven har NiCo_2O_4 støttet på lavt- og høyt overflate areal CeO_2 blitt undersøkt i forhold til katalytisk oksidasjon av metan. Den katalytiske aktiviteten ble sammenliknet under tørre og våte reaksjonsbetingelser samt satt i relasjon med ren NiCo_2O_4 , og for reproduksjon av resultatene som ble oppnådd under spesialiserings prosjektet høsten 2019. Videre så ble høyt overflateareal CeO_2/H syntetisert gjennom en Sol-gel basert metode som var egnet til å produsere bærer materiale med ønskede spesifikasjoner uten bruk av templat. I tillegg ble alle katalysatorene som ble syntetisert impregnert ved hjelp av IWI-impregneringsmetoden. De morfologiske egenskapene til katalysatorene og bærer materialene ble karakterisert ved hjelp av XRD, Raman spektroskopi, TPR, TGA og N_2 -physisorption.

Fra de forsøkene som ble utført, ble det funnet at resultatene som ble oppnådd i spesialiseringsprosjektet lot seg reproducere, og at NiCo oksider får økt aktivitet når de er syntetisert på CeO_2 , uavhengig av støttens struktur. I tillegg ble det vist at NiCo_2O_4 på lavt overflateareal har høy temperaturstabilitet og aktivitet under tørre reaksjonsforhold. Videre viste resultatet fra NiCo_2O_4 syntetisert på høyt overflate areal CeO_2 at aktiviteten til katalysatoren økte noe i forhold til katalysatorer basert på lavt overflateareal CeO_2 . Men det motsatte ble funnet i henhold til temperaturstabilitet, da katalysatoren viste tegn til sintring. Forsøkene som ble utført under våte reaksjonsbetingelser viste at katalysatorene deaktiverte irreversibelt sannsynligvis på grunn av strukturelle endringer i bærer materialet. I tillegg viste sammenlikning av ren-og støttet NiCo_2O_4 at bærer materialet opprettholdt en høyere aktivitet for oksidene i forhold til ren spinell. Videre viste sammenlikningen av bulkaktivitet til NiCo_2O_4 på høyt og lavt overflate areal CeO_2 at oksidene som var støttet av CeO_2/H ikke utnyttet arealet i like stor grad som de som ble støttet av CeO_2/L . Med bakgrunn I dette og XRD resultatene ble det foreslått at det finnes en bindingsmekanisme mellom NiCo oksidene og CeO_2 som enda ikke har blitt studert. Og som medfører nesten lik fordeling av aktivt material på CeO_2 uavhengig av støttens struktur. Basert på de resultatene som ble oppnådd for NiCo_2O_4 støttet på CeO_2 , viser katalysatoren lovende aktivitet og stabilitet med tanke på katalytisk oksidasjon av overskudds metan fra LNG drevende fartøy.

Contents

Preface	II
Abstract	IV
Sammendrag	VI
Abbreviations	XI
List of Symbols	XIII
1. Introduction	1
1.1. Motivation	1
1.2. Objective	2
1.3. Method	3
2. Theory	5
2.1. Natural Gas as Fuel	5
2.2. Catalytic Combustion of Methane	6
2.2.1. Nobel Metal Catalyst	6
2.2.2. Metal Oxide Catalyst	6
2.2.3. Catalyst Morphology	8
2.3. Catalyst Synthesis	10
2.3.1. Incipient Wetness Impregnation	10
2.3.2. Sol-gel Based Synthesis of High Surface Area Mesoporous Ceria	10
2.3.3. Drying and Calcination	11
2.4. Catalytic Characterization	12
2.4.1. X-ray Fluorescence	12
2.4.2. X-ray Diffraction	13
2.4.3. N ₂ -Physisorption	15
2.4.4. Raman Spectroscopy	17
2.4.5. Gas Chromatography	19
2.4.6. Thermogravimetric Analysis	22
2.4.7. Temperature Programmed Reduction	22
2.5. Catalytic Activity	24
2.5.1. Calculation of Methane Conversion	24
2.5.2. Carbon Error	25
2.6. Kinetics	25

3. Experimental	27
3.1. Synthesis of Catalysts and High Surface Area Ceria Support	27
3.2. Characterization	29
3.2.1. X-Ray Fluorescence - Bulk Composition	29
3.2.2. Raman Spectroscopy	29
3.2.3. X-Ray Diffraction – Investigation of Crystalline Phases and Crystal Size . . .	30
3.2.4. N ₂ - Physisorption - Surface Area and Pore Size Distribution	30
3.2.5. TPR	31
3.2.6. TGA - Investigation of Carbon Deposits	32
3.3. Activity Test	33
4. Results	37
4.1. XRF-Composition	37
4.2. N ₂ - Physisorption - BET/BJH	37
4.3. Raman	39
4.4. XRD	40
4.5. TPR	43
4.6. Catalyst Activity	44
4.6.1. Effect of H ₂ O	47
4.7. Raman - Carbon Deposition Studies	53
5. Discussion	54
5.1. Synthesis of Catalysts and Support	54
5.2. High and Low Surface Area CeO ₂ Support Structure	56
5.3. NiCo ₂ O ₄ Catalyst Structure	56
5.4. Catalyst Activity	58
5.4.1. Effect of CeO ₂	58
5.4.2. Reproduction of The Specialization Project Result and Effect of Low Surface Area CeO ₂	59
5.4.3. Effect of High Surface Area CeO ₂	59
5.4.4. Effect of Water	60
5.4.5. Carbon Deposits	61
6. Conclusion	62
7. Further Work	63
Bibliography	66
A. Catalyst Synthesis	I
A.1. Calculation - IWI Impregnation Solution	I
A.2. Deviation Between Nominal and Measured Mass Percentages	III

B. Characterization	IV
B.1. N ₂ - Physisorption	IV
B.2. Raman	VI
B.3. XRD	VIII
B.4. CeO ₂ TPR-Profile	IX
C. Activity Tests	X
C.1. H ₂ O Experiments	XII
C.2. Carbon Balance	XIV
C.3. Calculation of Reaction Rate and Quantitative Analysis	XV
C.4. CeO ₂ Blank Test and Activity Curve	XVI
D. Calibration Curve and Calculation of H₂O Flow	XVII
E. MatLab Script	XVIII
F. Risk Assessment	

Abbreviation	Meaning
BET	N ₂ -Physisorption, Brunauer, Emmett and Teller method
BJH	N ₂ -Physisorption, Barret, Joyner and Halenda method
Eq	Equation
ECD	Electron Capture Detector
FID	Flame Ionization Detector
GC	Gas Chromatography
HSE	Health, Safety and Environment
LBG	Liquefied Bio Gas
LNG	Liquefied Natural Gas
MFC	Mass Flow Controller
MS	Mass spectrometer
NG	Natural Gas
IWI	Incipient Wetness Impregnation
Pd	Palladium
Pt	Platinum
TCD	Thermal Conductivity Detector
TGA	Thermogravimetric Analysis
TPR	Temperature Programmed Reduction
XRD	X-Ray Diffraction
XRF	X-Ray Fluorescence
WCOT	Wall-Coated Open Tubular column
CeO₂	Ceria
CH₄	Methane
CO₂	Carbon Dioxide
γ-Al₂O₃	Gamma-Alumina
H₂O	Water
N₂	Nitrogen
NiCo₂O₄	Nickel Cobalt Spinel
NO_x	Nitroxides
O₂	Oxygen
SO_x	Sulphoxides
SiC	Si-Carbide
ZrO₂	Zirconia

List of Symbols

Symbol	Physical Quantity	Unit
2θ	Angle of diffraction	$^{\circ}$
λ	Air fuel ratio	-
λ	Wavelength	nm
ρ	Density	kg m^{-3}
c_i	Concentration of component i	mol L^{-1}
$c_{i,0}$	Initial concentration of component i	mol L^{-1}
d	Lattice spacing	\AA
E	Energy	kJ or eV
E_C	Carbon Error	in %
E_A	Activation energy	kJ mol^{-1}
F_i	Flowrate of component i	ml min^{-1}
F_{tot}	Total flow rate	ml min^{-1}
GHSV	Gas Hourly Space Velocity	$\text{NmL h}^{-1} \text{g}_{\text{cat}}^{-1}$
h	Height	cm
k	Rate constant	s^{-1}
k_B	Boltzmann's constant	JK^{-1}
L	Length	nm
M	Molarity	mol L^{-1}
Mm	Molecular weight	g mol^{-1}
m	Mass	g
n	Order of Diffraction	-
n_i	Amount of Substance i	mol
p	Pressure	bar / mTorr
p_i	Partial Pressure of component i	bar
q	Volumetric Flow Rate	NmL min^{-1}
r	Reaction Rate	$\text{mol g}_{\text{act.cat}}^{-1} \text{h}^{-1}$
S_{BET}	Specific Surface Area	$\text{m}^2 \text{g}_{\text{cat}}^{-1}$
S_i	Setpoint of component i by MFC	in %
T	Temperature $^{\circ}\text{C}$ or	K
V	Volume	cm^3
V_0	Volume of adsorbed molecules first layer in BET	mm^3
V_m	Volume of one mole of ideal gas	mL
V_P	Pore Volume	$\text{cm}^3 \text{g}_{\text{cat}}^{-1}$
V_{tot}	Total volume of adsorbed molecules	mm^3
X_i	Conversion of component i	in %

y_i Mole fraction of i in gas phase -

List of Figures

2.1.	Illustration of possible reaction pathway for methane on NiCo ₂ O ₄ based catalyst [16].	7
2.2.	Envisioned catalyst with marble structure consisting of low surface area Ceria with no defined pore structure and dispersed NiCo ₂ O ₄ spinel as black dots. The figure is created in Inkscape.	8
2.3.	Illustration of CeO ₂ structure created in Inkscape. Oxygen atoms in tetrahedral structure as well as interaction with Ce atoms in cubic eutaxa.	9
2.4.	Catalytic oxidation of methane illustrated on a surface consisting of CeO ₂ . The Lattice oxygen network shows the oxygen storage capacity of the support. The figure is created in Inkscape.	9
2.5.	Illustration of X-ray emissions pathways created in Inkscape. Starting out with an incoming X-ray beam that leads to ejection of inner electron. The atom stability is obtained either by Auger electron or fluorescence emission [31].	13
2.6.	Lattice scattering of X-rays, information of the crystalline phase is obtained through Bragg's relationship [34].	14
2.7.	Illustration of type IV BET-isotherm created in Inkscape [25].	15
2.8.	Illustration of adsorption-desorption hysteresis H1,H2,H3 and H4 classified according to IUPAC, created in Inkscape [24].	17
2.9.	Illustration of Raman scattering with frequency V_o (Reyleigh band), $V_o - V_{vib}$ (Stokes band) and $V_o + V_{vib}$ (anti-Stokes band). Illustration created in Inkscape [34].	18
2.10.	Simple illustration of Gas Chromatography created with Inkscape	19
2.11.	Illustration of GC peak obtained by analysing gas composition which contain N ₂ , O ₂ and CH ₄	21
2.12.	Reduction mechanism of TPR illustrated by the Nucleation-and Contracting sphere models. Created with Inkscape [44].	23
2.13.	Reduction rate illustration of the shrinking core-and nucleation models. Common to these two models is the reduced reduction rate due to diffusion limitations. The figure is created in Inkscape [34].	24
3.1.	Temperature program used for TPR analysis. Heating rate 10 °C min ⁻¹ from the initiation of reduction steps	31
3.2.	Standard quartz reactor used for temperature programmed reduction analyses.	32
3.3.	Flow sheet over rig 2.9, created in SmartArt.	33
3.4.	Simplified illustration of quartz reactor made in Inkscape	35
3.5.	Temperature program used during activity test. Illustration created in SigmaPlot	36
4.1.	Pore distribution over synthesized high surface area ceria, CeO ₂ /H. measured by N ₂ adsorption desorption at 77.35 K.	38

- 4.2. Raman spectrum of sample 6.6NiCoO/CeO₂/L-S5, 6.5NiCoO/CeO₂/H-S7, CeO₂/H and CeO₂/L. Measurement parameters: Surface accumulation 4, Acc. time 4 min, filter 10 % and hole size = 200. 39
- 4.3. XRD spectre of the samples CeO₂/H and CeO₂/L, where both samples used the following analysis parameters: $2\theta = 15-75^\circ$, time = 60 min, step change = $0.044^\circ\text{step}^{-1}$, permanent slit = 0.3 mm. 40
- 4.4. XRD plot showing the results of the samples 6.5NiCoO/CeO₂/L-S5, 6.5NiCoO/CeO₂/H-S7 and 6.5NiCoO/CeO₂/H-S7*, where * indicates the sample is examined after the 2nd reaction. Cross indicates nickel cobalt oxide identified using PDF 00-002-1074 and PDF 04-019-6381. Analysis parameters: $2\theta = 15-75^\circ$, time = 60 min, step change = $0.044^\circ\text{step}^{-1}$, permanent slit = 0.3 mm. 41
- 4.5. TPR-profile of NiCo₂O₄, and the catalysts supported by high- and low surface area CeO₂. Reaction conditions: H₂/Ar = 7 %, $F_{\text{H}_2/\text{Ar}} = 20 \text{ ml min}^{-1}$, heating rate = $10^\circ\text{C min}^{-1}$, $\text{act.m}_{\text{NiCo}_2\text{O}_4(\text{SINTEF})} = 0.150 \text{ g}$, $\text{act.m}_{6.5\text{NiCoO/CeO}_2/\text{L-S5}} = 0.0108 \text{ g}$ and $\text{act.m}_{6.5\text{NiCoO/CeO}_2/\text{H-S7}} = 0.0127$ 43
- 4.6. Methane conversion curve of samples 6.3 NiCoO/CeO₂/L-S1 and 6.5NiCoO/CeO₂/L-S5. Reaction conditions: $F_{\text{CH}_4} = 4 \text{ ml min}^{-1}$, $F_{\text{N}_2} = 100 \text{ ml min}^{-1}$, $F_{\text{Air}} = 96 \text{ ml min}^{-1}$ 44
- 4.8. Dry and wet reaction cycles of the catalyst 6.6NiCoO/CeO₂/L-S6. Reaction conditions: $F_{\text{CH}_4} = 4 \text{ ml min}^{-1}$, $F_{\text{N}_2} = 80 \text{ ml min}^{-1}$, $F_{\text{Air}} = 96 \text{ ml min}^{-1}$, $F_{\text{H}_2\text{O}} = 20 \text{ ml min}^{-1}$, amount of sample = 0.5036 g, proportion of active material = 0.033 g, p = 1 bar. Reaction conditions Dry: $F_{\text{CH}_4} = 4 \text{ ml min}^{-1}$, $F_{\text{N}_2} = 100 \text{ ml min}^{-1}$, $F_{\text{Air}} = 96 \text{ ml min}^{-1}$, P = 1 bar. 47
- 4.9. Reaction rate, for sample 6.6NiCoO/CeO₂/L-S6, calculated at T = 450 for 2 cycles with H₂O and three without. Reaction conditions Wet: $F_{\text{CH}_4} = 4 \text{ ml min}^{-1}$, $F_{\text{N}_2} = 80 \text{ ml min}^{-1}$, $F_{\text{Air}} = 96 \text{ ml min}^{-1}$, $F_{\text{H}_2\text{O}} = 20 \text{ ml min}^{-1}$, amount of sample = 0.5036 g, proportion of active material = 0.033 g, p = 1 bar. Reaction conditions Dry: $F_{\text{CH}_4} = 4 \text{ ml min}^{-1}$, $F_{\text{N}_2} = 100 \text{ ml min}^{-1}$, $F_{\text{Air}} = 96 \text{ ml min}^{-1}$, P = 1 bar. 48
- 4.10. Comparison of the conversion trend between 6.6NiCoO/CeO₂/L-S6 and pure NiCo₂O₄, under wet reaction conditions. 49
- 4.11. Comparison of activity trend to NiCo₂O₄ supported by high and low surface area CeO₂, under wet reaction conditions. 50
- 4.12. Carbon error plot of sample 6.5NiCoO/CeO₂/L-S5. Reaction conditions: $F_{\text{CH}_4} = 4 \text{ ml min}^{-1}$, $F_{\text{N}_2} = 100 \text{ ml min}^{-1}$, $F_{\text{Air}} = 96 \text{ ml min}^{-1}$, amount of sample = 0.5012 g, proportion of active material = 0.035 g, P = 1 bar. 51
- 4.13. Carbon error plot of sample 6.5NiCoO/CeO₂/H-S7. Reaction conditions: $F_{\text{CH}_4} = 4 \text{ ml min}^{-1}$, $F_{\text{N}_2} = 100 \text{ ml min}^{-1}$, $F_{\text{Air}} = 96 \text{ ml min}^{-1}$, amount of sample = 0.5025 g, proportion of active material = 0.039 g, P = 1 bar. 52
- 4.14. Raman plot of materials SiC, CeO₂, used and unused 6.5NiCoO/CeO₂/L-S5 catalyst. Analysis parameters: Range = 100 - 3000 cm⁻¹, Accumulation = 4, Acc. Time = 4 min, Filter = 10 %, Hole = 200. 53

- B.1. Raman spectrum of sample 6.0NiCoO/CeO₂/L-S3. Analysis parameters: Range = 100 - 3000 cm⁻¹, Accumulation = 4, Acc. Time = 4 min, Filter = 10 %, Hole = 200 . VI
- B.2. Raman spectrum of sample 5.7NiCoO/CeO₂/L-S4. Analysis parameters: Range = 100 - 3000 cm⁻¹, Accumulation = 4, Acc. Time = 4 min, Filter = 10 %, Hole = 200 . VI
- B.3. Raman spectrum of sample 6.6NiCoO/CeO₂/L-S6. Analysis parameters: Range = 100 - 3000 cm⁻¹, Accumulation = 4, Acc. Time = 4 min, Filter = 10 %, Hole = 200 . VII
- B.4. Raman spectrum of sample 6.5NiCoO/CeO₂/L-S5. Measurement parameters: Accumulation 4, Acc. Hour 4 min, filter 10 % and hole 200. VII
- B.5. Raman spectrum of sample 6.5NiCoO/CeO₂/H-S7. Measurement parameters: Accumulation 4, Acc. Hour 4 min, filter 10 % and hole 200. VIII
- B.6. XRD spectre of 6.0NiCoO/CeO₂/L-S3, 5.7NiCoO/CeO₂/L-S4 and 6.6NiCoO/CeO₂/L-S6. Analysis parameters: 2 θ = 15-75 °, time = 60 min, step change = 0.044 °step⁻¹, permanent slit = 0.3 mm. VIII
- B.7. TPR-profile of high and low surface area CeO₂. Reaction conditions: H₂/Ar = 7 %, F_{H₂/Ar} = 20 ml min⁻¹, heating rate = 10 °C min⁻¹ IX
- C.1. Methane conversion curve of sample 6.0NiCoO/CeO₂/L-S3. Reaction conditions: F_{CH₄} = 4 ml min⁻¹, F_{N₂} = 100 ml min⁻¹, F_{Air} = 96 ml min⁻¹, amount of sample = 0.5074 g, P = 1 bar. X
- C.2. Reaction curve of catalyst 5.7NiCoO/CeO₂/L-S4. Reaction conditions: F_{CH₄} = 4 ml min⁻¹, F_{N₂} = 100 ml min⁻¹, F_{Air} = 96 ml min⁻¹, amount of sample = 0.5035 g, P = 1 bar. XI
- C.3. Reaction curve of catalyst 6.5NiCoO/CeO₂/L-S5. Reaction conditions: F_{CH₄} = 4 ml min⁻¹, F_{N₂} = 100 ml min⁻¹, F_{Air} = 96 ml min⁻¹, amount of sample = 0.5012 g, P = 1 bar. XI
- C.4. Methane conversion curve of sample 6.6NiCoO/CeO₂/L-S6. Reaction conditions: F_{CH₄} = 4 ml min⁻¹, F_{N₂} = 100 ml min⁻¹, F_{Air} = 96 ml min⁻¹, amount of sample = 0.5009 g, P = 1 bar. XII
- C.5. Long-term reaction 6.5NiCoO/CeO₂/L-S5. Reaction conditions: F_{CH₄} = 4 ml min⁻¹, F_{N₂} = 80 ml min⁻¹, F_{Air} = 96 ml min⁻¹, F_{H₂O} = 20 ml min⁻¹, amount of sample = 0.5051 g, proportion of active material = 0.033 g, P = 1 bar, T = 450 °C. XIII
- C.6. Long-term reaction 6.6NiCoO/CeO₂/L-S6. Reaction conditions: F_{CH₄} = 4 ml min⁻¹, F_{N₂} = 80 ml min⁻¹, F_{Air} = 96 ml min⁻¹, F_{H₂O} = 20 ml min⁻¹, amount of sample = 0.5036 g, proportion of active material = 0.033 g, P = 1 bar, T = 450 °C. XIII
- C.7. Long-term reaction 6.5NiCoO/CeO₂/H-S7. Reaction conditions: F_{CH₄} = 4 ml min⁻¹, F_{N₂} = 80 ml min⁻¹, F_{Air} = 96 ml min⁻¹, F_{H₂O} = 20 ml min⁻¹, amount of sample = 0.5060 g, proportion of active material = 0.033 g, P = 1 bar, T = 450 °C. XIV
- C.8. Carbon error sample 6.0NiCoO/CeO₂/L-S3. XIV
- C.9. Carbon error sample 5.7NiCoO/CeO₂/L-S4. XIV
- C.10. Carbon error sample 6.6NiCoO/CeO₂/L-S6. XV
- C.11. Methane conversion curve of low surface area CeO₂. Reaction conditions: F_{CH₄} = 4 ml min⁻¹, F_{N₂} = 100 ml min⁻¹, F_{Air} = 96 ml min⁻¹, amount of sample = 0.5 g, P = 1 bar. XVI

D.1. LFC calibration curve XVII

List of Tables

2.1.	Different types of carrier gas and their preferred detectors	20
3.1.	wt % active material, amount of support, nickel and cobalt used for the synthesis of catalysts.	28
3.2.	Molar mixing ratio and amount of $\text{Ce}(\text{NO}_3)_3$, NaOH and H_2O used during synthesis of high surface area CeO_2	28
3.3.	Amount of sample material and boric acid used for analysis of sample composition.	29
3.4.	Analysis parameters used during identification of NiCo_2O_4 and carbon in samples using Raman.	29
3.5.	Analysis parameter used for analysis of samples using XRD.	30
3.6.	Weight of test tubes and total weight of test tubes and samples before and after degassing.	30
3.7.	Standard analysis parameters and sample amount used to analyse the reducing properties of synthesized samples and support.	31
3.8.	Standard flow parameters for rig 2.9	34
3.9.	Flow parameters for H_2O activity tests	34
4.1.	XRF composition and deviation (d) from nominal NiCo oxide content in catalysts supported on high and low surface area CeO_2	37
4.2.	N_2 - physisorption measurement results of CeO_2/H and CeO_2/L with and without NiCo_2O_4	38
4.3.	Calculated crystallite size for peaks found in the 2θ range 15-75 °for the support material CeO_2/H and CeO_2/L	40
4.4.	Calculated CeO_2 crystallite size for the peaks found between $2\theta = 15-75$ °for NiCo_2O_4 catalysts synthesized on high-and low surface area CeO_2	42
4.5.	Reaction rate calculated at $T = 400$ and 450 °C, for catalysts supported on high-and low surface area CeO_2 and NiCo_2O_4	46
4.6.	Reaction rate calculated for repeating wet and dry reaction cycles at 450 °C for catalyst 6.6NiCoO/ CeO_2/L -S6.	48
4.7.	Comparison of activity of 6.6NiCoO/ CeO_2/L -S6 and NiCo_2O_4 SINTEF connected with time on stream (TOS).	49
4.8.	Comparison of bulk activity pr. m^2 of 6.6NiCoO/ CeO_2/L -S6 and 6.5NiCoO/ CeO_2/H -S7.	50
A.1.	Mass Ni, Co, and CeO_2 used for the synthesis of catalysts	II
A.2.	XRF analysis result of catalysts supported by high- and low surface area CeO_2	III
B.1.	BJH: raw data from pore size investigation of CeO_2/H	V

-
- C.1. Reaction result from CeO_2/L test in rig 2.9. Reaction conditions: $F_{\text{CH}_4} = 4 \text{ ml min}^{-1}$,
 $F_{\text{N}_2} = 100 \text{ ml min}^{-1}$, $F_{\text{Air}} = 96 \text{ ml min}^{-1}$, amount of sample = 0.5000 g, $p = 1 \text{ bar}$. . . XVI
- D.1. Calibration measurements obtained for LFC XVII

1. Introduction

1.1. Motivation

After generations of utilizing fossil energy sources such as coal and oil, the global temperature has increased by approx. $0.07\text{ }^{\circ}\text{C}$ per decade since 1880 [1]. The Paris Agreement signed by 189 nations in 2016 commits the nations to limiting global warming to below $2\text{ }^{\circ}\text{C}$ [2]. If this goal is to be achieved, alternative energy sources that either pollute less or are green must be used to replace coal and oil. Other solutions will also be advantageous in terms of energy optimization as well as utilization and purification of the fuel currently available for various industries.

Shipping, alone, stands for more than 2.2 % of the global CO_2 emission, and has the potential to grow with 50 % until 2050 [3]. Like many other countries, Norway is a maritime nation with a long coastline and a proud history of seafaring. As part of the Paris Agreement, the country commits itself to reducing the environmental impact from shipping as a part of the global solution. In 2018, Norway's domestic shipping and fishing accounted for 3.2 Million tonnes of CO_2 equivalents that is equivalent to 6 % of the total Norwegian greenhouse gas emissions [4][5]. The Norwegian government has also stated that if the maritime sector is to achieve a 40 % emission reduction by 2040, approximately 1 % of the fleet must change into an alternative fuel source yearly so that 28 % of the fleet is driven either by electricity, bio-fuel or natural gas (NG) in 2040 [6].

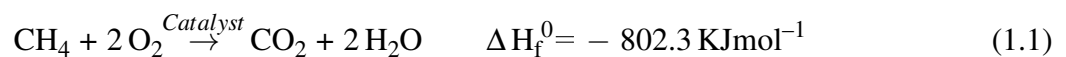
Today, Heavy Fuel Oil (HFO) -or different types of HFO-based blends are the most widely used types of fuel in the marine industry and part of the reason for this lies in costs and resource availability. However, HFO-based fuel originates from residual fuel oils which is complex in composition and contains a large number of impurities which entails it to be highly pollutant [7].

Methane is assumed to be one of the alternative energy sources of the future, yet the global warming potential (GWP) exhibits an environmental risk [8]. Compared to CO_2 , CH_4 have a GWP that is 21-28 times stronger over a periode of 100-years, and even stronger in a shorter time perspective [9]. In contrast to HFO, NG contains significantly less impurities, and 85-95 % of the gas is CH_4 . Further processing of NG into Liquefied Natural Gas (LNG) removes pollutants and makes it the cleanest of the fossil fuels [10]. Another source of CH_4 is biogas (BG) produced from fermentation of organic industrial waste such as agricultural residue or fish. The gas is considered to be carbon neutral with potential to reduce global CO_2 emissions. But the BG mixture mainly consists of CH_4 and CO_2 , and consequently further processing into liquified biogas (LBG) is necessary before the gas can be utilized as fuel.

Regardless of the fuels origin, the downside with LNG, LBG and compressed natural gas (CNG) lays in the methane slip and the environmental consequences which are associated with GWP. In principle, the methane slip is a result of engine design, vessel weight and engine performance related to different operating conditions.

Historically, formation of NO_x has been suppressed compared to excess emission of CH₄, using engine designing alone. In fact, it is impossible to maintain high efficiency as well as reduce emissions of CH₄ and NO_x at the same time through engine designing. Consequently, the gas that is not handled by engine design must be post-treated [11]. Handling the methane slip can include different engine designs or fuel injection systems, but a possible solution could also be catalytic combustion of the exhaust gas as illustrated in reaction 1.1. Since the exhaust gas consists mainly of CO₂, H₂O, CO, CH₄ at a relatively low temperature it will be necessary to develop a catalyst which can operate under the following conditions:

- High catalytic activity at low temperatures (< 550 °C)
- High efficiency at low concentration of CH₄ (< 1000 ppm)
- Tolerance to SO_x poisoning
- Tolerance to steam (10-15 %), CO₂ (15 %) and O₂



1.2. Objective

The objective of this master thesis is reproducing the activity results obtained during the specialisation project by impregnating the NiCo₂O₄ catalyst on commercial low surface area CeO₂. Further, synthesis of high surface area CeO₂ will be performed for the purpose of establishing a support with different morphological structure. Moreover, NiCo oxides supported on high surface area CeO₂ will be compared to low surface area catalysts to investigate if there are any benefits by changing the support structure in terms of activity and stability. Additionally, the synthesized catalysts will be characterised using some of the best-known characterisations techniques to obtain information of the catalysts properties. Furthermore, the catalysts will be exposed for wet reaction conditions to further investigate the activity under realistic conditions, and to obtain information about deactivation mechanism and utilization of the support material.

1.3. Method

This master's thesis was written in connection with the research project EmX2025, which deals with reduction of greenhouse gas emissions from the Norwegian marine transport industry. In addition, this thesis is an extension of the specialization project that was completed in the fall of 2019 [12]. Some of the results achieved will be reused, but this will be noted when applied. The research project has previously produced three master's theses that focused on noble metal catalysts, but also NiCo_2O_4 spinel [13] [14] [15]. In the spring and summer of 2019, an internship was made by Schuster in connection with the project involving the synthesis of NiCo_2O_4 spinel on $\gamma\text{-Al}_2\text{O}_3$ and CeO_2 support [16]. The work done in connection to this formed the basis for the project and the master's thesis as the results for synthesized NiCo_2O_4 on CeO_2 were positive in terms of activity and stability.

The methods derived from the project were carried out independently but under the guidance of supervisors. The practical work of implementing different characterization techniques as well as activity tests was carried out independently. Training was provided initially by supervisors and department engineers. When needed for help and troubleshooting, the same engineers were used.

The literature search on which a large part of the thesis is based was carried out by reading relevant articles and research papers. These articles were retrieved through several different databases, and the references were carefully reviewed. The theory acquired was used to explain and understand the results obtained in the experiments.

2. Theory

2.1. Natural Gas as Fuel

As previously mentioned, natural gas consists mainly of methane, CH_4 , and is one of the most abundant energy sources on the planet. However, over one-third of the natural gas reserves are not developed and this is mainly due to the remote location of the reservoirs [17]. The development of liquefied natural gas processing plants (LNG-Plant) creates access to an abundant source of less polluting fuel. Ships driven by LNG has the potential to reduce emissions of CO_2 and other harmful compounds, and this can both improve air quality and lower the global warming impact from the marine industry.

In principle, the methane slip is a result of high air excess ratio due to suppression of NO_x formation in the combustion chamber. Thermal NO_x is favoured at high temperatures (1300 °C) and due to historically-and-environmental causes, the International Maritime Organization (IMO) has set strict regulations according to NO_x emissions through the Tier (III) standard [18]. In addition, the methane slip is also affected by engine design- and performance, which are related to vessel weight.

At the moment there are two types of engines that are promising according to application of NG/LNG, Lean burn spark ignited (LBSI) and low pressure dual fuel (LPDF) engines. The LBSI typically operate with an excess air ratio of $\lambda = 2$ that results in less NO_x emission due to a lower peak combustion temperature. The downside to this technology is bulk quenching in the coldest areas of the combustion chamber that increases the methane slip. In contrast, the LPDF engine is a type of engine that can utilize two types of fuel LNG and conventional diesel. The operational principle is similar to LBSI, but LPDF has the benefit of choosing between several types of fuel depending on availability. This advantage is an important factor when it comes to undeveloped LNG infrastructure as stated previously. But the drawback is the same for both engines, especially when it comes to bulk quenching and methane slip at a low vessel load [11].

Considering the GWP of CH_4 and the lack of regulation according to methane-slip from ship engines, the benefits of LNG can not be exploited before a solution to these problems can be found. Together with more regulation and the development of combustion technology, catalytic combustion of the exhaust gas can be a solution to the problem.

2.2. Catalytic Combustion of Methane

Catalytic combustion of methane has previously been investigated as an alternative to conventional thermal combustion of natural gas in gas turbine combustors, and has showed positive results according to energy production and reducing emissions. Another application of catalytic combustion is the abatement of methane emissions from lean-burning NG engines found in LNG driven ships [19]. Further in this section, noble metal-and metal-oxide catalysts used in catalytic oxidation of methane will be presented.

2.2.1. Nobel Metal Catalyst

Among noble metal catalyst used for catalytic combustion of methane, Palladium (Pd) and Platinum (Pt) are two of the most studied species. Experiments with lean-burn conditions have revealed superior activity towards methane conversion for Pd [19]. And further investigation of Pd has led to increased activity by utilizing metal-oxides, like Al_2O_3 or CeO_2 , as support material. J. Chen et al. was able to achieve complete conversion at 300 °C for CeO_2 based catalysts and 410 °C for Al_2O_3 at GHSV of 50000 ^{-1} [20]. Nevertheless, some key factors such as material cost and resource availability has a major role when it comes to catalyst development. Additional studies have demonstrated a serious drawback in cases of deactivation caused by sulphur poisoning and water sensitivity that could turn Pd based catalysts unqualified [19]. However, experimental alloys consisting of Pt and Pd, have been shown to improve stability according to the deactivation mechanisms compared to mono-metal catalysts. [20].

2.2.2. Metal Oxide Catalyst

In catalytic oxidation, metal oxides and especially metal transition elements have an important role due to multiple valence states and the capability to create redox cycles between a high oxidation state and a low oxidation state, but also at the same time, release and restore lattice oxygen. Unlike noble metal-based catalysts, the relevant metal oxides are made up from abundant raw materials that are far less expensive, and catalysts with appropriate activity and thermal stability can be made with proper ingredients and synthesis techniques [20].

The NiCo_2O_4 spinel is such a compound that consists of earth-abundant elements and can completely oxidize methane in the temperature range of 350-550 °C [21]. Stoichiometric ratio studies of nickel and cobalt based catalysts performed by Ragnhild B. Lund-Johansen has revealed limited influence on catalytic activity [15]. In addition, the same experiments have demonstrated that low CH_4 concentration causes higher activity at lower temperatures. However, similar deactivation mechanism as found in noble metal-based catalysts regarding water in the feed stream reduces the positive impact [15].

The reaction mechanism of CH_4 on NiCo_2O_4 have been investigated by Franklin Feng, T. et al. [21]. The initial step of the reaction is dissociation of CH_4 into CH_3 . Further it is suggested that formation of CH_2 from CH_3 occurs through two different routes. Where the first includes dehydrogenation of

CH_3 into CH_2 the second involves coupling of the carbon atom of CH_3 with surface lattice oxygen to form CH_3O binding to an Ni cation. It is proposed that the reaction follows the second reaction path due to CHO playing an important role in oxidation of methane on different catalysts surfaces.

Formation of CHO is suggested to occur through two different reaction branches as shown in figure 2.1 The main difference between the reaction routes lies in the oxygen contribution of Co. Dehydrogenation of CH_3 by OH on the nickel surface (A) is neglected since the reaction through Co is more favourable (B). Further transformation of the intermediate CHO into product molecules is proposed to go through two sub-pathways including OCHO dehydrogenation and CO oxidation.

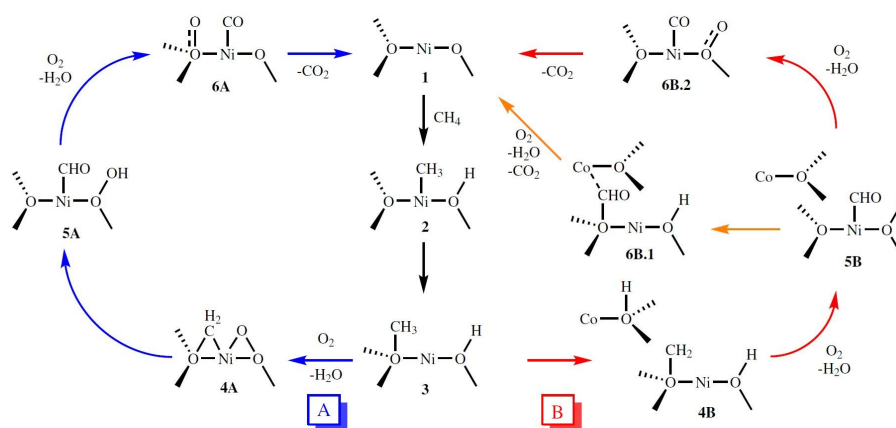


Figure 2.1.: Illustration of possible reaction pathway for methane on NiCo_2O_4 based catalyst [16].

Henrik Schuster developed the nickel-cobalt based catalyst by synthesizing it on $\gamma\text{-Al}_2\text{O}_3$ [16]. Activity tests revealed severe deactivation in terms of sintering that made the catalysts unsuitable for exhaust gas treatment. However, promising results were obtained by additional improvement of the support material by utilizing high surface area CeO_2 . Ceria has high oxygen storage capacity and the ability to disperse active components so that sintering can be avoided at high temperature. $\text{CoO}_x/\text{CeO}_2$ catalysts have been considerably used in many different reactions, for example diesel oxidation, N_2O decomposition, methanol oxidation and CO oxidation [22]. It has been claimed that there exists a catalytic synergistic effect between cobalt and cerium oxides that lead to a greater activity compared to each single oxide [22]. Today, ceria has emerged as a new promising catalyst component that has a wide range of catalytic applications, wanted redox properties and reactivity. CeO_2 is the most abundant rare earth material and about 0.0046 wt % of the Earth's crust consists of this element [23]. However, these qualities are highly dependent on the preparation technique because it influences the structural features such as surface area, component dispersion and interaction strength of the catalyst [22].

2.2.3. Catalyst Morphology

As previously mentioned, the nickel-cobalt spinel catalyst on commercial low surface area ceria, CeO_2/L , was investigated during autumn 2019. Two catalysts with different active material load (6.3 wt % and 16.3 wt %) was synthesized, 6.3NiCoO/ $\text{CeO}_2/\text{L-S1}$ and 16.3NiCoO/ $\text{CeO}_2/\text{L-S2}$, and compared to the results obtained by H. Schuster. The activity tests results achieved indicated that 6.3NiCoO/ $\text{CeO}_2/\text{L-S1}$ utilized the metal load much better than the higher loaded samples. Characterization studies of the catalysts revealed large crystalline phases and no defined pore structure for the support. Based on the results, it could indicate that the catalysts had smooth surface that could be illustrated as a small ball coated with NiCo_2O_4 clusters as shown in figure 2.2.

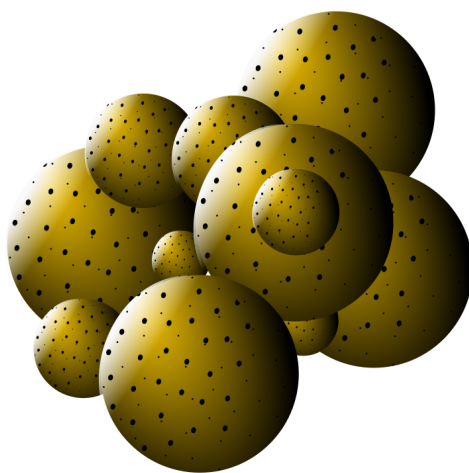


Figure 2.2.: Envisioned catalyst with marble structure consisting of low surface area Ceria with no defined pore structure and dispersed NiCo_2O_4 spinel as black dots. The figure is created in Inkscape.

Porous materials, such as carbon, has systems with irregular shape and structure. For some materials the pore system is caused by space between crystallites, and the channels are named after the width, for instance micropores (≤ 2 nm), mesopores (2-50 nm) and macropores (≥ 50 nm) [24]. Understanding the importance of well-defined pore structure in catalysts development relates to enhanced accessibility of active sites and increased activity.

The catalysts crystallites consist of a crystal lattice constructed from crystals with different structures such as face-centred cubic (fcc), hexagonally close-packed (hcp) or body-centered cubic (bcc) [25]. However, the most typical structure of CeO_2 is cubic fluorite [26]. The structure can be defined as a cubic eutaxa of M atoms with O atoms in tetrahedral intercedes as shown in figure 2.3.

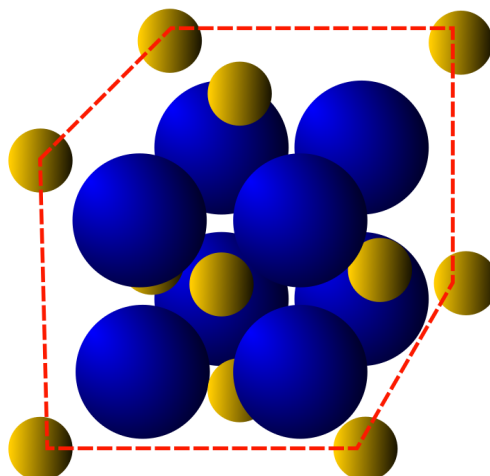


Figure 2.3.: Illustration of CeO_2 structure created in Inkscape. Oxygen atoms in tetrahedral structure as well as interaction with Ce atoms in cubic eutaxa.

CeO_2 with ceria in oxidation state +IV, is the most stable oxide of ceria when it comes to ambient pressure and temperature. The ability to quickly switch between +III and +IV oxidation state is one of the properties contributing to the catalytic benefits, and ceria is known for its elevated oxygen transfer capacity [27]. The methane oxidation reaction on the nickel-cobalt spinel catalyst supported by ceria is illustrated in figure 2.4. The structure show how a great extent of oxygen is stored in the lattice system as a result of the cubic fluorite structure.

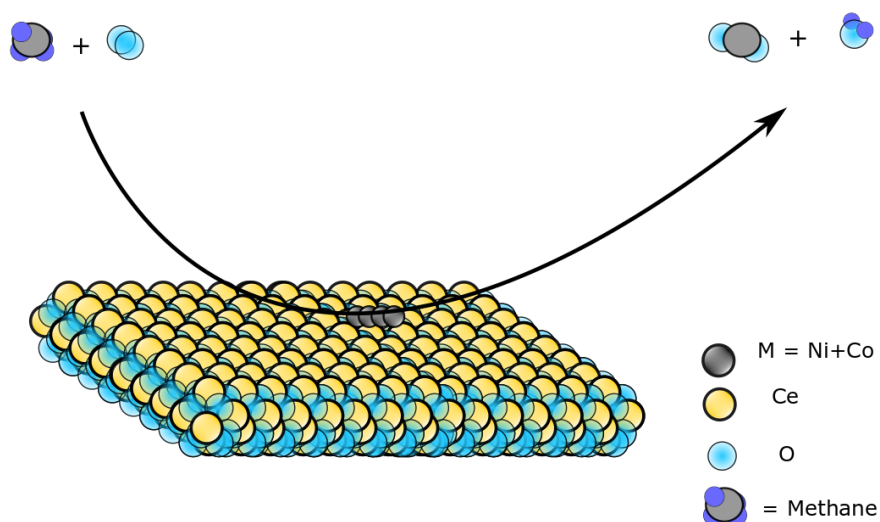


Figure 2.4.: Catalytic oxidation of methane illustrated on a surface consisting of CeO_2 . The Lattice oxygen network shows the oxygen storage capacity of the support. The figure is created in Inkscape.

2.3. Catalyst Synthesis

Production of catalysts can be performed with several different synthesis techniques such as coprecipitation, wetness impregnation (WI) and incipient wetness impregnation (IWI). The common feature between these methods are precipitation due to saturation. Accordingly, the catalysts structure is a result of precipitation technique and execution. However, further in this section only synthesis through IWI and sol-gel will be presented.

2.3.1. Incipient Wetness Impregnation

Incipient Wetness Impregnation is a popular method used for heterogeneous catalyst preparation. The technique is known for its simplicity when it comes to execution, limited waste production and low costs due to low consumption of expensive materials and solvents. However, the method is far from the most widely used for catalyst preparation [28].

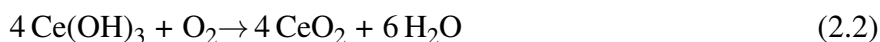
The principle is based on pore volume measurements of the support material and the solubility of salts containing active materials. A precursors solution is made by dissolving for example nitrates in distilled-or-deionized water. The limiting factor, previously mentioned, is the pore volume and the salts solubility. Consequently, the concentration and volume of the solution is either based on one or both limiting factors, hence, the method is mostly used for low loading. The pore volume indicates how much solution is needed to fill the pores of the support, and as a result the impregnation can be performed either in one-or-multiple rounds with drying in between. Hence, the consistence of the material during impregnation gives rise to another name to the method, dry impregnation [28].

2.3.2. Sol-gel Based Synthesis of High Surface Area Mesoporous Ceria

The principle of high surface area mesoporous CeO_2 synthesis is based on Sol-gel chemistry at room temperature and atmospheric pressure. The gel consists of a high alkaline solution that is formed by dissolving sodium hydroxide in distilled water. When $\text{Ce}(\text{NO}_3)_3$ is added to the gel, reaction 2.1 is initiated, and the colloidal solution (Sol) is established. The solution consist of two different phases where small $\text{Ce}(\text{OH})_3$ particles are finely dispersed through the medium [29]. CeO_2 is formed when $\text{Ce}(\text{OH})_3$ reacts with oxygen according to reaction 2.2. The oxygen is provided through the atmosphere and constant stirring [30].

In contrast to other precipitation methods where pH is regulated, this method is settled through the molar ratio between $\text{NaOH}/\text{H}_2\text{O}$ and $\text{Ce}(\text{NO}_3)_3/\text{NaOH}$. The reaction progress is monitored through colour changes that occurs in the solution. Following the synthesis procedure, the product is washed to remove Na^+ and to neutralize the pH. The solid product is then dried to remove water and make it suitable for further processing with IWI.

Given that the method uses cerium (III) nitrate as ceria source and no expensive organic or inorganic templates, the synthesis benefits from low costs. Simultaneous, the reaction occurs at room temperature, hence a low energy consumption.



2.3.3. Drying and Calcination

As a result of the synthesis process, the catalyst precursor contains IWI solution with dissolved active materials. Drying is a process where the solvent is evaporated beyond the point of saturation, and precipitation of the active material forms crystals on the surface of the catalysts, preferably where the active material interact with the support [28].

The drying rate is controlled by the temperature and it should be close to the boiling point of the solvent or at a lower temperature for a more careful drying. Egg shell distribution and egg yolk formation are examples of phenomenon that occurs when the rate is too fast or too slow. At shell distribution, active material encapsulates the catalysts pores. On the other hand, yolk formation causes large particles in the pore core.

Calcination is a stabilizing procedure where the catalysts structure, pores and impurities are shaped and removed. Nevertheless, the most important point is to form oxides from the nitrates and to establish the chemistry for further use.

2.4. Catalytic Characterization

In this section, different characterization techniques used to determine catalytic properties such as morphology, reducibility, active sites and composition are presented.

2.4.1. X-ray Fluorescence

X-ray Fluorescence (XRF) is a method that utilizes the characteristic emission wavelengths that are independent of the chemical association of the elements to identify the presence of different elements in a sample. Furthermore, the technique can be used in quantitative analysis, and it has multi-element capacity.

A wide range of different characterization techniques, such as X-ray Diffraction and SEM, is built around the same concept as XRF. The method is established on photoelectric principles that utilize energy provided from photons to cause emission of fluorescence in a sample [31]. The foundation is illustrated in figure 2.5, where fluorescence is created through a three-step pathway. In the beginning high energy photons, originating from an X-ray source, collide with atomic electrons in the inner orbital causing them to eject from their position due to energy absorption. Consequently, an unstable atom with electron vacancy is formed which initiates a counter response either through ejection of atomic electrons or emission of fluorescence due to electron migration. Ejection of atomic electrons is a physical phenomenon known as the Auger effect, and it occurs when electrons with higher energy fill the vacancy. Excess energy, provided by high energy electrons, is adsorbed by another atomic electron, causing it to eject from the atom. On the other hand, when the vacancy is filled with electrons from outer orbitals fluorescence is emitted due to energy difference. The fluorescence yield depends on which of the pathways that is most prominent since they are competing. The effectiveness or the likelihood of fluorescence emission occurring is measured as ω , and the sensitivity of the method is poor for elements with low atomic number [31, 32].

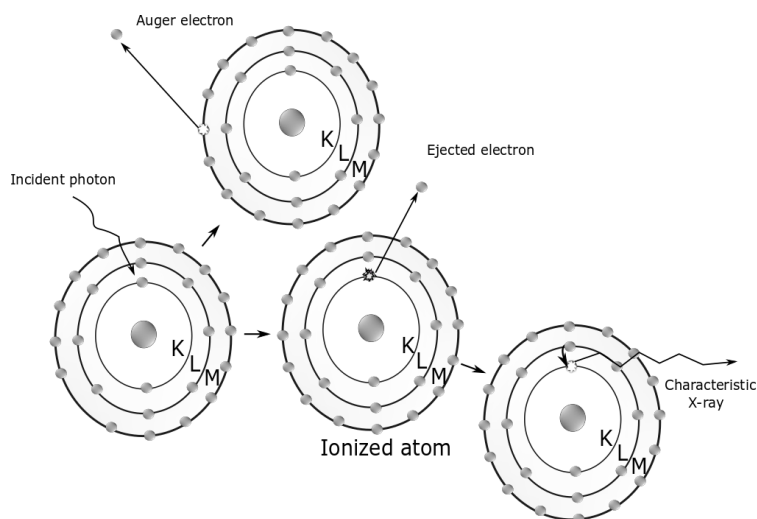


Figure 2.5.: Illustration of X-ray emissions pathways created in Inkscape. Starting out with an incoming X-ray beam that leads to ejection of inner electron. The atom stability is obtained either by Auger electron or fluorescence emission [31].

2.4.2. X-ray Diffraction

X-ray Diffraction (XRD) is a method applied for examine crystalline phases found in catalysts and to obtain information about crystal size. As mentioned in the XRF section, the process utilizes diffraction caused by elastic scattering of photons. When photons are scattered in a periodic lattice constructive interference is obtained. The lattice spacing is derived from the Bragg relation 2.3.

$$n\lambda = 2d\sin\theta \quad n=1,2,\dots \quad (2.3)$$

where:

- n is the order of reflection
- λ is the wavelength of the X-rays
- d is the distance between the two lattice planes
- θ is the angle between the incoming beams and the reflection

The lattice scattering is illustrated in figure 2.6 where the left side of the figure explains Bragg's law through a set of atoms in an array. Constructive interference occurs only when the angle of the incoming X-ray is equal to the scattered beam so that equation 2.3 are satisfied. Because $\sin\theta$ never can be larger than 1, then $n\lambda$ must be smaller than $2d$, and λ must be smaller than $\frac{2d}{n}$ [33]. If the angle 2θ is measured when constructively interfering X-rays is reflected from the crystal, then the Bragg relationship will give the corresponding lattice spacing that is characteristic for a specific compound.

If the principle is expanded into a three-dimensional array and the system consists of many different parallel planes instead of atoms the planes will also be able to form constructive interference when equation 2.3 is satisfied. Unlike the two-dimensional system where d is the distance between the

atoms, d is now the distance between the planes. Therefore, there will be many values for d because the system consists of many different planes, and many sets of angles that provides constructive interference for the crystal. The phenomena is called Bragg reflection [33].

The right side of figure 2.6 shows a powder sample consisting of many crystalline particles where the lines illustrate the direction. As show, not all the particles have the same direction, meaning not all of them will contribute to form constructive interference during analysis. To increase the number of particles contributing to diffraction during examination the sample is rotated [25].

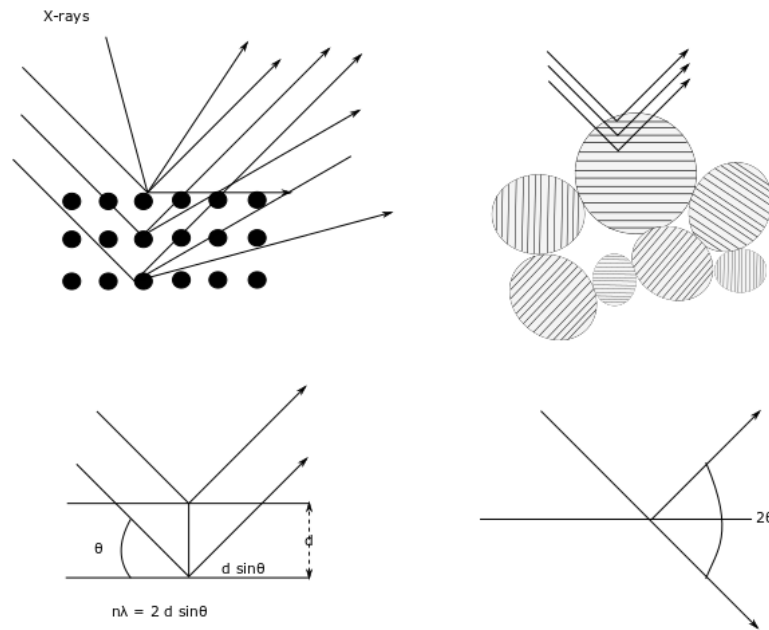


Figure 2.6.: Lattice scattering of X-rays, information of the crystalline phase is obtained through Bragg's relationship [34].

The crystal size is given by the Scherrer equation 2.4 that relates the crystal size to the line width.

$$\langle L \rangle = \frac{k\lambda}{\beta \cos\theta} \quad (2.4)$$

Where:

- L is the crystallite size
- K is a constant, often 1
- θ is the angle between the incoming X-ray beam and the normal on the reflecting plane
- β is the peak width
- λ is the wavelength of the X-ray beam

The method has its limitation, especially when it comes to particle size. If the particles are too small or amorphous the method is not capable to detect them. This can cause uncertainty about what kind of phases that are present in the sample [25][34].

2.4.3. N₂-Physisorption

N₂-Physisorption is a method used to determine the surface area and pore size distribution of porous materials with surface area greater than 1 or 2 m²/g. The principle is based on adsorption of N₂ at liquid N₂ temperature (77 K). N₂ molecules adsorbed to the surface occupies an area comparable to the cross-section area of one single molecule (0.162 m²). The internal surface area can be determined by measuring the number of N₂ molecules adsorbed at monolayer coverage[25, 35].

Figure 2.7 shows an illustration of the IV Brunauer-Emmett-Teller (BET) isotherm, and it can be used to demonstrate the principle behind the process. In the beginning, adsorption of gas at low pressure occurs. When the pressure starts to increase, a monolayer is formed on the surface as a result of more molecules being adsorbed. The next stage is formation of multilayers, and finally condensation inside the pores.

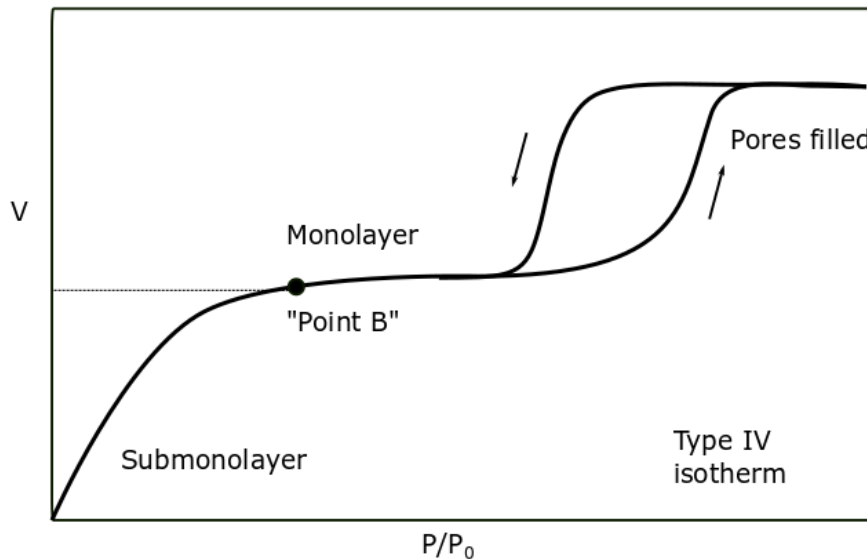


Figure 2.7.: Illustration of type IV BET-isotherm created in Inkscape [25].

The BET equation 2.5 gives the relationship between N₂ volume adsorbed at a given partial pressure and the volume adsorbed at monolayer coverage.

$$\frac{P}{V_{\alpha}(P_0 - P)} = \frac{1}{xV_0} + \frac{x-1}{xV_0} \frac{P}{P_0} = n + \alpha \frac{P}{P_0} \quad (2.5)$$

Where:

- V_{α} is the total volume
- V_0 is the volume of adsorbed molecules in the first layer
- P_0 is the partial pressure of condensed gas
- P is the pressure
- x is the desorption rate of the first and the second layer

The BET-isotherm is only valid under the following assumptions [25]:

- The adsorbate and adsorptive are in dynamic equilibrium, and in any layer, the rate of adsorption and desorption are equal.
- The adsorption site for any molecule are equivalent in the first layer.
- The adsorption site for the second layer and for higher layers are constituted by the first layer.
- Adsorbate-adsorbate interactions are neglected.
- Adsorption-desorption conditions are the same for any layer, except for the first layer.
- The condensation energy is equal to the adsorption energy for the 2nd layer and for any layer above that.
- At saturation pressure ($P=P_0$), the multilayer grows to infinite thickness.

When condensation is reached, another equation is applied to determine pore size distribution through the Barrett-Joyner-Halenda method (BJH). BJH is based on the Kelvin equation 2.6 that describes the desorption isotherm [25].

$$\ln \frac{P}{P_0} = - \frac{2\sigma V \cos\theta}{rRT} \quad (2.6)$$

where:

- σ is the surface tension of liquid N_2
- θ is the contact angle
- V is the molar volume of liquid N_2
- r is the pore radius
- R is the gas constant
- T is the absolute temperature
- P is measured pressure
- P_0 is the saturation pressure

The adsorption-desorption hysteresis is classified by IUPAC. This is typical desorption branches used for calculation and describing the structure of the catalyst, figure 2.8 shows an illustration. For example, H1 hysteresis is obtained for catalyst with narrow distribution of mesopores. The type H2 is a branch that is typical for active carbon. H3 and H4 is related to catalysts that has no well-defined mesopore structure, and H3 is typical for clays [24].

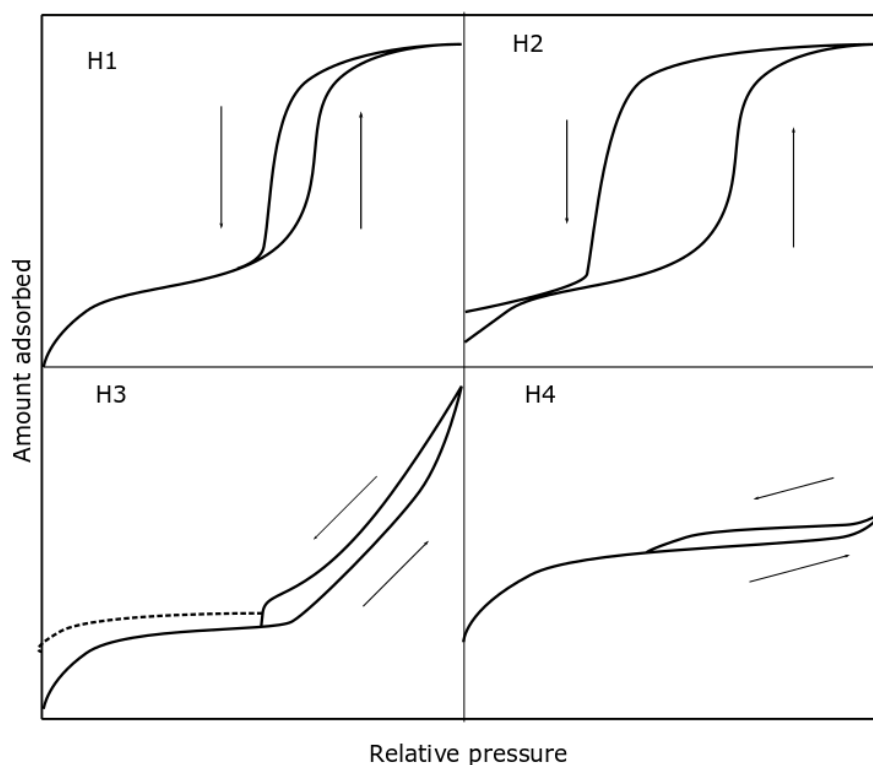


Figure 2.8.: Illustration of adsorption-desorption hysteresis H1,H2,H3 and H4 classified according to IUPAC, created in Inkscape [24].

2.4.4. Raman Spectroscopy

Raman spectroscopy is a characterization technique used to investigate catalytic surface down to a depth comparable to the wavelength of light. The principle is based on inelastic scattering of photons caused by energy loss due to exciting vibration. A schematic illustration of the scattering procedure is illustrated in figure 2.9. During examination, the sample is exposed to monochromatic light with the frequency V_o . Most of the light that falls onto the sample undergoes Rayleigh scattering, meaning it scatters light without energy exchange. On the other side, formation of Stokes band is a result of energy loss in the photon equal to hV_{vib} , consequently the intensity of the scattered light has the frequency of $V_o - V_{vib}$. The opposite process is formation of anti-Stokes band. This phenomenon occurs when the energy equal to V_{vib} is transferred to the photon, resulting in a higher frequency of $V_o + V_{vib}$ in the sample [34].

In contrast to infrared spectroscopy where the molecules adsorb photons with the same frequency as its vibrations, the molecules in Raman spectroscopy lose energy. Nevertheless, not all vibrations are observed in Raman spectroscopy as well as in infrared spectroscopy. According to the selection rule of infrared spectroscopy during vibration, the dipole moment must change. Consequently, molecules such as H_2 (4160.2 cm^{-1}), N_2 (2330.7 cm^{-1}) and O_2 (1554.7 cm^{-1}) can not be observed with infrared spectroscopy. Therefore, for symmetric particles the two techniques complement each other [34].

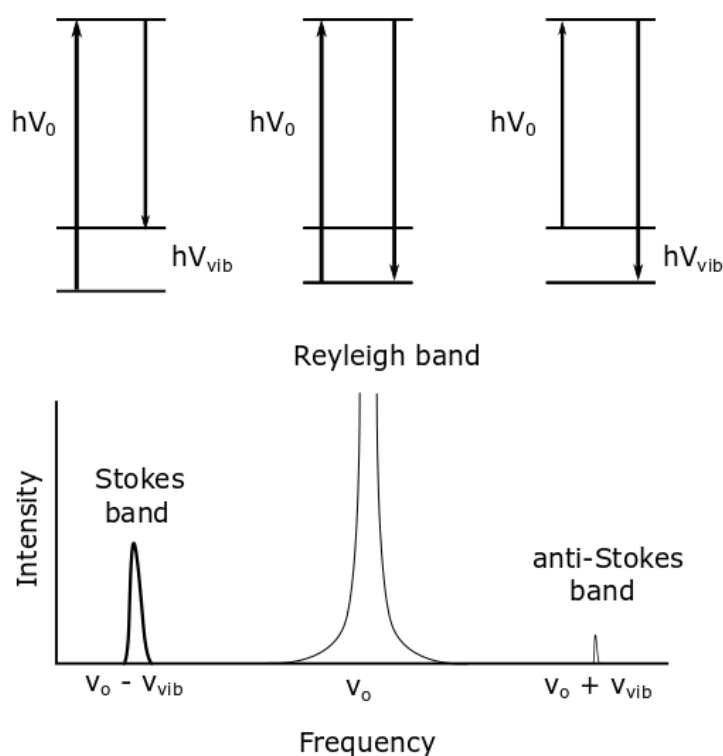


Figure 2.9.: Illustration of Raman scattering with frequency V_0 (Reyleigh band), $V_0 - V_{vib}$ (Stokes band) and $V_0 + V_{vib}$ (anti-Stokes band). Illustration created in Inkscape [34].

One benefit to this method is that typical support materials like alumina and silica are weak Raman scatters that allow measurement of adsorbed species at lower wavenumber (50 cm^{-1}). Thus, the method can be a powerful tool to study active phases on supported catalysts. Additional value of the Raman spectroscopy is its ability to be used in in-situ studies due to weak interference between signals between the adsorbed species and the gas phase. Nevertheless, the disadvantages of this method are the small cross-section for Raman scattering. Most of the scattered intensity is in the form of Rayleigh band that is typical three times higher than intensity of stokes band. The problem can be handled with a stronger laser, but desorption and decomposition of surface components can occur due to heat. Disruptions of weak signals caused by fluorescence is another disadvantage that may occur, resulting in lower detectability.

2.4.5. Gas Chromatography

Gas Chromatography (GS) is an analytical technique that is based on separation of chemical compounds between two different phases. Moreover, the method can be applied for composition determination in gas mixtures or assess the quality of sample compounds [36]. A simplified illustration of an GC apparatus with the basic components carrier gas, injector, splitter, column and detector is shown in figure 2.10.

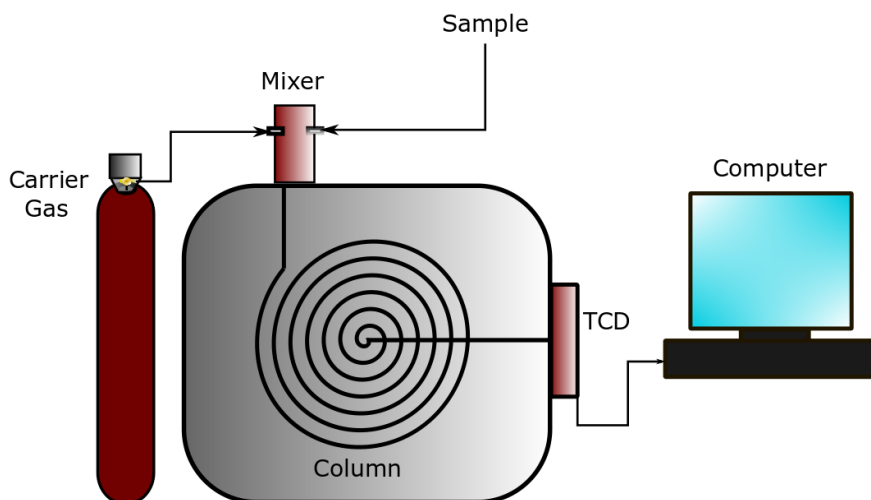


Figure 2.10.: Simple illustration of Gas Chromatography created with Inkscape

As previously mentioned, the principle is based on separation between two phases known as the mobile and the stationary phase. The mobile phase is a mixture between the sample and an inert carrier gas, with the purpose to transport the sample through the column. The second objective of the carrier gas is to provide an appropriate matrix for the detector so it can measure the sample fractions, hence the choice of carrier gas depends on the detector. Additionally, the detectors are classified according to measurement units, selectivity and if they are destructive or non-destructive. Some of the most common detectors are:

- Thermal Conductivity (TCD)
- Flame Ionization (FID)
- Electron Capture (ECD)

When concentration is the desired unit of measurement, it is typical to use either TCD or ECD. For selective measurements ECD or FID is applied. Some carrier gases and their preferred detectors can be seen in table 2.1. Moreover, hydrogen can also be applied as a carrier, but H_2 sets stricter requirements to HSE due to fire and explosion hazard [37].

Table 2.1.: Different types of carrier gas and their preferred detectors

Detector	Carrier gas
TCD	Helium or Argon
FID	Helium or Nitrogen
ECD	Very dry Nitrogen

Furthermore, the injector consists of two essential parts, the mixing zone and splitter. Where the primary function of the mixer is to mix sample and carrier gas before injection, the splitter controls sample load on the column.

In similar fashion to the mobile phase, the stationary phase may be structured differently depending on the purpose. 90 % of the columns used today are wall-coated open tubular columns (WCOT). WCOT is recognised by the length and the inner coating that consists of a thin liquid stationary phase. In contrast, packed columns consist of a shorter column where the stationary phase is coated on a solid support. Additionally, the most common material used for the stationary phase is fused silica, glass or stainless steel.

The separation principle of GC is based on polarity of the examined species and the column. In general, there exists three types of columns which has several subcategories. The main categories are:

- Polar
- Non-Polar
- Intermediate Polarity

In general, polar columns are mostly used for separation of polar analytes such as alcohols and amines. The elution order is determined by the interaction between the analyte and the stationary phase. This means that polar substances stay for a longer period inside the column compared to less- or non-polar compounds. The opposite applies to non-polar columns where separation order of e.g. alkanes follows the boiling point of the different species. The interaction force between the stationary phase and the sample is typically Van der Waals forces. The intermediate polar columns incorporate elements from both polar-and non-polar columns, and are used to provide a complementary separation for substances that fall between the two other groups [38]. Separation of compounds can also be performed through a column called a Molsieve, which has a zeolite molecular sieve that separate species according to size. This type of column is typically used for separation of gases, such as H₂, CH₄, CO, O₂ and N₂ [39].

The length of the column effects the separation efficiency of the sample, and it is common to see tubes up to 100 m. However, at this length the sample is often more complex and requires a long separation time. For less complex samples, it is often enough to use a small column to provide the wanted result in a shorter amount of time [37]. The column efficiency is a measurement that describes the broadening of chromatographic band by using the chromatographic peak width. It is also known

as plate number (N) and it can be calculated from equation 2.7. A recorded GC-peak is illustrated in figure 2.11 to show the principle behind quantitative analysis with GC. The recorded peak signal corresponds to the area of the peak found by integration, in addition the integration area is limited by two set boundaries. A calibration curve translates the obtained signal into a known unit of measure, e.g. concentration [40].

$$N=16 \left(\frac{t_R}{w_b} \right)^2 \quad (2.7)$$

Where:

- t_R = peak retention time
- w_B = the base width of the peak

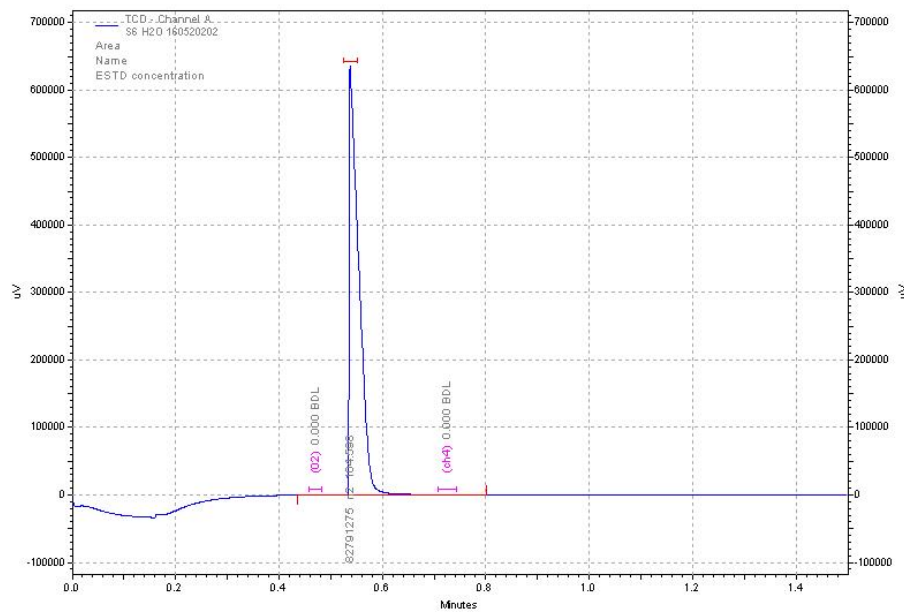


Figure 2.11.: Illustration of GC peak obtained by analysing gas composition which contain N_2 , O_2 and CH_4 .

2.4.6. Thermogravimetric Analysis

Thermogravimetric Analysis (TGA) is a thermal analysis which measures changes in mass of a sample as a function of temperature [41]. The method can be utilized to determine composition, decomposition temperature, impurities and moisture content. Further, the principles are based on mass measurements of a sample which is held at a constant temperature, heated or cooled in a specific atmosphere. The sample is located on a highly sensitive balance, while a constant flow of inert gas purges the atmosphere. Different samples and analysis require distinct types of gas, and it is possible to use ambient atmosphere, vacuum or a reactive purge gas such as oxygen. Further, combination between TGA and other well-established methods e.g. Differential Scanning Calorimetry (DSC) and Mass spectroscopy (MS) is possible. Typical is MS combined with TGA to identify chemical species that are purged out of the system [42]. When combined with DSC, the highly sensitive scale pan is replaced with a DSC sensor. Moreover, the principle of DSC is based on measurements of energy adsorption and desorption that occur in the sample when it is heated or cooled, thus exothermic and endothermic reactions together with phase transitions can be studied. The combination between TGA and DSC provides many different measurement options that open up to many possibilities, for example, carbon deposits studies [43].

2.4.7. Temperature Programmed Reduction

Temperature-Programmed Reduction (TPR) is a characterization method that is used for analysing the reducing properties of catalysts. Through the analysis, the sample is reduced with H_2 , CO or NH_3 simultaneously as the temperature increases. In general, H_2 is the most common gas used, and the reducing reaction between metal oxide and hydrogen to form metal M and steam can be presented according to equation 2.8.



One of the main principles behind the method is based on the ability to remove vapour quickly from the reaction zone. In a thermodynamic perspective, the Gibbs free energy for reduction, ΔG^0 , is negative for several oxides, allowing them to be reduced and form a TPR profile. However, ΔG^0 can also be positive, but when water is efficiently removed at elevated temperatures as seen in reaction 2.9, P_{H_2O} are held at a low value. The result can be a negative value of $RT \log \left(\frac{P_{H_2O}}{P_{H_2}} \right)$ low enough to compensate the positive value of ΔG^0 , thus obtain TPR profiles of oxides with positive ΔG^0 values [44].

$$\Delta G = \Delta G^0 + RT \log \left(\frac{P_{H_2O}}{P_{H_2}} \right) \quad (2.9)$$

The TPR curve is dependent on heating rate, H_2 concentration, flow rate and active species content. The profile is easily changed with an alteration in one of the four parameters, hence it is very important

to inform about reaction conditions [45]. The NiCo_2O_4 -spinel is known to be a reducible oxide with a recognized TPR profile. However, supported on a carrier such as CeO_2 the profile is most likely changed due different structure that promotes or suppresses reduction [46].

The reduction mechanism can be explained using two different models known as Nucleation and Contracting sphere (core), an illustration is shown in figure 2.12. Nucleation is initiated with formation of small metal nuclei on the oxide particle, which slowly removes oxygen from the lattice structure due to reduction. The process continues with more and more rapid metal nuclei formation, and when the clusters encounter other clusters the growth expands through the particle. Later, the reduction rate decreases due to diffusion limitations as illustrated in figure 2.13.

In the contracting sphere model, the initiation step is recognised by rapid formation of a thin outer metal layer on the oxide particle. When lattice oxygen is removed, metal is slowly formed towards the core until the particle is completely reduced [44].

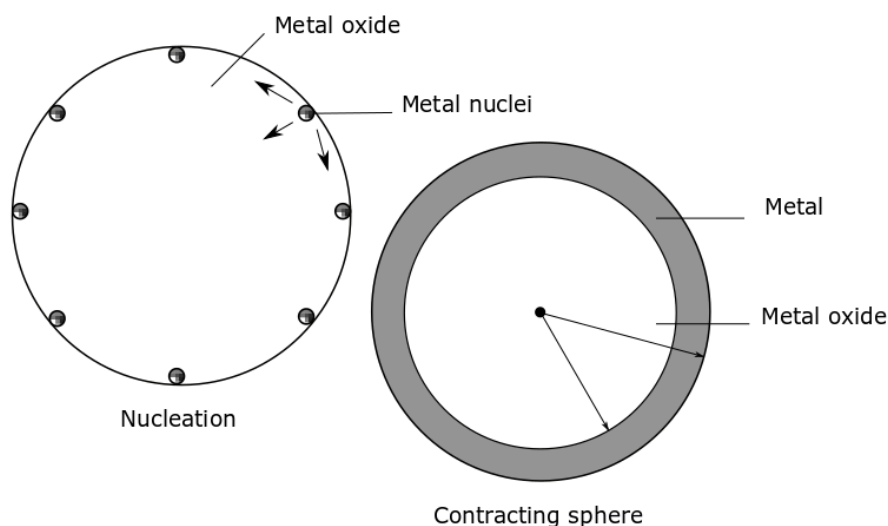


Figure 2.12.: Reduction mechanism of TPR illustrated by the Nucleation-and Contracting sphere models. Created with Inkscape [44].

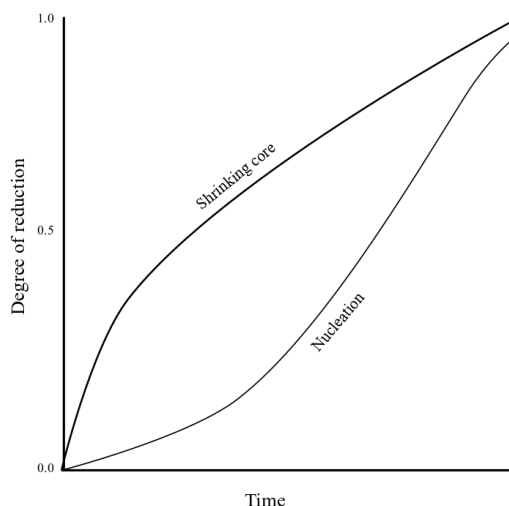


Figure 2.13.: Reduction rate illustration of the shrinking core-and nucleation models. Common to these two models is the reduced reduction rate due to diffusion limitations. The figure is created in Inkscape [34].

2.5. Catalytic Activity

The catalytic activity is a difficult phenomenon to quantify and there are several methods to do so. The most accepted and recommended measure of activity is through calculation of the turnover frequency (TOF). This is the number of molecules that react per active site and per unit time. The method requires knowledge of the catalyst and the nature of the active site, and it is often calculated from the measured rate of reaction. Another way that will be further described in the following, is to use the conversion achieved under specific reaction conditions as a measurement of activity. It is important to note that this type of measurement only provides an indication about the activity because the method is not informative.

2.5.1. Calculation of Methane Conversion

The activity and efficiency of synthesized catalysts can be indicated by the conversion of methane X_{CH_4} , and the expression can be seen in equation 2.10.

$$X_{CH_4} = \frac{F_{CH_4,in} - F_{CH_4,out}}{F_{CH_4,in}} \quad (2.10)$$

The feed stream and the outgoing methane stream can be calculated from equation. 2.11.

$$F_{CH_4} = y_i \cdot F_{tot \cdot i}, \quad i = in \text{ or } out \quad [ml \text{ min}^{-1}] \quad (2.11)$$

y_i is the proportion of methane, and it can be calculated from equation 2.12, where A_i is the peak area and K_i is the response factor of the GC.

$$y_i = A_i \cdot K_i \quad (2.12)$$

The final expression for methane conversion seen in equation 2.13 is given by inserting equation 2.11 into equation 2.10.

$$X_{\text{CH}_4} = \frac{y_{\text{CH}_4,\text{in}} F_{\text{tot},\text{in}} - y_{\text{CH}_4,\text{out}} F_{\text{tot},\text{out}}}{y_{\text{CH}_4,\text{in}} F_{\text{tot},\text{in}}} \quad (2.13)$$

The total flow in or out of the system can be calculated with respect to the inert flow F_{N_2} , as seen in equation 2.14 and equation 2.15.

$$F_{\text{tot},\text{in}} = \frac{F_{\text{N}_2,\text{in}}}{y_{\text{N}_2,\text{in}}} \quad (2.14)$$

$$F_{\text{tot},\text{out}} = \frac{F_{\text{N}_2,\text{out}}}{y_{\text{N}_2,\text{out}}} \quad (2.15)$$

Since N_2 is an inert gas the amount of the gas going in the system is equal to the amount going out, and it can be expressed as equation 2.16.

$$F_{\text{N}_2,\text{in}} = F_{\text{N}_2,\text{out}} \quad (2.16)$$

By introducing equation 2.14-2.16, the final conversion expression can be simplified from equation 2.13 into equation 2.17.

$$X_{\text{CH}_4} = 1 - \frac{y_{\text{CH}_4,\text{out}}}{y_{\text{CH}_4,\text{in}}} \cdot \frac{y_{\text{N}_2,\text{in}}}{y_{\text{N}_2,\text{out}}} \quad (2.17)$$

2.5.2. Carbon Error

The validity of the methane conversion can be examined by the systems carbon balance. If all of the carbon produced during the reaction is converted into CO_2 , then equation 2.18 would be valid.

$$F_{\text{CH}_4,\text{in}} = F_{\text{CH}_4,\text{out}} + F_{\text{CO}_2,\text{out}} \quad (2.18)$$

The carbon balance error, E_C , is a measure of fault in the carbon balance, and it can be calculated according to equation 2.19.

$$E_C = 100 \% \cdot \left(1 - \frac{F_{\text{CH}_4,\text{in}}}{F_{\text{CH}_4,\text{out}} + F_{\text{CO}_2,\text{out}}} \right) \quad (2.19)$$

Equation 2.20 can then further be simplified by previous derived relationships into equation 2.20.

$$E_C = \left(1 - \frac{y_{\text{CH}_4,\text{in}}}{y_{\text{N}_2,\text{in}}} \cdot \frac{y_{\text{N}_2,\text{out}}}{y_{\text{CH}_4,\text{out}} + y_{\text{CO}_2,\text{out}}} \cdot 100 \% \right) \quad (2.20)$$

2.6. Kinetics

The rate of a catalytic reaction is described by a kinetic framework that is regulated through measurable parameters such as pressure, temperature and concentration. A catalytic reaction consists of many subsequent reactions, and it may be difficult to establish a detailed understanding of the process in its entirety. The Langmuir-Hinshelwood (LH) -and the Mars-Van-Krevlen model can be used to describe the reaction mechanisms and make it possible to compare different catalytic systems. For

instance, the LH-kinetics assumes that all reacting species is adsorbed to the catalytic surface before any reaction occurs. This means that all reacting species are in thermal equilibrium with the surface and that the compounds react in a chemisorbed state [25]. By assuming that methane oxidation is a first-order reaction in terms of CH_4 concentration, and the oxygen concentration on the surface is constant and the counter reaction is neglected, then the reaction rate can be expressed as equation 2.21.

$$r = \frac{GHSV_{\text{act.m}}}{V_m} \eta X, [\text{mol h}^{-1} \text{g}_{\text{act} \cdot \text{cat}}^{-1}] \quad (2.21)$$

Where:

- V_m is volume of ideal gas (22414 ml mol⁻¹)
- η is mol % of CH_4 in the feed
- X is the conversion of CH_4
- $GHSV_{\text{act.m}}$ is the gas-hourly space velocity calculated in terms of active material, and it can be expressed from equation 2.22.

$$GHSV_{\text{act} \cdot \text{m}} = \frac{F_{\text{Tot}}}{m_{\text{act}}}, [\text{ml h}^{-1} \text{g}_{\text{act} \cdot \text{cat}}^{-1}] \quad (2.22)$$

3. Experimental

In the following section, experimental work done during the dissertation period will be presented. The risk associated with experimental equipment and each operation, as well as the new risk associated with the Covid-19 pandemic, was assessed through the NTNU risk assessment protocol. And further approved by the department before any experiments were performed. A complete review of the assessment can be reviewed through NTNU's risk assessment portal with ID number 34736, or in attachment F.

3.1. Synthesis of Catalysts and High Surface Area Ceria Support

During the synthesis of catalysts in this project, Nickel(II)nitrate hexahydrate (SIGMA-ALDRICH) and Cobalt(II)nitrate hexahydrate (SIGMA-ALDRICH) were used as source to Ni and Co. Furthermore, Cerium(IV)oxide(5 Micron Powder, Alfa Aesar) was used as the source of low surface area ceria, CeO_2/L .

The synthesis procedure was started by weighing approx. 2.5 g CeO_2/L . Based on the desired weight %, the amount of $\text{Ni}(\text{NO}_3)_2 \cdot 6 \text{H}_2\text{O}$ and $\text{Co}(\text{NO}_3)_2 \cdot 6 \text{H}_2\text{O}$ was calculated and weighed into a sample container (2 ml). This formed the base of the IWI impregnation solution which was finalized by dissolving the nitrates in distilled H_2O . The amount of water used was based on the solubility of the substances. Appendix A shows a calculation example as well as a complete overview of the calculations made according to the syntheses.

Impregnation of the support material was stepwise performed by pipetting 0.2 ml of the IWI solution over the material. Further, to ensure a dry consistency between each impregnation, the catalysts were dried at 50 °C for 1 hour. After the last impregnation, the catalyst was dried at 120 °C for 24 hours.

In table 3.1 the catalysts synthesized on low and high surface area CeO_2 can be seen. The table also includes nominal active material load and amount of active material used. The samples are named according to nominal active material load, support material used and synthesis order. After impregnation and drying, the samples became calcinated in a standard quartz calcination reactor with a maximum temperature of 550 °C, ramp rate of 2 °C min^{-1} , dwell at 6 h and with air as calcination gas.

Table 3.1.: wt % active material, amount of support, nickel and cobalt used for the synthesis of catalysts.

ID	wt % _(act)	m _(act) [g]	m _(CeO₂) [g]
6.0NiCoO/CeO ₂ /L-S3	6.026	0.161	2.509
5.7NiCoO/CeO ₂ /L-S4	5.657	0.154	2.563
6.5NiCoO/CeO ₂ /L-S5	6.475	0.175	2.528
6.6NiCoO/CeO ₂ /L-S6	6.593	0.183	2.593
6.5NiCoO/CeO ₂ /H-S7	6.519	0.178	2.546

(H): Synthesized on high surface area support

(L): Synthesized on low surface area support

High surface area ceria support was synthesized with the Sol-gel method, where Cerium(III)nitrate Hexahydrate (Fluka) was used as ceria source and Sodium hydroxyde(VWR Chemicals) was used to create the alkaline reaction environment. In table 3.2 the mass and the mixing ratio between Ce(NO₃)₃, NaOH and H₂O is shown. NaOH was dissolved in distilled H₂O, and the solution was placed on a stirring plate and stirred constantly during the whole process. Ce(NO₃)₃ was weighed out and transferred into the alkaline solution. A switch in colour from clear to purple indicated the presence of Ce³⁺ according to equation 2.1. The reaction was left for 2 hours until another colour change occurred, from purple to yellow, indicating precipitation of CeO₂. After precipitation, the solution was filtered and the solids was washed with distilled H₂O until the pH was neutral. Drying of the material was performed at 50 °C for 24 hours.

Table 3.2.: Molar mixing ratio and amount of Ce(NO₃)₃, NaOH and H₂O used during synthesis of high surface area CeO₂.

Substance	# mol	m [g]
Ce(NO ₃) ₃	0.15	50
NaOH	1.02	41
H ₂ O	22.73	410
Ce(NO ₃) ₃ /NaOH	0.15	
NaOH/H ₂ O	0.045	

Further, the synthesis of NiCo₂O₄ on high surface ceria was performed with the IWI method as previously described. The only difference between those two preparations was the number of impregnation steps. For high surface area CeO₂, one impregnation step was sufficient.

3.2. Characterization

Characterization techniques used for examination of catalysts properties such as XRF, N₂-physisorption and Raman spectroscopy and the experimental execution details are described further in the section.

3.2.1. X-Ray Fluorescence - Bulk Composition

The substance composition of every synthesised catalyst, including ceria with high surface area, was verified with XRF analysis. The experiment was performed in a Rigaku Wavelength Dispersive X-ray Fluorescence Supermini 200 Analyzer (WDXRF) with a Pd anode as X-ray source (50 kV, 200 W). Starting point for sample processing was to create a pellet of 2.5 -3 g boric acid, H₃BO₃. About 100 -200 mg of sample material was then distributed over the pellet and pelletized for 2 min at a pressure of 10 ton. After pressing, the pellet was transferred over to a 6 μm polypropylene film and placed in a 40 mm sample holder. Then the sample was loaded onto an autosampler disc and analysed. To ensure good accuracy and quality of analysis some of the samples were analysed multiple times. Table 3.3 shows the amount of boric acid and sample used.

Table 3.3.: Amount of sample material and boric acid used for analysis of sample composition.

ID	m _{H₃BO₃} [g]	m _{sample} [g]
6.0NiCoO/CeO ₂ /L-S3	3.09	0.1019
5.6NiCoO/CeO ₂ /L-S4	3.22	0.1580
6.5NiCoO/CeO ₂ /L-S5	3.01	0.1046
6.6NiCoO/CeO ₂ /L-S6	3.00	0.1505
6.5NiCoO/CeO ₂ /H-S7	3.05	0.1106
CeO ₂ /H	3.11	0.1215

3.2.2. Raman Spectroscopy

For structural fingerprint identification of NiCo₂O₄ and carbon in the samples a Horiba Jobin Yvon-LabRam spectrometer with a HeNE ($\lambda = 632.8$ nm) laser was used. The sample was powdered and loaded onto a sample slide before it was placed beneath the laser source. Standard analysis parameters used for spinel and carbon analysis can be seen in table 3.4.

Table 3.4.: Analysis parameters used during identification of NiCo₂O₄ and carbon in samples using Raman.

	NiCo ₂ O ₄	Carbon
Range [cm ⁻¹]	100 -1000	100 - 3000
Accumulation	4	4
Acc. Time [min]	4	12
Filter [%]	10	10
Hole	200	200

3.2.3. X-Ray Diffraction – Investigation of Crystalline Phases and Crystal Size

X-ray diffraction was performed to examine crystallite size and crystalline phases of synthesized samples and support material. A Bruker D8 A25 DaVinci X-ray Diffractometer with $\text{CuK}\alpha$ radiation ($\lambda = 1.5406 \text{ \AA}$) and a LynxEyeTM SuperSpeed Detector was used during the experiment, and the analysis parameters can be seen in table 3.5. DIFFRAC EVA was used to evaluate the resulting spectrums, and the crystallite size were calculated using the peak search program, and with the FWHM parameter.

Table 3.5.: Analysis parameter used for analysis of samples using XRD.

2θ [$^\circ$]	15-75
Time [min]	60
Step Change [$^\circ \text{ step}^{-1}$]	0.044
Permanent slit [mm]	0.3

3.2.4. N_2 - Physisorption - Surface Area and Pore Size Distribution

N_2 - physisorption analysis of synthesized samples was performed in a N_2 -Physisorption micrometrics TriStar II 3020 device. Before examination, the individual weight of the empty sample tubes and the combined weight of samples and tubes was measured. The amount of sample material used corresponded to a total surface area of 30 m^2 . Depending on the support material, if it had low or high surface area, the sample mass ranged between 200 – 600 mg. After sample preparation, degasification was performed in a VacPrep 061 degasser in two stages. To start with, the samples were left at room temperature for one hour at a pressure below 100 mmHg. In stage two, the tubes were moved to a hot chamber with a temperature at $200 \text{ }^\circ\text{C}$ and left for 24 hours. Table 3.6 shows an overview over the combined weight of samples and tubes before and after degasification.

Table 3.6.: Weight of test tubes and total weight of test tubes and samples before and after degassing.

ID	$m_{(T+S)}$ [g]	$m_{(T)}$ [g]	$m_{(T+S \text{ degas})}$ [g]
CeO_2/H	26.1231	25.9796	26.1202
6.5NiCoO/ $\text{CeO}_2/\text{H-S7}$	25.7957	25.4892	25.7906
6.5NiCoO/ $\text{CeO}_2/\text{H-S7}^*$	26.0311	25.7857	26.0254

* After reaction

After degasification the weight of the sample tubes was again measured, and the sample mass was corrected. The tubes were attached to the TriStar and an isotherm-container with liquid N_2 was placed beneath. Analysis of BET surface area, BJH pore size and distribution was performed, and the data collected was treated in Excel and SigmaPlot.

3.2.5. TPR

To examine the reduction capabilities of the synthesized catalysts, TPR was used. The experiments were carried out in a BenchCAT Hybrid 1000 HP instrument, with the analysis parameters shown in Table 3.7. The reaction itself was performed in a standard TPX quartz reactor, and figure 3.1 shows the temperature program used during the analysis where the measurements were carried out between 100 - 1000 °C.

Table 3.7.: Standard analysis parameters and sample amount used to analyse the reducing properties of synthesized samples and support.

ID	m _{sample} [g]	H ₂ / Ar [%]	Flow [ml min ⁻¹]	Heating rate [°C min ⁻¹]
6.5NiCoO/CeO ₂ /L-S5	0.1525	7	20	10
6.5NiCoO/CeO ₂ /H-S7	0.1650	7	20	10
6.5NiCoO/CeO ₂ /H-S7*	0.1592	7	20	10
CeO ₂ /H	0.1498	7	20	10
CeO ₂ /L	0.1493	7	20	10

* After reaction

Preparation of samples was carried out in three steps. First, a small amount of quartz wool was placed in the bottom of the reactor. Subsequent steps included transfer of approx. 150 mg sample to the reactor. In the final step, a small amount of quartz wool was placed over the sample, figure 3.2 showing how the sample was packed in the reactor. After the pretreatment, the reactor was placed in the analyser. Gaskets and connections were secured so there were no leaks. To verify this, several leakage tests were conducted using leakage foam and sniffer detector. The tests were carried out with nitrogen and hydrogen as feed stream. After the analysis, the test results were processed in Excel and SigmaPlot.

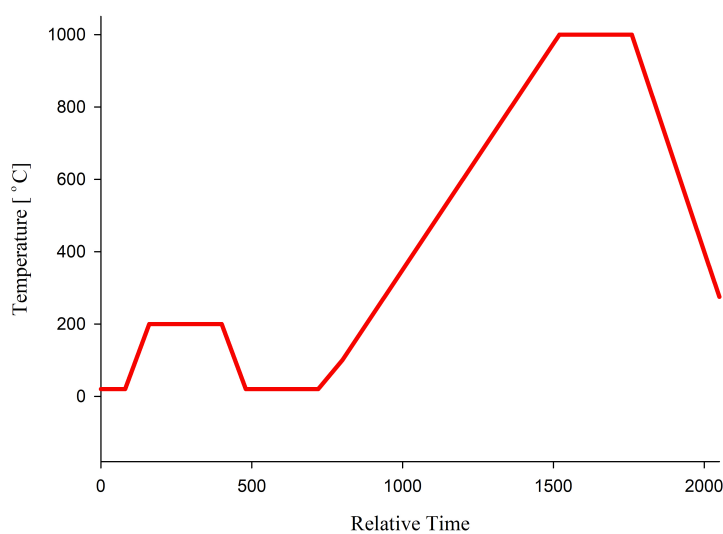


Figure 3.1.: Temperature program used for TPR analysis. Heating rate 10 °C min⁻¹ from the initiation of reduction steps

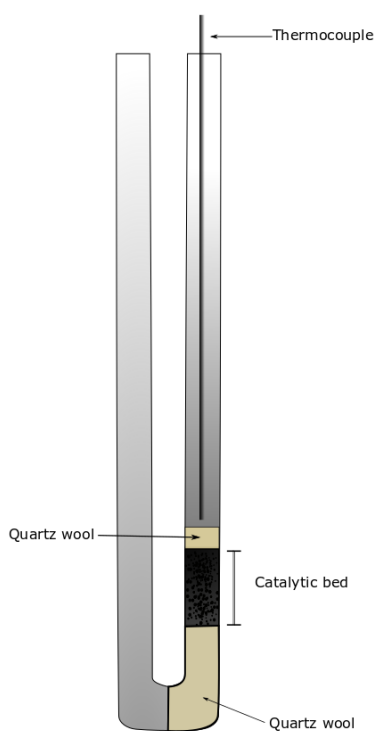


Figure 3.2.: Standard quartz reactor used for temperature programmed reduction analyses.

3.2.6. TGA - Investigation of Carbon Deposits

One of the samples was examined for possible carbon deposits after completion of activity test using TGA. The test was performed by analysing ca. 10-20 mg sample in a Netzsch STA 449C Jupiter TGA / DSC. The purge stream that consisted of synthetic air and argon was analysed using Netzsch Aërlo's QMS 403C MS.

3.3. Activity Test

Testing of the synthesized catalyst was performed to give an indication about the capability to convert CH_4 into CO_2 and H_2O . The obtained results were further examined for signs of deactivation, formation of carbon and investigation of catalysts activity. Figure 3.3 shows a simplified flow sheet over the methane oxidation reaction rig 2.9 used during the experiments. The layout is built around a quartz reactor enclosed by an oven with gas streams going in and out of the system. The feed stream combination of CH_4 , N_2 and air was controlled by mass flow controllers, and the product stream composition was analysed by Agilent 3000 A μ GC.

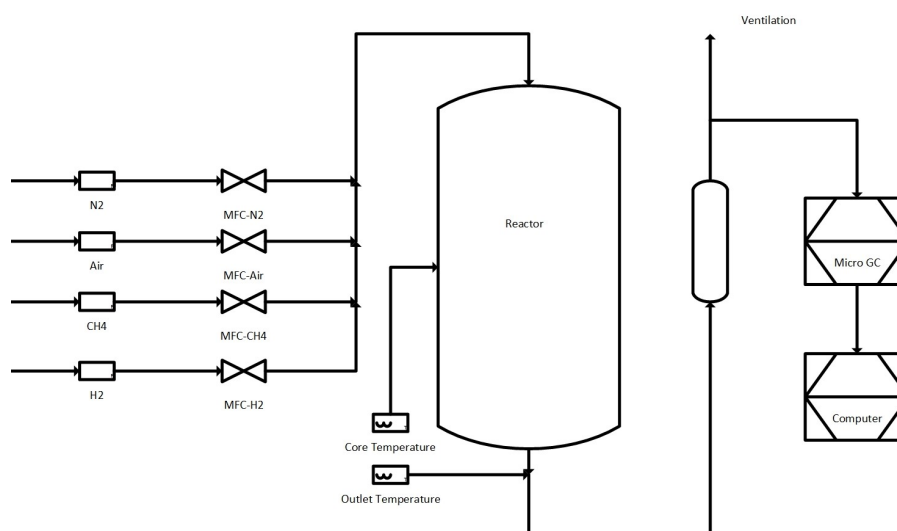


Figure 3.3.: Flow sheet over rig 2.9, created in SmartArt.

Conduction of the activity test was initiated by a size selection step to ensure uniform catalysts particle size between 212-425 nm. The size of particles larger than 425 nm was reduced by a mortar, and smaller particles were pelletized before passed through a custom grid sieve. Further, about 0.5 g of catalysts material was diluted with 1.5 g SiC and loaded into the reactor. SiC was applied to prevent bypass and creation of hot spots in the reactor bed. In figure 3.4 a sketch of the quartz reactor can be seen.

After loading of the sample, the reactor was placed in the oven and covered with insulation material to reduce heat loss. The feed stream-and product gas line was attached to the reactor and a thermocouple was placed flush with the catalyst bed. To safeguard health and safety, leakage tests with N_2 and H_2 was performed, which indicated if the pipe connection joint were tight or not. Table 3.8 shows the standard flow parameters used during the experiment.

The temperature program used in the activity test can be seen in figure 3.5 The obtained data from the micro GC was further treated with MatLab and SigmaPlot.

Table 3.8.: Standard flow parameters for rig 2.9

Gas	Flow [ml min ⁻¹]	Set point [%]
CH ₄	4	24.51
N ₂	100.75	15.16
Air	95.25	91.40

Since exhaust gas contains water, it was decided to perform wet reaction tests on the catalysts 6.5NiCoO/CeO₂/L-S5, 6.6NiCoO/CeO₂/L-S6 and 6.5NiCoO/CeO₂/H-S7. The reaction conditions are shown in Table 3.9. It was decided to use 10 % H₂O in the feed, which corresponds to 20 ml min⁻¹. Several dry and wet tests were performed on the same sample to investigate the effect of water. In addition, a long-term analysis , 72 hours, at constant temperature, T = 450 °C, was performed for each of the catalysts mentioned, to see how it behaved over time.

Before the experiments was performed, a new liquid flow controller was installed and calibrated. To create a calibration curve, three different set points, which are shown in Appendix C table D.1, were used. The calibration was performed by weighing an empty container and placing it at the outlet of the controller. After a given period, the container was weighed again, and the amount of water over time calculated. Then, the Set point was plotted against the calculated liquid flow and the calibration curve created. The curve and calculation of the amount of steam are shown in the appendix C.

The analysis was performed in accordance with what has been described for the activity test previously. The only difference was that steam was introduced at 200 °C while reducing the N₂ flow down to 80 ml min⁻¹. The steam stream was presented by passing the nitrogen stream through a preheater which generated steam from the water line. The other significant difference was that the gas lines were heated to 150 °C to prevent condensation.

Table 3.9.: Flow parameters for H₂O activity tests

Gas	Flow [ml min ⁻¹]	Set point [%]
CH ₄	4	24.51
N ₂	80.75	12.46
Air	95.25	91.40
H ₂ O	20	0.96 g h ⁻¹

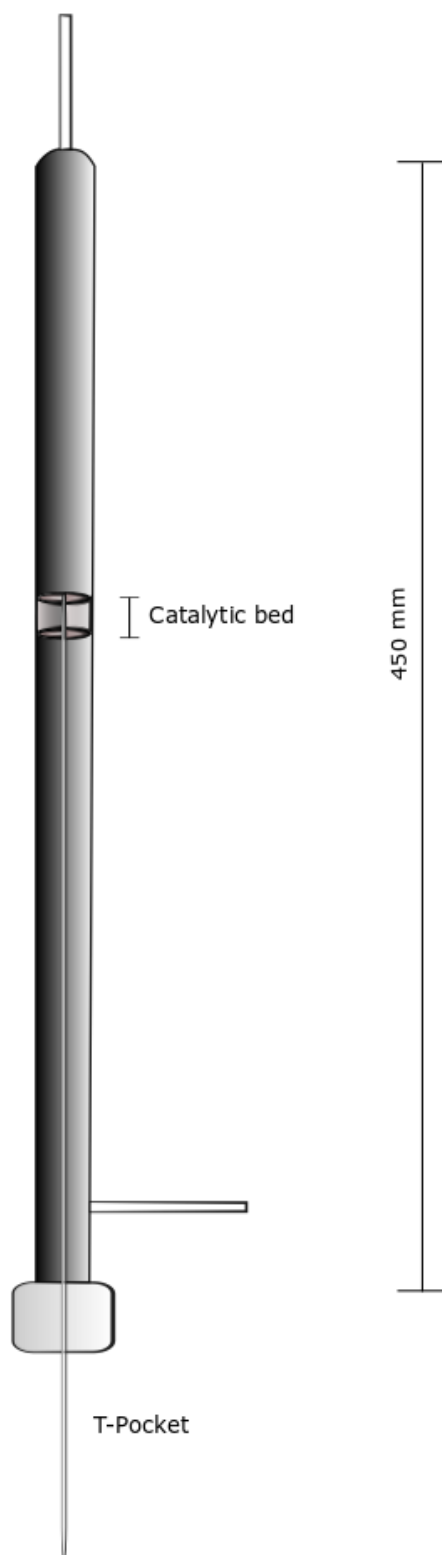


Figure 3.4.: Simplified illustration of quartz reactor made in Inkscape

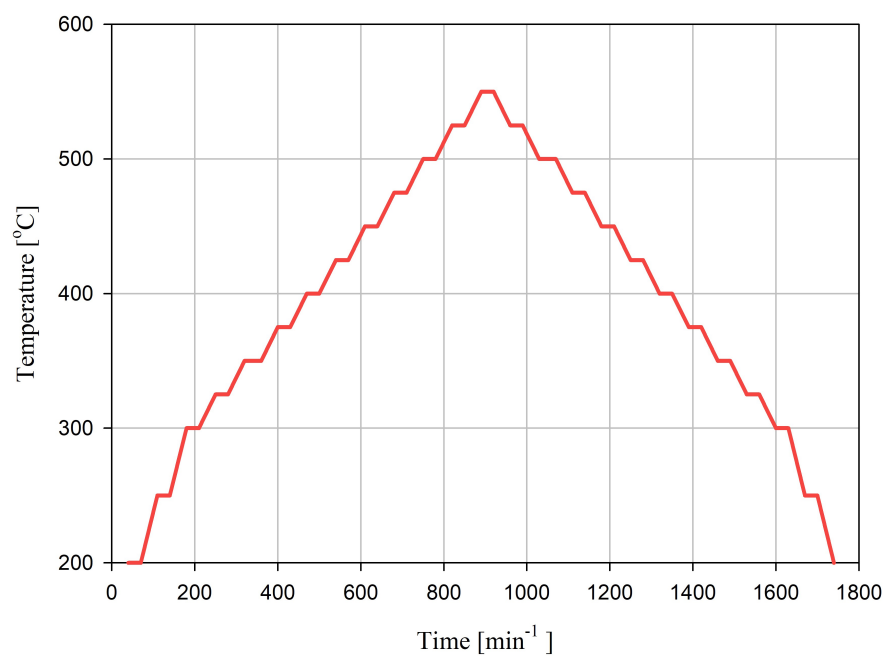


Figure 3.5.: Temperature program used during activity test. Illustration created in SigmaPlot

4. Results

The first part of this chapter deals with the various characterization techniques used to study the structure and composition of the catalysts. Further, activity and stability studies performed on the catalysts will be presented. Some of the results that are presented have been produced during the specialization project, and some are provided by SINTEF, but this is noted when they are applied. In addition, references will also be made to measurement results and calculations in appendix when appropriate.

4.1. XRF-Composition

Table 4.1 lists the results obtained from measurements using XRF. The deviation between measured and nominal value is indicated as d [%]. It should be noted that the deviation varies considerably in relation to the nominal value. A calculation example can be seen in appendix A.

Table 4.1.: XRF composition and deviation (d) from nominal NiCo oxide content in catalysts supported on high and low surface area CeO₂.

ID	Nominal value	wt % Act. Material _(NiCo oxide)	molar ratio _(Ni/Co)	d [%]
6.0NiCoO/CeO ₂ /L-S3	6.0	4	0.6	-33
5.7NiCoO/CeO ₂ /L-S4	5.7	3	0.4	-47
6.5NiCoO/CeO ₂ /L-S5	6.5	7	0.5	8
6.6NiCoO/CeO ₂ /L-S6	6.6	5	0.5	-24
6.5NiCoO/CeO ₂ /H-S7	6.5	8	0.6	23

4.2. N₂ - Physisorption - BET/BJH

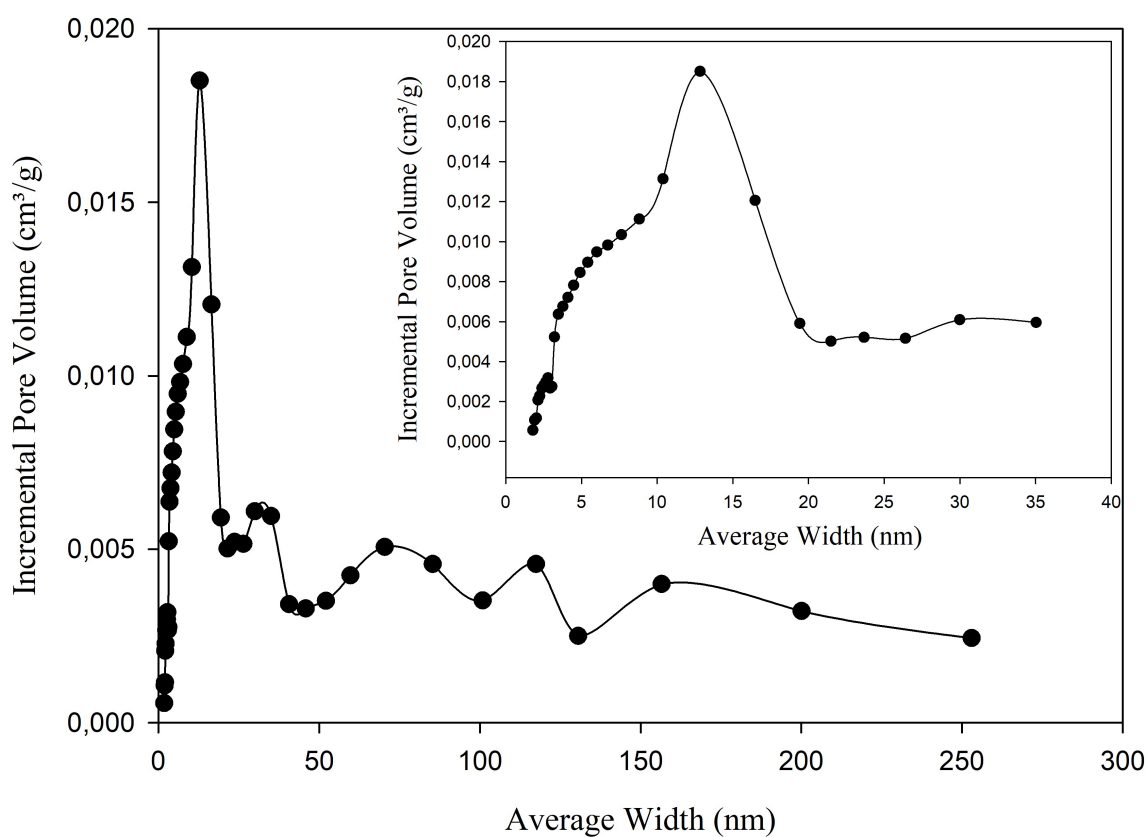
The results obtained from the N₂ - physisorption tests are shown in table 4.2. It is noted that synthesized support, CeO₂/H, has 25 times the S_{BET} area compared to CeO₂/L, which is a commercially available material with low surface area. Furthermore, the table shows the analysis result from a catalyst that were synthesized on high surface area CeO₂. Comparison of S_{BET} for the support material and the catalyst shows a reduction which indicates that the support is supplied with active material. In addition, the S_{BET} measurement of the catalyst made after reaction can also be viewed. It is pointed out that the area is reduced during activity experiment with the following reaction conditions: $T = 200\text{-}550$ °C, $F_{\text{CH}_4} = 4$ ml min⁻¹, $F_{\text{N}_2} = 100$ ml min⁻¹, $F_{\text{Air}} = 96$ ml min⁻¹ for 16 hours. The table also contains the measurement result for the catalyst 6.3NiCoO/CeO₂/L-S1 which was synthesized during the specialization project.

Table 4.2.: N₂- physisorption measurement results of CeO₂/H and CeO₂/L with and without NiCo₂O₄

ID	S _{BET} [m ² g ⁻¹]	V _p [cm ³ g ⁻¹]	Average pore diameter [nm]
CeO ₂ /H	156	0.05	12.01
CeO ₂ /L	6.12	-	-
6.3NiCoO/CeO ₂ /L-S1	5.83	-	-
6.5 NiCoO/CeO ₂ /H-S7	100	0.03	-
6.5 NiCoO/CeO ₂ /H-S7*	83.2	-	-

* After reaction

The pore distribution on synthesized high surface area CeO₂/H indicates an average value of 12 nm as shown in figure 4.1. It is noted that this may indicate a more porous structure compared to CeO₂/L where it was not possible to obtain a meaningful distribution.

**Figure 4.1.:** Pore distribution over synthesized high surface area ceria, CeO₂/H. measured by N₂ adsorption desorption at 77.35 K.

4.3. Raman

A Raman spectra, which compares CeO_2/L and CeO_2/H with and without NiCo_2O_4 can be viewed in figure 4.2. It is noted that NiCo_2O_4 spinel is indicated at $188 - 192 \text{ cm}^{-1}$ and $644 - 660 \text{ cm}^{-1}$ [15][16]. The peak at $457 - 475 \text{ cm}^{-1}$ indicates CeO_2 . Furthermore, it is noted that the Co vibration for CeO_2/L , at $188-192 \text{ cm}^{-1}$, is much more pronounced than for CeO_2/H , which probably indicates an ordered structure.

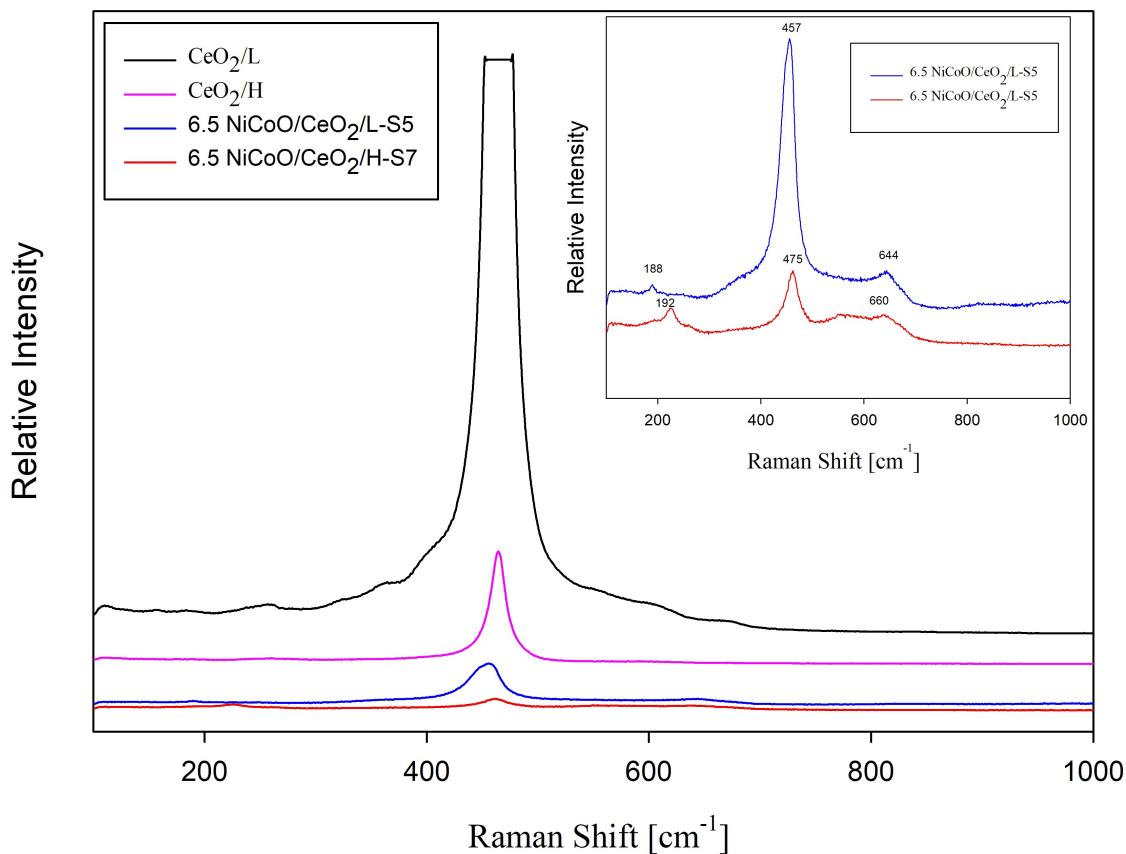


Figure 4.2.: Raman spectrum of sample $6.6\text{NiCoO}/\text{CeO}_2/\text{L-S5}$, $6.5\text{NiCoO}/\text{CeO}_2/\text{H-S7}$, CeO_2/H and CeO_2/L . Measurement parameters: Surface accumulation 4, Acc. time 4 min, filter 10 % and hole size = 200.

4.4. XRD

In figure 4.3 the XRD spectre for commercial low surface area and synthesised high surface area CeO_2 can be viewed. Further, CeO_2/H is recognised through smaller and broader peaks compared to low surface area CeO_2 . It is noted that the peak size of CeO_2/L varies somewhat, which may indicate that the precision of the analysis may be reduced due to large crystals. Table 4.3 contains calculated crystallite size from the XRD analysis, of which three of the peaks can be compared because they were found for both materials. In general, CeO_2/H has a crystallite size of approx. 4 nm, and CeO_2/L 40-60 nm.

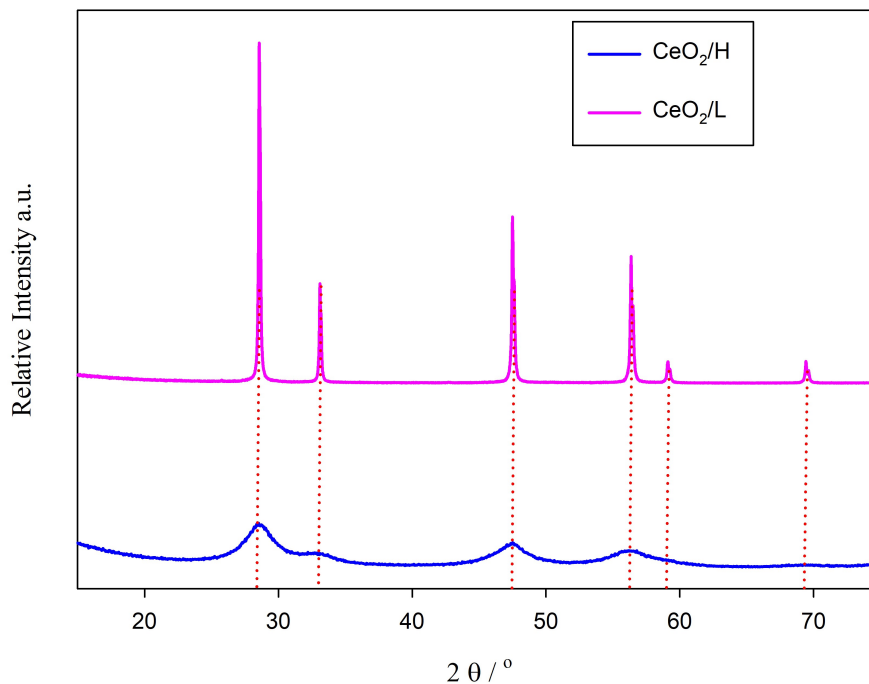


Figure 4.3.: XRD spectre of the samples CeO_2/H and CeO_2/L , where both samples used the following analysis parameters: $2\theta = 15-75^\circ$, time = 60 min, step change = $0.044^\circ\text{step}^{-1}$, permanent slit = 0.3 mm.

Table 4.3.: Calculated crystallite size for peaks found in the 2θ range $15-75^\circ$ for the support material CeO_2/H and CeO_2/L .

ID	2θ [$^\circ$]	k	d	FWHM [$^\circ$]	Crystallite size [nm]
CeO_2/H	28.509	0.89	3.128	2.063	4.4
	47.42	0.89	1.916	2.173	4.4
	56.218	0.89	1.635	2.789	3.6
CeO_2/L	28.579	0.89	3.121	0.15	61
	33.616	0.89	2.703	0.162	57
	47.983	0.89	1.912	0.205	47
	56.88	0.89	1.632	0.236	43
	59.553	0.89	1.562	0.252	40
	69.887	0.89	1.353	0.214	50

Figure 4.4 shows the XRD spectre for NiCo_2O_4 synthesised on high- and low surface area CeO_2 . Further, two of the catalysts that can be viewed are of the same kind, but they were examined before and after the activity experiment, figure 4.7a-4.7b, where the following reaction conditions were used: $T = 200\text{-}550\text{ }^\circ\text{C}$, $F_{\text{CH}_4} = 4\text{ ml min}^{-1}$, $F_{\text{N}_2} = 100\text{ ml min}^{-1}$, $F_{\text{Air}} = 96\text{ ml min}^{-1}$ for 16 hours. The crosses illustrate where nickel cobalt oxide was detected through a search and match database, with the PDF database 00-002-1074 and 04-019-6381. In addition, XRD spectre from all the other catalysts that were synthesized can be seen in Appendix B.3 figure B.6.

Table 4.4 contains calculated crystallite size for the peaks found in the area of $2\theta = 15\text{-}75\text{ }^\circ$. It is noted that the crystallite size of the catalyst based on CeO_2/H is much smaller relative to that based on commercial CeO_2/L . Furthermore, there is an increase in crystallite size after catalytic testing of the CeO_2/H based catalyst, which may suggest sintering during the reaction. In general, the catalysts based on high surface area CeO_2/H have a crystallite size of approx. 8-19 nm and 9-12 nm. For the catalyst supported by CeO_2/L , the size is approx. 40-54 nm.

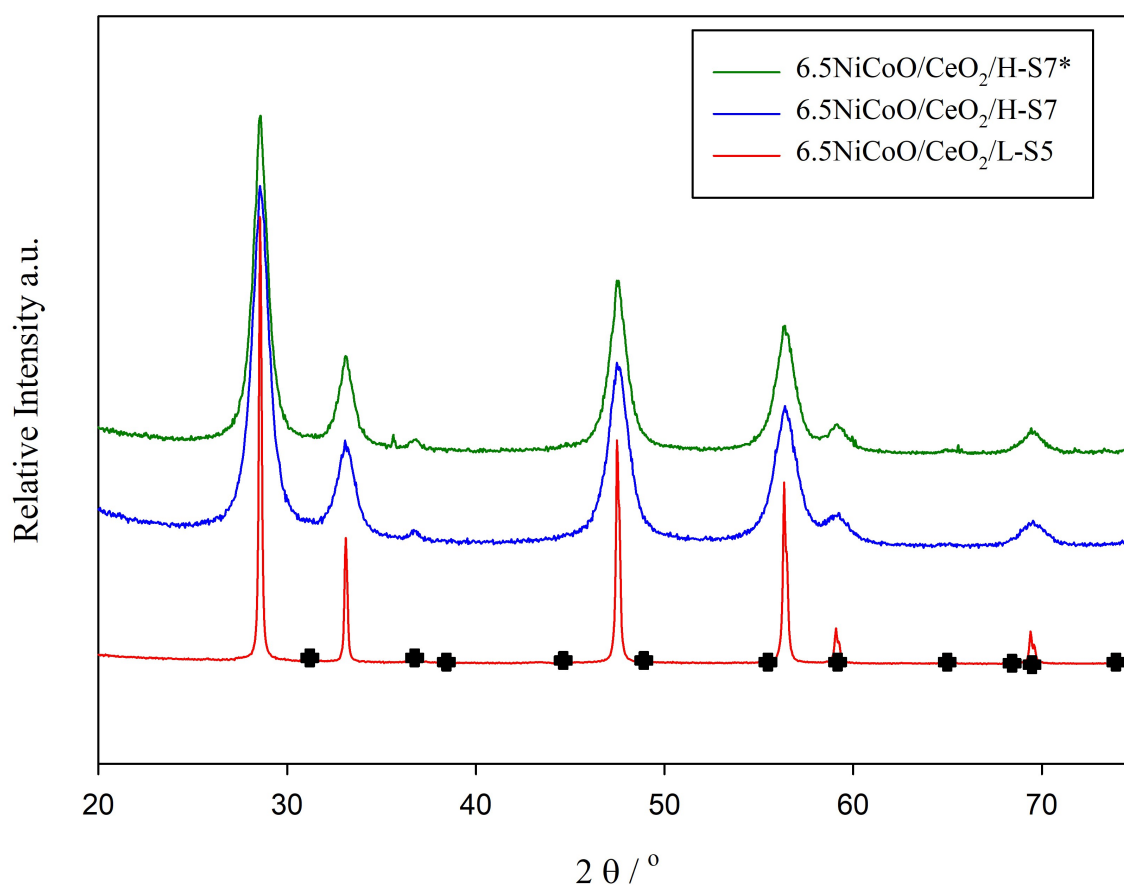


Figure 4.4.: XRD plot showing the results of the samples $6.5\text{NiCoO}/\text{CeO}_2/\text{L-S5}$, $6.5\text{NiCoO}/\text{CeO}_2/\text{H-S7}$ and $6.5\text{NiCoO}/\text{CeO}_2/\text{H-S7}^*$, where * indicates the sample is examined after the 2nd reaction. Cross indicates nickel cobalt oxide identified using PDF 00-002-1074 and PDF 04-019-6381. Analysis parameters: $2\theta = 15\text{-}75\text{ }^\circ$, time = 60 min, step change = $0.044\text{ }^\circ\text{step}^{-1}$, permanent slit = 0.3 mm.

Table 4.4.: Calculated CeO₂ crystallite size for the peaks found between $2\theta = 15-75^\circ$ for NiCo₂O₄ catalysts synthesized on high-and low surface area CeO₂.

Sample ID	2θ [°]	k	d	FWHM [°]	Crystallite size [nm]
6.5NiCoO/CeO ₂ /H-S7	28.596	0.89	3.119	1.022	8.9
	33.122	0.89	2.702	0.978	9.4
	47.51	0.89	1.911	1.163	8.3
	56.388	0.89	1.630	1.253	8.0
	59.09	0.89	1.559	0.545	19
	69.506	0.89	1.350	1.375	7.8
6.5NiCoO/CeO ₂ /H-S7*	28.579	0.89	3.120	0.85	11
	33.109	0.89	2.703	0.815	11
	47.542	0.89	1.911	1.016	9.5
	56.411	0.89	1.630	1.083	9.3
	69.426	0.89	1.353	0.879	12
6.5NiCoO/CeO ₂ /L-S5	28.564	0.89	3.122	0.17	54
	33.1	0.89	2.704	0.182	51
	47.483	0.89	1.913	0.233	42
	56.34	0.89	1.631	0.25	40
	69.466	0.89	1.352	0.237	45

* After reaction

4.5. TPR

In figure 4.5, the temperature programmed reduction analysis of NiCo_2O_4 on CeO_2/H and CeO_2/L was compared to the reference reduction curve of pure NiCo_2O_4 , which is produced by SINTEF. Further, the experiment was performed with identical reaction conditions, but some deviation between the active material load must be taken in consideration. The result shows a lower initial reduction temperature for the catalyst synthesized on high surface area CeO_2 , as well as a steeper reduction curve indicating that the reduction is initiated faster. In contrast, the CeO_2/L based catalyst reduction curve is narrower relative to the one based on CeO_2/H , and additionally it shows the contour of three peaks and not two. Generally, both supported catalysts have a higher initial reduction temperature compared to the reference curve of NiCo_2O_4 . The TPR-profile of high and low surface area CeO_2 can be viewed in appendix B.4 figure B.7. Additionally the hump, which can be seen at 450 °C, is most likely caused by CeO_2 .

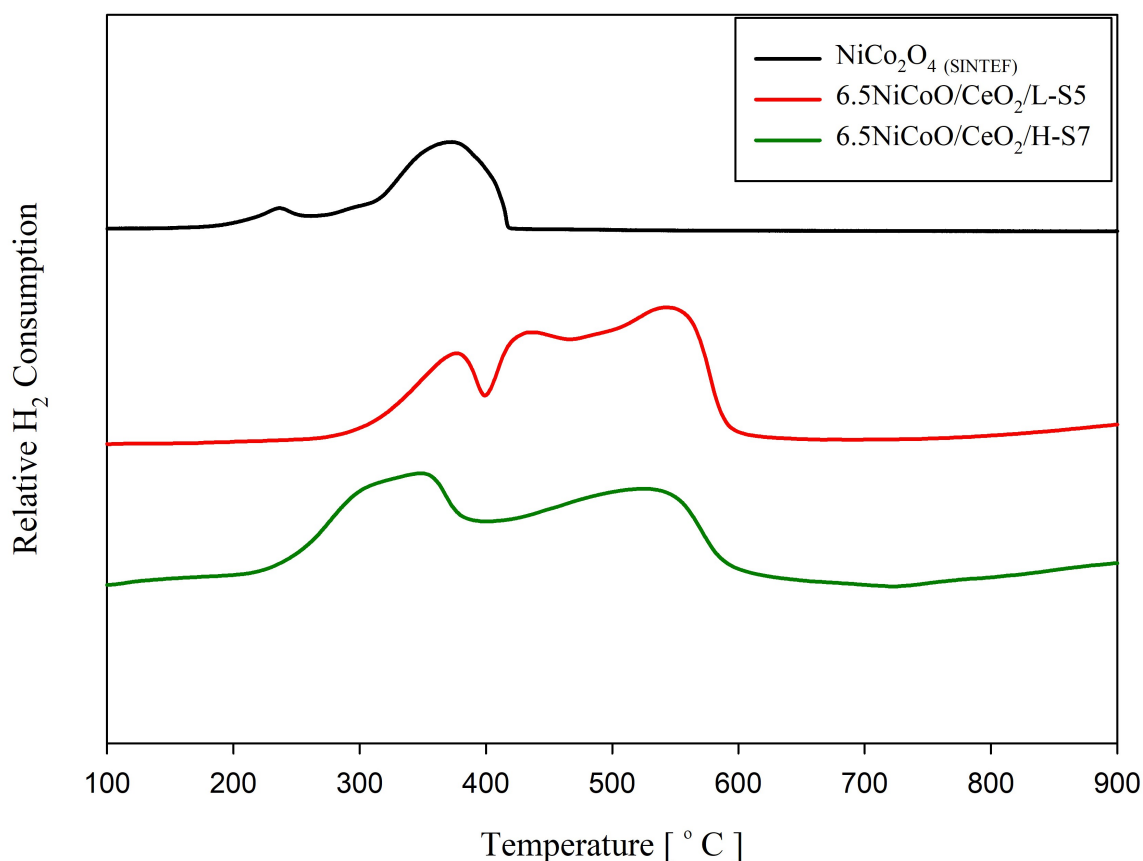


Figure 4.5.: TPR-profile of NiCo_2O_4 , and the catalysts supported by high- and low surface area CeO_2 . Reaction conditions: $\text{H}_2/\text{Ar} = 7 \%$, $F_{\text{H}_2/\text{Ar}} = 20 \text{ ml min}^{-1}$, heating rate = 10 °C min^{-1} , $\text{act.m}_{\text{NiCo}_2\text{O}_4(\text{SINTEF})} = 0.150 \text{ g}$, $\text{act.m}_{6.5\text{NiCoO}/\text{CeO}_2/\text{L-S5}} = 0.0108 \text{ g}$ and $\text{act.m}_{6.5\text{NiCoO}/\text{CeO}_2/\text{H-S7}} = 0.0127$.

4.6. Catalyst Activity

In Figure 4.6, is the reaction curve during heating for the 6.3NiCoO/CeO₂/L-S1 catalyst, which was synthesised during the specialisation project, compared to the catalyst 6.5NiCoO/CeO₂/L-S5. From the figure it is noted that the reaction curve obtained by the two catalysts suggests good reproducibility of the synthesis.

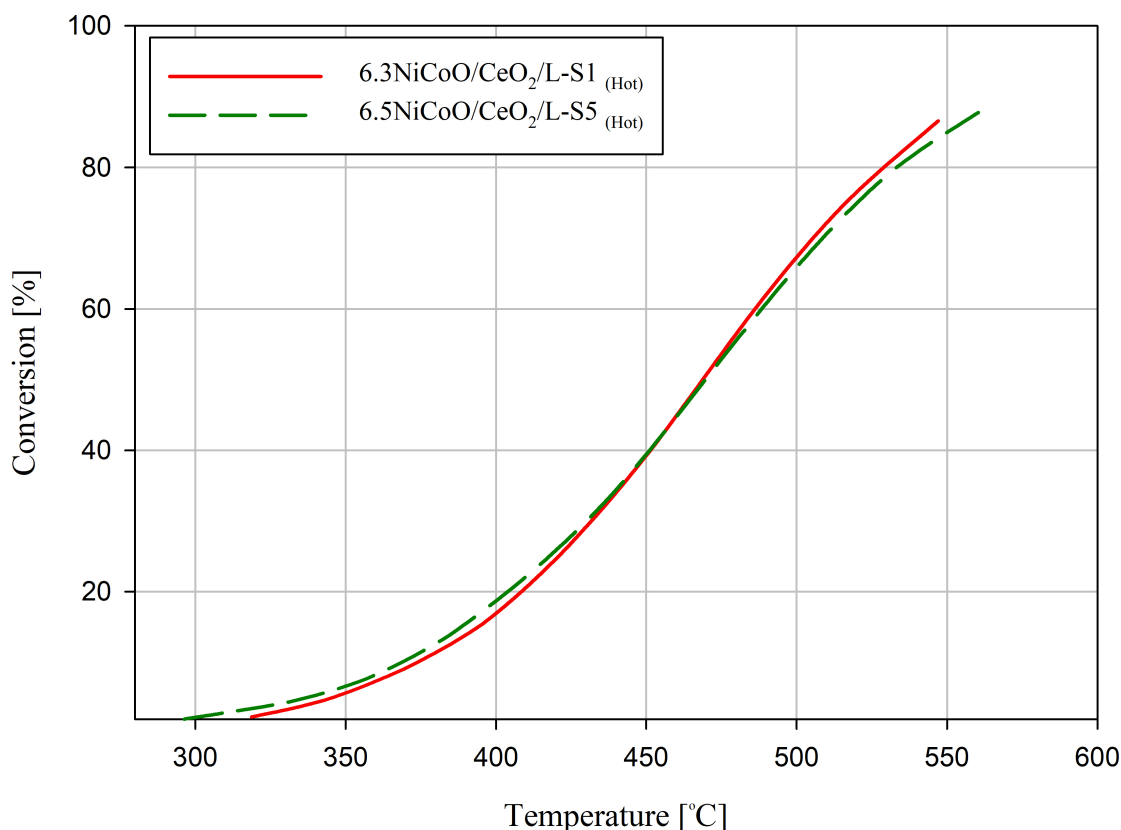
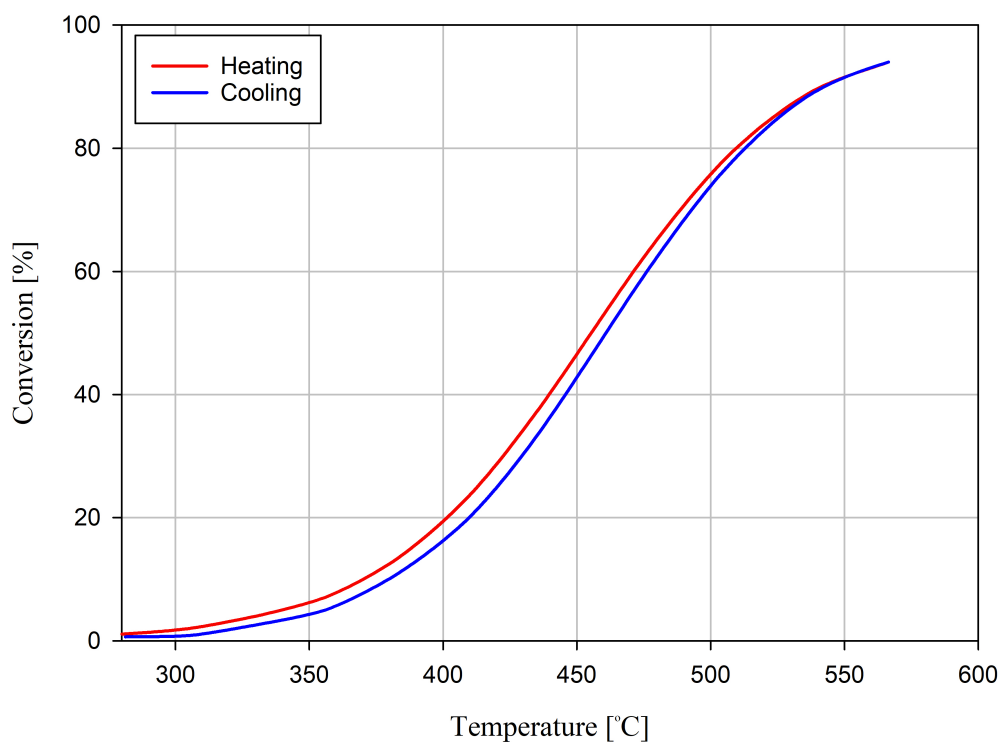
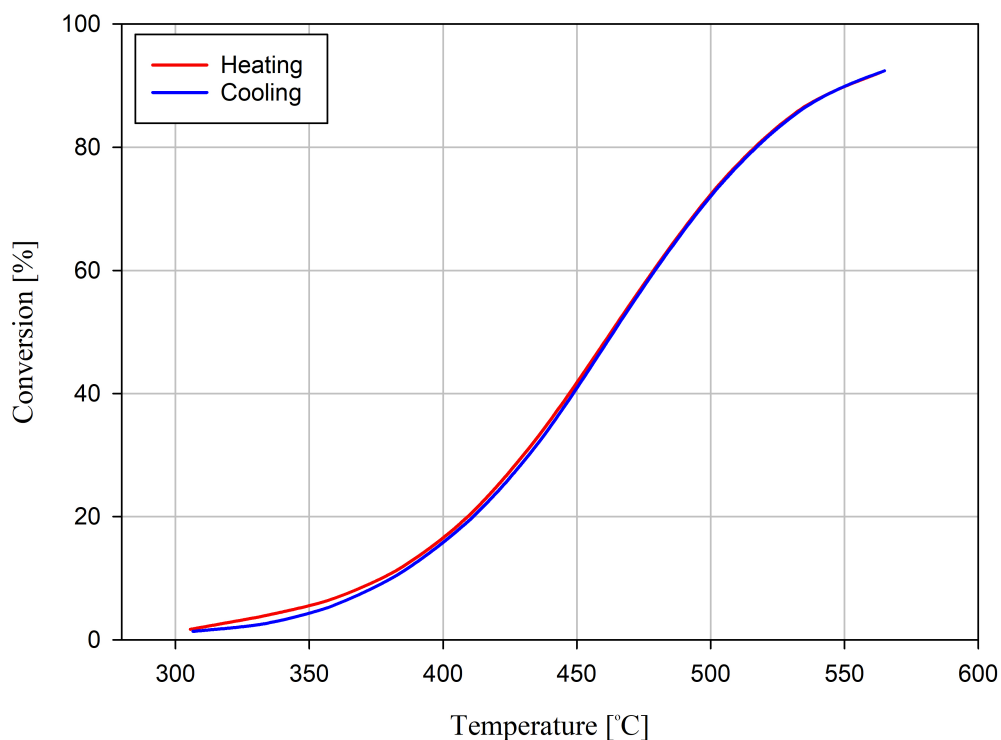


Figure 4.6.: Methane conversion curve of samples 6.3 NiCoO/CeO₂/L-S1 and 6.5NiCoO/CeO₂/L-S5. Reaction conditions: $F_{\text{CH}_4} = 4 \text{ ml min}^{-1}$, $F_{\text{N}_2} = 100 \text{ ml min}^{-1}$, $F_{\text{Air}} = 96 \text{ ml min}^{-1}$

The reaction curve for the catalyst 6.5NiCoO/CeO₂/H-S7, which was synthesized on high surface area CeO₂, is shown in Figure 4.7a. The figure represents the first reaction cycle of the catalyst, and it is noted that the cooling curve deviates somewhat from the heat curve through the reaction. The second reaction cycle of the catalyst, which can be seen in figure 4.7b, shows a more stable reaction path with smaller deviations between the heating curve and the cooling curve. This could indicate a more stable catalyst, but it should be noted that the reaction curve has shifted to slightly higher temperature compared to the reaction obtained from the first cycle.



(a) First reaction cycle of the catalyst 6.5NiCoO/CeO₂/H-S7. Reaction conditions: $F_{\text{CH}_4} = 4 \text{ ml min}^{-1}$, $F_{\text{N}_2} = 100 \text{ ml min}^{-1}$, $F_{\text{Air}} = 96 \text{ ml min}^{-1}$, amount of sample = 0.5025 g, proportion of active material = 0.039 g, $P = 1 \text{ bar}$.



(b) Second reaction cycle of the catalyst 6.5NiCoO/CeO₂/H-S7. Reaction conditions: $F_{\text{H}_2} = 4 \text{ ml min}^{-1}$, $F_{\text{N}_2} = 100 \text{ ml min}^{-1}$, $F_{\text{Air}} = 96 \text{ ml min}^{-1}$, amount of sample = 0.5025 g, proportion of active material = 0.039 g, $P = 1 \text{ bar}$.

The reaction rate calculated, which were performed with equation 2.21, at $T = 400\text{ }^{\circ}\text{C}$ and $T = 450\text{ }^{\circ}\text{C}$ for pure NiCo_2O_4 , which was calculated during the specialization project, and NiCo_2O_4 catalysts on low- and high surface area CeO_2 is presented in table 4.5. In addition, a calculation example can be seen in appendix C, and a blank test of the support material can be reviewed in table C.1, appendix C.4, where the result shows small signs of CH_4 conversion.

Furthermore, the reaction rates in table 2.21 shows small variations in between the catalysts. It is noted that there is no significant difference between the reaction rate of NiCo_2O_4 on low surface area, CeO_2/L , and high surface area, CeO_2/H .

Table 4.5.: Reaction rate calculated at $T = 400$ and $450\text{ }^{\circ}\text{C}$, for catalysts supported on high-and low surface area CeO_2 and NiCo_2O_4 .

ID	$T[^{\circ}\text{C}]$	X_{CH_4}	$r [\text{mol g}_{\text{act}} \cdot \text{cat}^{-1} \text{h}^{-1}]10^{-2}$	$T[^{\circ}\text{C}]$	X_{CH_4}	$r [\text{mol g}_{\text{act}} \cdot \text{cat}^{-1} \text{h}^{-1}]10^{-1}$
NiCo_2O_4	400	0.32	0.7	450	0.65	0.1
6.3NiCoO/ CeO_2/L -S1	400	0.17	5.7	450	0.39	1.3
6.0NiCoO/ CeO_2/L -S3	400	0.15	5.2	450	0.34	1.2
5.6NiCoO/ CeO_2/L -S4	400	0.15	5.7	450	0.36	1.4
6.5NiCoO/ CeO_2/L -S5	400	0.19	6.1	450	0.39	1.3
6.6NiCoO/ CeO_2/L -S6	400	0.16	5.2	450	0.36	1.2
6.5NiCoO/ CeO_2/H -S7	400	0.20	6.5	450	0.45	1.5
6.5NiCoO/ CeO_2/H -S7*	400	0.16	5.4	450	0.42	1.4
* 2 nd run						

4.6.1. Effect of H₂O

Figure 4.8 contains a comparison of several reaction cycles performed during wet and dry reaction conditions for the same catalyst. The result shows that the effect of water in the feed decreases the activity of the catalyst compared to the reference reaction curve. In addition, the comparison shows that the dry cycles reaction path moves after each wet cycle, and this could indicate that the catalyst deactivates irreversibly.

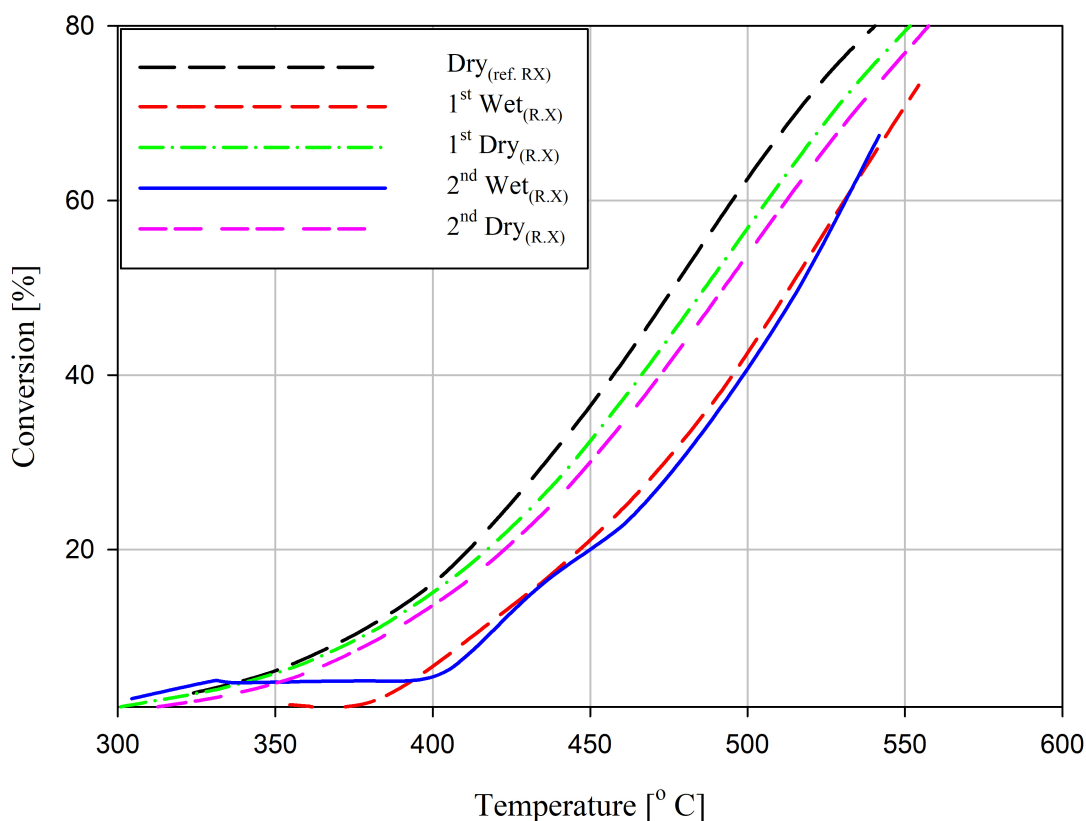


Figure 4.8.: Dry and wet reaction cycles of the catalyst 6.6NiCoO/CeO₂/L-S6. Reaction conditions: $F_{\text{CH}_4} = 4 \text{ ml min}^{-1}$, $F_{\text{N}_2} = 80 \text{ ml min}^{-1}$, $F_{\text{Air}} = 96 \text{ ml min}^{-1}$, $F_{\text{H}_2\text{O}} = 20 \text{ ml min}^{-1}$, amount of sample = 0.5036 g, proportion of active material = 0.033 g, $p = 1 \text{ bar}$. Reaction conditions Dry: $F_{\text{CH}_4} = 4 \text{ ml min}^{-1}$, $F_{\text{N}_2} = 100 \text{ ml min}^{-1}$, $F_{\text{Air}} = 96 \text{ ml min}^{-1}$, $P = 1 \text{ bar}$.

Figure 4.9 shows the reaction evolution of catalyst 6.6NiCoO/CeO₂/L-S6 in repeated dry and wet reactions, where the measurements are calculated for the conversion at T = 450 °C. The trend line indicates a declining trend through the experiments. In addition, table 4.6 contain the reaction rate calculated for each reaction cycle of the low surface area catalyst.

Table 4.6.: Reaction rate calculated for repeating wet and dry reaction cycles at 450 °C for catalyst 6.6NiCoO/CeO₂/L-S6.

Reaction cycle	T [°C]	X _{CH₄}	r [mol g _{act.cat} ⁻¹ h ⁻¹] 10 ⁻¹
Dry _(ref. R,X)	450	0.36	1.2
1 st Wet _(R,x)	450	0.20	0.7
1 st Dry _(R,x)	450	0.32	1.0
2 nd Wet _(R,X)	450	0.20	0.6
2 nd Dry _(R,X)	450	0.29	0.9

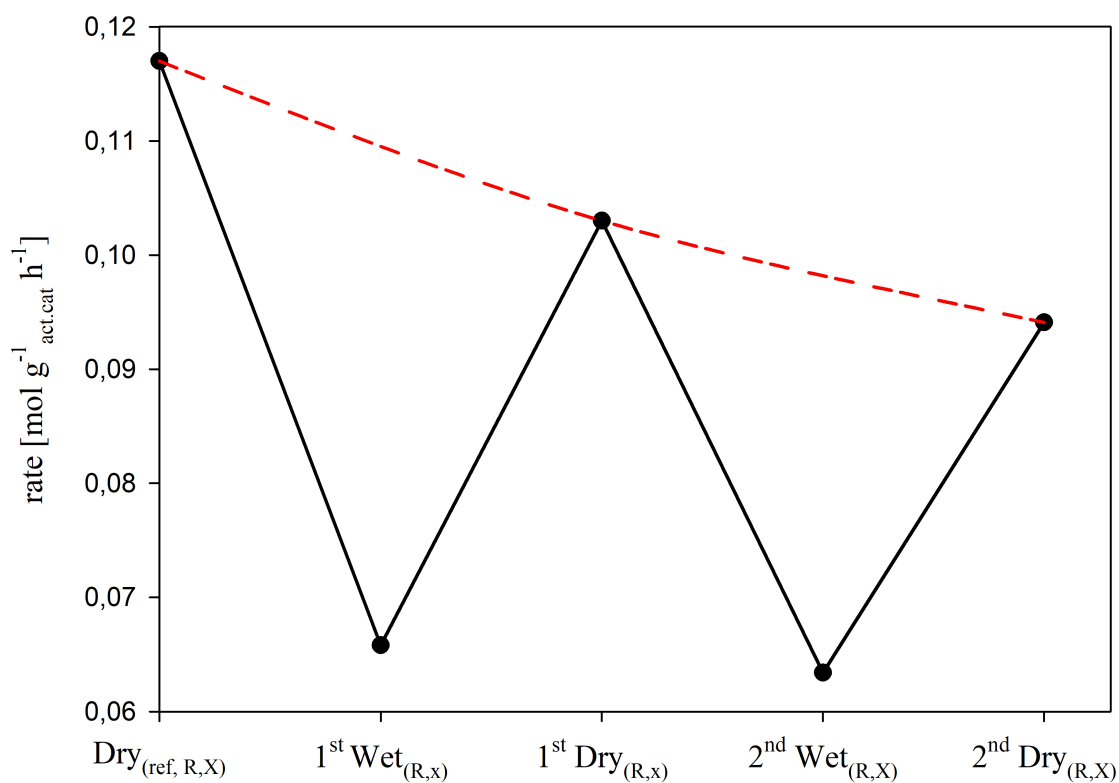


Figure 4.9.: Reaction rate, for sample 6.6NiCoO/CeO₂/L-S6, calculated at T = 450 for 2 cycles with H₂O and three without. Reaction conditions Wet: F_{CH₄} = 4 ml min⁻¹, F_{N₂} = 80 ml min⁻¹, F_{Air} = 96 ml min⁻¹, F_{H₂O} = 20 ml min⁻¹, amount of sample = 0.5036 g, proportion of active material = 0.033 g, p = 1 bar. Reaction conditions Dry: F_{CH₄} = 4 ml min⁻¹, F_{N₂} = 100 ml min⁻¹, F_{Air} = 96 ml min⁻¹, P = 1 bar.

In Figure 4.10, the conversion trend from the long-term trial of a catalyst synthesized on low surface area CeO_2 , is compared to the activity trend of pure NiCo_2O_4 . Additionally, the activity, which was calculated from the long-term trial, is quantified and compared in table 4.7. A calculation example can be viewed in appendix C.3. The Long-term trials of NiCo_2O_4 have previously been performed by SINTEF, and the results presented here is based on the results obtained from that experiment.

Table 4.7.: Comparison of activity of $6.6\text{NiCoO}/\text{CeO}_2/\text{L-S6}$ and NiCo_2O_4 SINTEF connected with time on stream (TOS).

$6.6\text{NiCoO}/\text{CeO}_2/\text{L-S6}$		NiCo_2O_4 SINTEF	
TOS [h]	r [$\text{mol g}_{\text{act} \cdot \text{cat}}^{-1} \text{h}^{-1}$] 10^{-2}	TOS [h]	r [$\text{mol g}_{\text{act} \cdot \text{cat}}^{-1} \text{h}^{-1}$] 10^{-4}
10	3.5	10	1.6
30	3.6	30	1.6
50	3.5	50	1.5
70	3.0	70	1.5

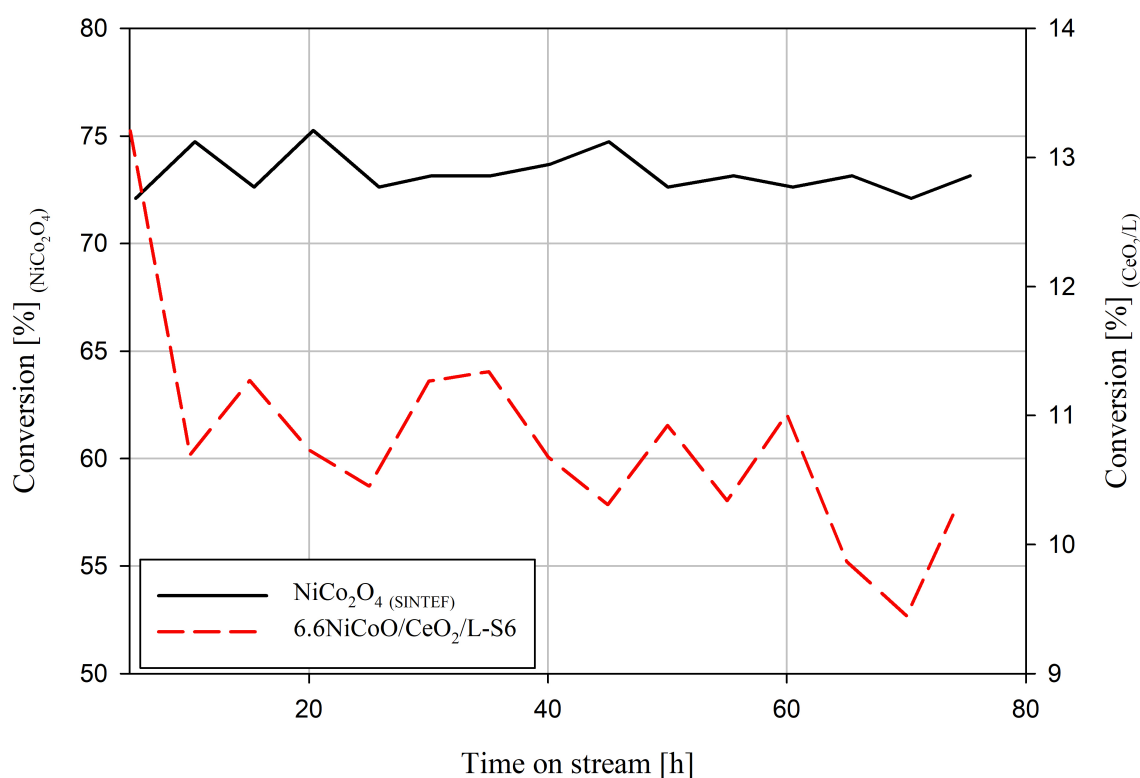


Figure 4.10.: Comparison of the conversion trend between $6.6\text{NiCoO}/\text{CeO}_2/\text{L-S6}$ and pure NiCo_2O_4 , under wet reaction conditions.

Quantified bulk activity pr. m^2 for catalysts based on high and low surface area CeO_2 is compared in table 4.8. The result shows that the activity is higher for low surface area CeO_2/L relative to CeO_2/H . This may further indicate that CeO_2/L based catalysts utilize the area better compared to NiCo_2O_4 synthesized on CeO_2/H . In the figure 4.11, the reaction trend of NiCo oxide on high and low surface area CeO_2 is compared. The figure shows that the activity of the catalyst supported by high surface area CeO_2 increases over time compared to NiCo oxide on CeO_2/L . A calculation example for the bulk activity is shown in appendix C.3.

Table 4.8.: Comparison of bulk activity pr. m^2 of $6.6\text{NiCoO}/\text{CeO}_2/\text{L-S6}$ and $6.5\text{NiCoO}/\text{CeO}_2/\text{H-S7}$.

6.6NiCoO/CeO ₂ /L-S6		6.5NiCoO/CeO ₂ /H-S7	
TOS [h]	r_B [mol m ⁻² h ⁻¹] 10 ⁻⁴	TOS [h]	r_B [mol m ⁻² h ⁻¹] 10 ⁻⁵
10	3.9	10	2.1
30	4.1	30	2.1
50	4.0	50	2.1
70	3.4	70	2.1

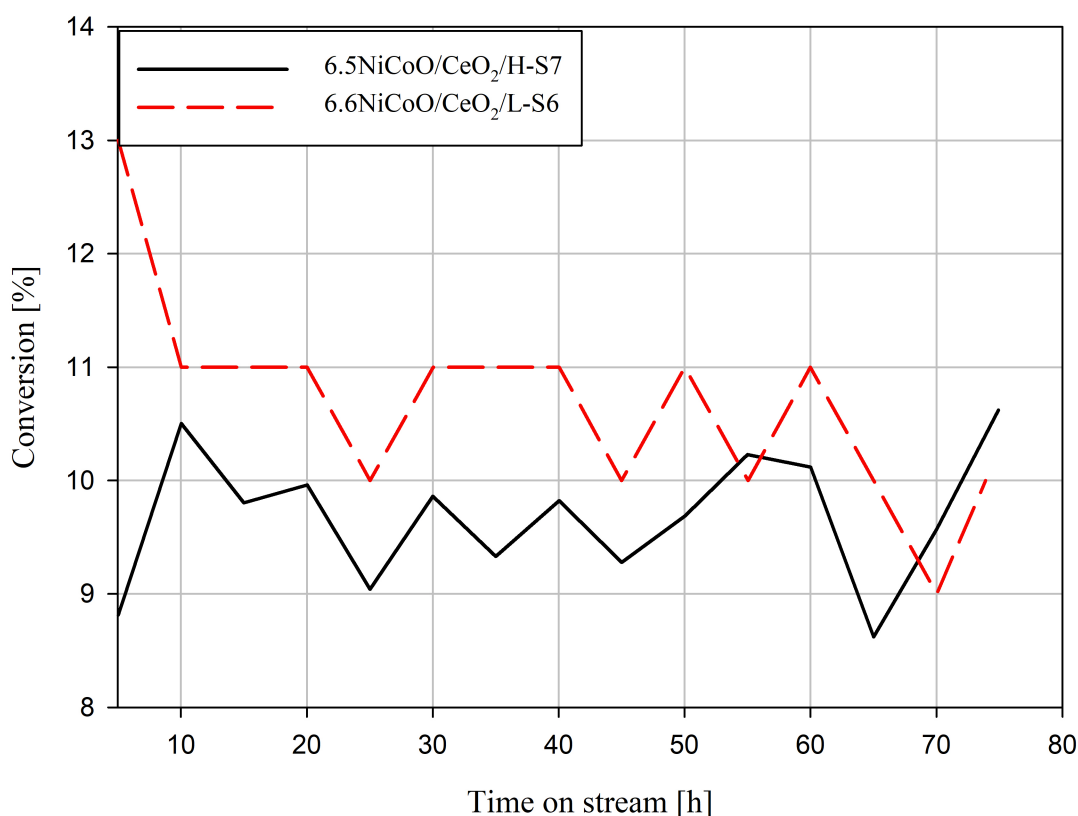


Figure 4.11.: Comparison of activity trend to NiCo_2O_4 supported by high and low surface area CeO_2 , under wet reaction conditions.

Carbon Error

A carbon plot of the 6.5NiCoO/CeO₂/L-S5 catalyst is shown in Figure 4.12. With increasing methane conversion, the error decreases linearly by a few divergent points. This may indicate that compounds other than CO₂ are formed during the reaction, or that the measuring instrument should be calibrated. Calculation of carbon errors was performed using equation 2.19.

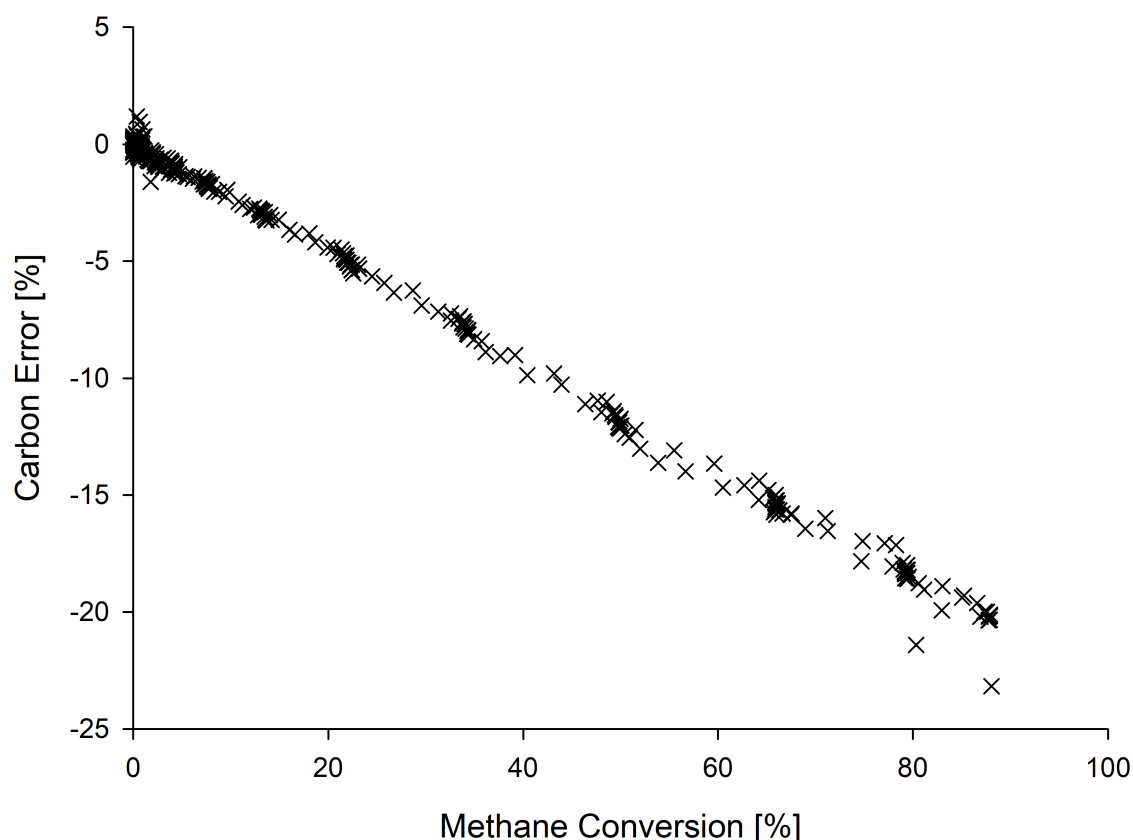


Figure 4.12.: Carbon error plot of sample 6.5NiCoO/CeO₂/L-S5. Reaction conditions: $F_{\text{CH}_4} = 4 \text{ ml min}^{-1}$, $F_{\text{N}_2} = 100 \text{ ml min}^{-1}$, $F_{\text{Air}} = 96 \text{ ml min}^{-1}$, amount of sample = 0.5012 g, proportion of active material = 0.035 g, $P = 1 \text{ bar}$.

In Figure 4.13 the carbon error for sample 6.5NiCoO/CeO₂/H-S7 is plotted against methane conversion. The plot illustrates the same structure with a descending linear line as shown in Figure 4.12. The same trend is observed in all the samples that were synthesized, and the results can be viewed in appendix C.2.

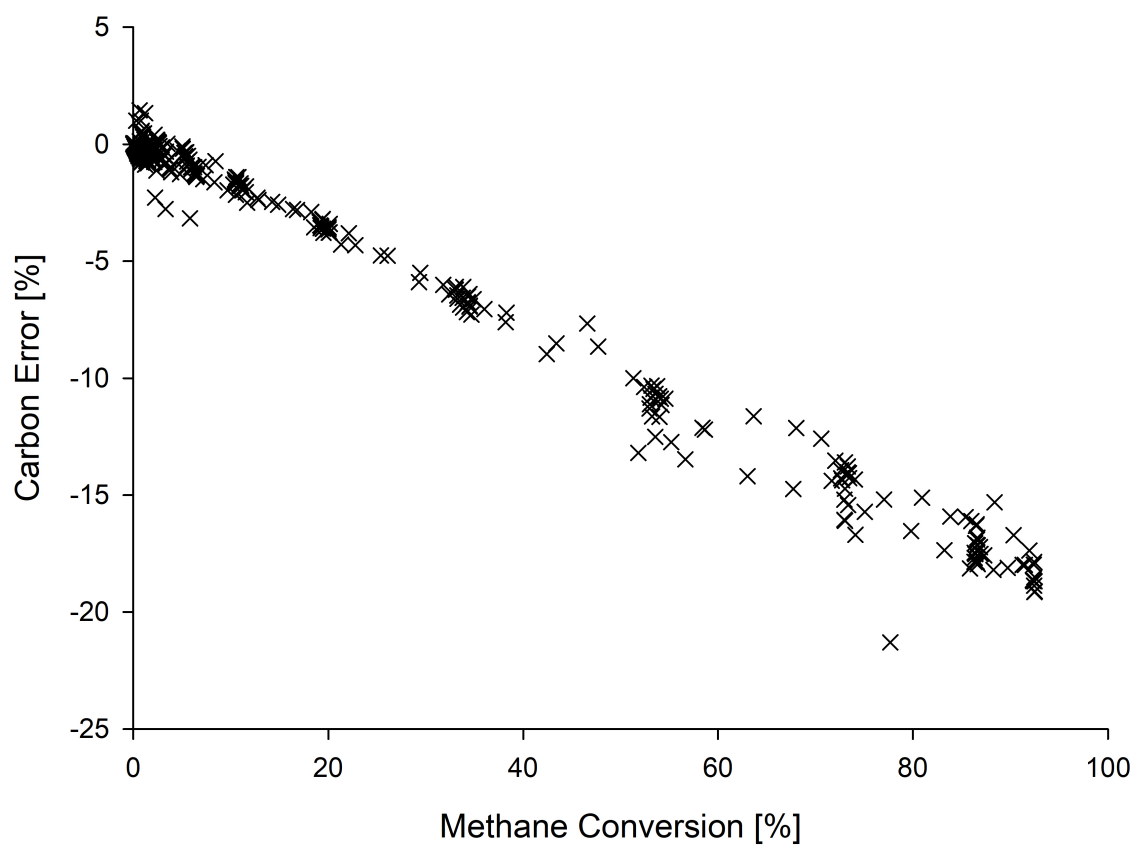


Figure 4.13.: Carbon error plot of sample 6.5NiCoO/CeO₂/H-S7. Reaction conditions: $F_{\text{CH}_4} = 4 \text{ ml min}^{-1}$, $F_{\text{N}_2} = 100 \text{ ml min}^{-1}$, $F_{\text{Air}} = 96 \text{ ml min}^{-1}$, amount of sample = 0.5025 g, proportion of active material = 0.039 g, $P = 1 \text{ bar}$.

4.7. Raman - Carbon Deposition Studies

For further investigation on the suspicion of carbon deposition on the catalysts, Raman and TGA were used. The result of Raman can be seen in figure 4.14, the plot shows the measurement range 1200 - 2000 cm^{-1} , where it is most appropriate to search for carbon, for the materials SiC, CeO_2 , and used and unused 6.5NiCoO/ CeO_2 /L-S5 catalysts. Three prominent peaks typical of SiC are highlighted in the figure. It should be noted that these peaks can only be observed in used sample material, and there are no peaks indicating the presence of carbon.

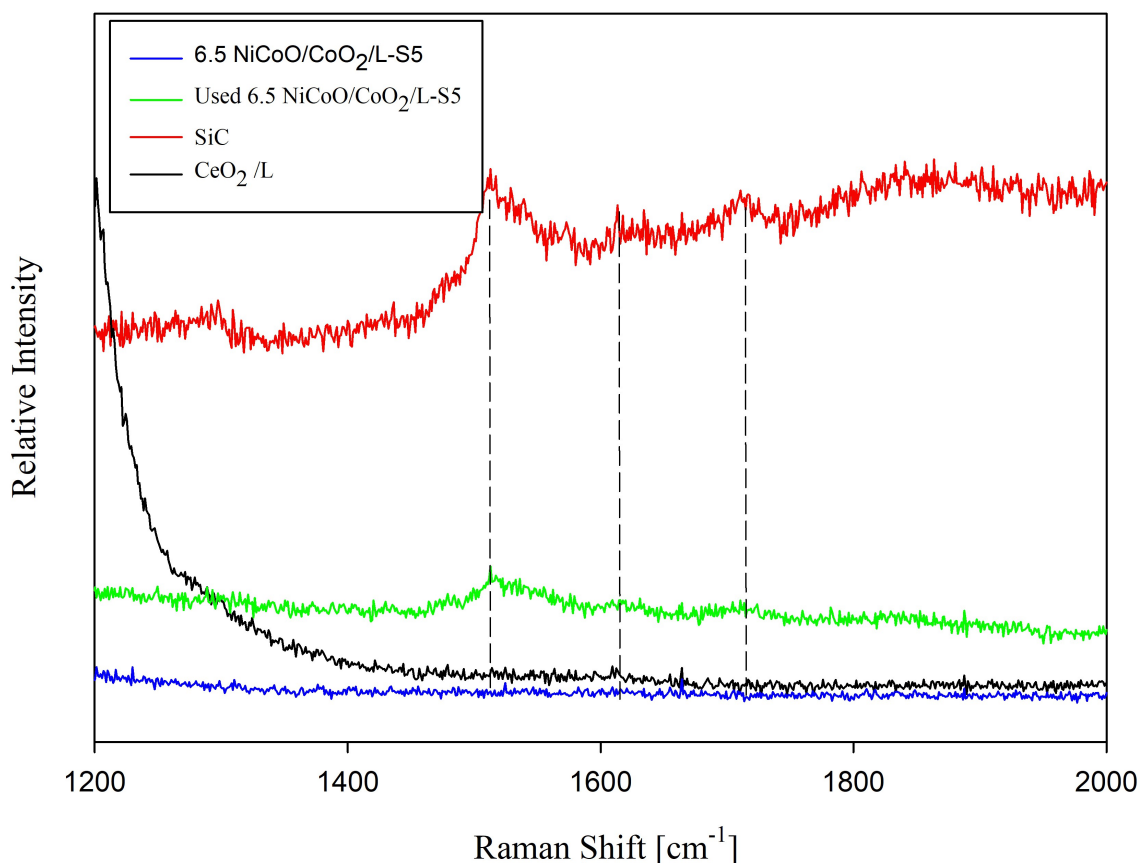


Figure 4.14.: Raman plot of materials SiC, CeO_2 , used and unused 6.5NiCoO/ CeO_2 /L-S5 catalyst. Analysis parameters: Range = 100 - 3000 cm^{-1} , Accumulation = 4, Acc. Time = 4 min, Filter = 10 %, Hole = 200.

5. Discussion

In this section, synthesis of the catalysts as well as CeO₂/H will be discussed. In addition, structural differences and properties that have been examined with different characterization techniques will be reviewed.

The accuracy of the methods used was tested by repeating selected samples several times. More about the conduction and calculations performed in accordance with the accuracy tests are shown in Appendix A.

5.1. Synthesis of Catalysts and Support

As mentioned in section 3.1, the catalyst synthesis was performed using the IWI method, which is established on pore volume measurements [28]. Considering the morphology examination of CeO₂/L performed during the specialization project, the decision of the IWI method was not recommended because CeO₂/L has no defined pore volume. [12]. However, because the samples were intended as a reproduction of the results of that experiment, the decision to continue was based on further comparison. Further synthesis was therefore performed with multiple impregnation rounds, where the samples were dried in-between.

As a consequence, multiple impregnations can create an error source which is of concern regarding material loss. This loss may result from some of the material remaining in the pipette tip and, as a result, will not be transferred to the sample. Further, the nitrates used to prepare the solution, were very static and this created some challenges when weighing and transferring materials between different containers. The solution to the problem was to minimize the number of transfers and the use of containers. However, it must be assumed that some material may have been lost even when certain precautions were taken.

Synthesis of high surface area CeO₂/H was performed with a Sol-gel method that was primarily based on the molar ratio of Ce(NO₃)₃ and NaOH as well as the ratio of NaOH and distilled H₂O [30]. The advantage of this was the synthesis could be performed in a very short time, and without use of inorganic/organic templates as well as solutions. The whole procedure took only 2.5 h, and it was capable of producing CeO₂ with high surface area and defined pore structure as shown in table 4.2. The main concern with this method is uncontrolled product formation, and small variations between the mixing ratios will consequently give CeO₂ with different properties. The reaction conditions could have been monitored in terms of optimize the procedure. However, because it was capable of producing CeO₂ with the qualities that were desired, it was not considered necessary. Compared to CeO₂/L, the Sol-based method was capable to produce ceria with 25-times higher surface area, making it suitable for

IWI.

The XRF analysis composition data, which are shown in table 4.1, show that there is considerable variation between the nominal – and the measured weight percentage of NiCo active phase for all samples. The cause can further be explained by the analysis method, and the operating conditions the method needs for optimal performance.

Through the experiments, the limited factor for the analysis was the small amount of the samples that were used, approx. 100-150 mg which correspond to 6 – 10 mg of active material. The accuracy and the detection limit of the instrument is mainly founded on sample size, sample matrix, and the elemental weight, which is related to fluorescence emission [25]. Hence, for analysis of samples that contain heavy elements, the size -and the amount of sample can be smaller than for a sample that contains lighter elements, such as this case. Further, the SQX program that was used during the analysis is a non-standard program. The advantage of this is that the analysis can give quick answers to which elements the sample contains. But the downside is lower accuracy. The accuracy is also highly dependent on sample preparation and the sample homogeneity which are associated with NiCo oxide distribution. Based on this, it is assumed that some of these points, but especially the quantity and size of the sample, have negatively affected the accuracy of the XRF.

In relation to elemental analysis, atomic spectroscopy such as ICP-MS could have been an alternative to XRF. However, the sample must be dissolved in an acid solution, and in contrast to the destructive ICP-MS analysis, XRF is the best non-destructive alternative. Therefore, it was decided to use XRF further, but with some restrictions associated with the accuracy as discussed previously.

Even though the synthesis may cause deviations, and considering the XRF accuracy, further calculation of the reaction rates is therefore based on the nominal weight percentage.

5.2. High and Low Surface Area CeO₂ Support Structure

The Raman result as shown in figure 4.2 demonstrates how the support material poses some challenges associated with the characterization technique. Characteristic for the support is the large peak at 457 cm⁻¹ for CeO₂/L and 475 cm⁻¹ for CeO₂/H. However, this entails some challenges when it comes to investigation of active phases. The scattered intensity, caused by Reyleigh band, covers the Stokes band scattered from the surface components. Consequently, the substances of interest are hidden and therefore difficult to detect. The use of a stronger laser could have resolved the issue, however this may have changed the active phases [25].

In contrast to the strong signal of CeO₂/L, CeO₂/H has a lower intensity which is believed to be associated with structural differences. 10 % filter was used to compensate for some of the scattered light, and it had a positive effect according examination results. The plateau at 457 Cm⁻¹ for CeO₂/L is a result of maximum intensity, and it gives a clear picture that CeO₂ provides strong signals that interfere with the image.

The XRD result shown in table 4.3 show small differences in terms of crystallite size, but the variations observed can be a result of defects and stress in the material. Three comparable peaks were found, and they shows that the difference in crystallite size between high and low surface area CeO₂ lies between 56, 43 and 37 nm. The number of peaks observed during examination, and the morphology of the peaks, shown in figure 4.3, is also different between the two materials. Tall straight peaks are associated with larger crystals. This could suggest that CeO₂/H has a more disordered structure and smaller particles compared to CeO₂/L [34]. However, further investigation of particle size with TEM is necessary to confirm this assumption.

N₂-Physisorptions experiments were performed to investigate the difference in surface area and pore volume. The results for high-and low surface area CeO₂ can be seen in table 4.2 It should be noted that CeO₂/L has no defined pore volume that can be compared to CeO₂/H. The reason for this was investigated during the specialization project, where it was concluded that the material had the same structure as clay [12]. Figure 4.1 shows a distribution chart over pore width found in CeO₂/H, and with an average of 12.065 nm this implies a more porous structure. Further comparison of the S_{BET} in table 4.2 shows that synthesised CeO₂ area increases with 149.48 m²g⁻¹. Hence, the results show that CeO₂/H has a more porous structure with a more defined pore system as well as smaller particles. Furthermore, the results show that it was possible to produce a support with the desired properties for further comparison.

5.3. NiCo₂O₄ Catalyst Structure

Raman spectroscopy was used to study the NiCo₂O₄ spinel on the synthesised samples. In figure 2.9 only 6.5NiCoO/CeO₂/L-S5 and 6.5NiCoO/CeO₂/H-S7 are plotted respectively with the support, but the result from all synthesised samples can be viewed in appendix B.2 figure B.2-B.3. The Raman

shifts at 188, 192, 644 and 660 cm⁻¹ correspond to the vibrations associated with the spinel structure NiCo₂O₄ [15][16]. However, since there is a similarity between the NiCo₂O₄ and the spinel Co₃O₄, the result cannot rule out the presence of the other structure. The samples were examined in the range of 100 – 1000 cm⁻¹ and with 10 % filter. Mainly, the investigation boarder was based on historical data that had identified the structure in this range before [15]. The 10 % filter was applied during the experiment due to the scattered light from the support material as previously mention. Nevertheless, the samples did contain small amounts of active material which could have had a negative influence on the analysis due to the method focuses on a limited area of the sample. Although, the consequence for some areas of the sample would be smaller amounts of particles that can contribute to scattering Stokes band and generate a stronger signal.

The XRD spectrum of the catalyst 6.5NiCoO/CeO₂/L-S5 and the fresh-and used specimen of 6.5NiCoO/CeO₂/H-S7 is presented in figure 4.4, in which the crosses indicate the 2θ values for the diffraction peaks of NiCo₂O₄ spinel. Nevertheless, some precaution must be taken into consideration regarding the NiCo₂O₄ spinel. There exists similarities between the NiCo₂O₄ and the Co₂O₃ spinel that can make them difficult to separate. Hence, the Co₂O₃ present cannot be neglected. Though, if Co₂O₃ exists there will be a separate phase for nickel that has not been detected. Consequently, the presence of Ni and Co₂O₃ cannot be confirmed or rejected due to the limitations of the method [25].

Generally, the spectrum in figure 4.4 features morphological similarities regarding the support peaks as previously discussed. But some differences do exist, especially narrower and taller peaks that illustrates crystallite growth due to interaction between NiCo₂O₄ and CeO₂. Table 4.4 contains calculated crystallite size in the 2θ range 15-75 °for the stated samples. Though, four comparative peaks for the crystallite phase of CeO₂ are found at 2θ = 28, 33, 47, 56 and 69 °. Moreover, the size difference indicates that 6.5 NiCoO/CeO₂/L-S5 particles consists of larger crystallites. Nevertheless, small and amorphous structures can't be detected due to the methods limitations, and a more complete morphology study of the samples would require another method such as TEM [25].

Moreover, it was not possible to separate pure NiCo₂O₄ phases from the support structure, regardless of morphological difference as shown in figure 4.4. This may suggest an amorphous spinel structure with high dispersion on the support material. In addition, this may imply that CeO₂ binds NiCo oxides in a manner that results in high disperses regardless of the support structure. However, this must be further explored with other characterisation techniques due to XRD limitations as previously mentioned.

The examination result in figure 4.5 compares the reduction curve of 6.5NiCoO/CeO₂/L-S5 and 6.5NiCoO/CeO₂/H-S7 from the TPR analysis. Although the reaction conditions were virtually the same, some difference in mass of active material must be taken in consideration when analysing the results. The reduction of the catalyst 6.5NiCoO/CeO₂/H-S7 is initiated at a lower temperature, approx. 200 °C, compared to the catalyst on low surface area CeO₂. However, the catalyst is not reduced

completely before 725 °C. On the other hand, reduction of 6.5NiCoO/CeO₂/L-S5 are initiated at 270 °C and completed at 650 °C. Considering the difference in active material load, the difference could be a result of a greater H₂ access in favour of 6.5NiCoO/CeO₂/L-S5. However, the reduction range could also be caused by transport limitation of lattice oxygen in the catalyst due to the shrinking core phenomena [34]. Moreover, from the TPR profile for CeO₂/L and CeO₂/H, appendix B.4 figure B.7, the surface area appears to have an effect on the reducibility of ceria. However, this difference becomes smaller with NiCo₂O₄ on, which may indicate that the NiCo oxides promotes the reduction of ceria. It is not easy to make both effects fit together unless the spinel does not modify both high and low surface area CeO₂ in the synthesis.

5.4. Catalyst Activity

In the following section the activity of NiCo₂O₄ catalyst supported by two different types of CeO₂ will be discussed. However, some limitation regarding polynomial fitting of the reaction curve must be taken in consideration. Hence, the accuracy of the reaction rate calculated at T = 400 and T = 450 °C may differ slightly. Moreover, calculation of the reaction rate is based on the assumption of first order reaction regarding CH₄, and zero order for oxygen. It should also be noted that the carbon error shows a linear decrease, which indicate loss of carbon, throughout all of the samples. The validity of the results was confirmed by repeating the tests several times.

5.4.1. Effect of CeO₂

The figure 4.6, where the conversion achieved for sample 6.5NiCoO/CeO₂/L-S5 is plotted against temperature, shows that the catalyst is capable to convert over 80 % of the methane at a temperature of 550 °C. In contrast to previous research where pure NiCo₂O₄ spinel has been proven to achieve 90 % conversion at 479 °C and full conversion at a temperature of 550 °C , the nominal value of the synthesized sample is only 6.5 wt % of NiCo mixed oxide [15]. Moreover, the reaction rate of pure NiCo₂O₄ is compared to the reaction rate pr. gram active material of the synthesized catalysts in table 4.5. The activity is higher for all catalysts supported by CeO₂ regardless of nominal oxide composition compared to pure spinel. Furthermore, this shows that CeO₂ has a very positive effect in terms of activity, regardless of the support morphology. This may indicate that there is some form of association between NiCo₂O₄ and CeO₂ that facilitates CH₄ conversion in favour of the low nominal value. However, this may also be a result of the elevated oxygen transfer capacity of CeO₂ [27].

Considering the environment in terms of production and needs of raw materials, these properties could be advantageous, especially when it comes to production of Co which is best known as a by-product from Cu- and Ni ores. This also applies where extensive processing and energy consumption is necessary to achieve high purity. In addition, spinel supported on CeO₂ show greater temperature stability over samples based on γ -Al₂O₃ [16].

5.4.2. Reproduction of The Specialization Project Result and Effect of Low Surface Area CeO₂

The results from the reproduction experiment of the catalyst synthesized during the specialization project is shown in table 4.5. The reaction rate of Sample 6.5 NiCoO/CeO₂/L-S5 and sample 6.3 NiCo/CeO₂/L-S1 calculated at T = 400 °C shows that the difference between these two are $3.9 \cdot 10^{-3} \text{ mol g}_{\text{act} \cdot \text{cat}}^{-1} \text{ h}^{-1}$. Likewise, the difference at T = 450 °C is $6.6 \cdot 10^{-3} \text{ mol g}_{\text{act} \cdot \text{cat}}^{-1} \text{ h}^{-1}$. Comparison of the reaction curve as seen in figure 4.6 indicates that the reaction follows the same temperature path with corresponding CH₄ conversion for both samples. Consequently, sample 6.5 NiCoO/CeO₂/L-S5 is the one closest to reproduce the result from the specialization project [12].

In addition, the reaction profile for all the other samples can be seen in figure C.1-C.4 in appendix C. The same reaction pattern is recognised for all the synthesized samples. But, small variations in composition of Ni and Co seems to be responsible for the activity difference between 6.5NiCoO/CeO₂/L-S5 and 6.3NiCo/CeO₂/L-S1 as seen in table 4.5. Even though the composition is different for the synthesized catalysts, the stability of the catalysts is conserved and there are no signs of deactivation when comparing the hot-and cold conversion curve. This could indicate that ceria is in its most stable form as previously mentioned, and that it binds strongly to the active material and prevents sintering during reaction [27].

5.4.3. Effect of High Surface Area CeO₂

Considering figure 4.7a which contains the first conversion curve of sample 6.5 NiCoO/CeO₂/H-S7, show sign of deactivation. Further, investigation of the deactivation mechanisms was performed with N₂-physisorption and XRD. The results of these studies are shown in table 4.2 and table 4.4. Comparison of the fresh and the used catalyst shows that S_{BET} decreases with $17.24 \text{ m}^2 \text{ g}^{-1}$, and crystallite size of CeO₂/H increases. The rate of the reaction is also decreasing as seen when the result obtained for the first and second, at T= 400 and T = 450 °C, reaction cycle is compared in table 4.5. Hence the conversion curve has moved to the right as shown in figure 4.7b. Consequently, it can be assumed that deactivation is a result of sintering.

Additionally, figure 4.7b contains the heating and cooling curve of the second reaction cycle of sample 6.5 NiCoO/CeO₂/H-S7, and it shows no sign of deactivation. The phenomenon where the catalyst is first deactivated and then not, is believed to be associated with the synthesis technique or the calcination, which were performed at a maximum temperature of 550 °C. The assumption is based on previous observations during the specialization project, but also observations made by others, including H. Schulster [16][12].

Further, the catalyst had a maximum conversion at approx. 90 % at T = 550 °C when it was stabilized, and even higher for the unstable try. This is based on the characterization of the support materials and the catalysts as previously discussed, and by comparing the activity results with those obtained

for the samples containing CeO_2/L , table 4.5. It appears that the CeO_2/H support material results in slightly increased activity for the NiCo_2O_4 catalyst. Moreover, this also suggests that the difference between CeO_2/L and CeO_2/H does not significantly affect the activity.

For synthesizing of sample $6.5\text{NiCoO}/\text{CeO}_2/\text{H-S7}$ on CeO_2/H , it was decided that the sample that was able to reproduce the result of the specialization project should be used as a template. Hence, the nominal active material weight percentage for $6.5\text{NiCoO}/\text{CeO}_2/\text{H-S7}$ is the same as sample $6.5\text{NiCoO}/\text{CeO}_2/\text{L-S5}$. The decision was made with focus on further investigation and comparison of how NiCo_2O_4 was affected by the two different support structures. As discussed previously in this section, the NiCo_2O_4 on CeO_2/H is likely to have higher activity relative to $6.5\text{NiCoO}/\text{CeO}_2/\text{L-S5}$ and the other samples synthesized on CeO_2/L in terms of CH_4 conversion. Although the catalyst experienced some deactivation, for the stable version it is assumed that the same properties as discussed for the CeO_2/L samples regarding environmental benefits, association and oxygen transfer capacity also apply here.

5.4.4. Effect of Water

To obtain a more realistic picture of the catalysts capability to treat excess CH_4 from exhaust gas, the effect of water was investigated. In addition, multiple reaction cycles were performed with dry and wet reaction conditions to examine the deactivation mechanism of NiCo_2O_4 on high- and low surface area CeO_2 . Further, long-term experiments under wet reaction conditions were used to compare the stability of NiCo_2O_4 on low surface area CeO_2 and pure NiCo_2O_4 , which have previously been studied by SINTEF. Furthermore, the catalysts NiCo_2O_4 utilization of the surface area of CeO_2/L and CeO_2/H , were examined by comparing quantitative bulk activity pr. surface area CeO_2 .

Figure 4.8 contain the conversion curves of the catalyst $6.6\text{NiCoO}/\text{CeO}_2/\text{L-S6}$, where repeating cycles of dry and wet reaction conditions are compared. Furthermore, the catalyst performance during wet conditions are decreasing, which suggests irreversible deactivation. Although, the deactivation mechanism of pure NiCo_2O_4 spinel is claimed to be reversible [15], this could imply that the irreversible deactivation mechanism is caused by structural changes in the support material due to H_2O . Figure 4.9, where the reaction rate at $T = 450\text{ }^\circ\text{C}$ for the catalyst $6.6\text{NiCoO}/\text{CeO}_2/\text{L-S6}$ are plotted, the falling trend line of the dry reaction cycles further contributes to the argument about irreversible deactivation.

Furthermore, the activity of the catalyst does not appear to be affected to the same extent as in pure spinel [15]. Considering that the synthesized catalysts contain a fraction of active matter relative to the catalysts that have been studied previously. And where the reversible deactivation is claimed to be caused by H_2O blocking active sites on the surface by adsorption. This could indicate that CeO_2 promotes oxidation of CH_4 due to the elevated O_2 capacity [27].

As mentioned initially, the long-term experiment, performed under wet reaction conditions, for a catalysts based on CeO_2/L , were used to compare stability and activity in relation with NiCo_2O_4 . The

examination result is shown in figure 4.10, where conversion is plotted vs time on stream. Further, the initial stability of the catalyst based on CeO_2/L show sign of deactivation relatively to NiCo_2O_4 . It is suggested that this could be a result of sintering, but it can also be related to the time on stream. In difference to 6.6NiCoO/ CeO_2/L -S6, which went through multiple dry and wet reaction cycles before the long-term examination, the NiCo_2O_4 spinel were examined from an unused specimen. Consequently, this is not optimal in terms of comparable reaction conditions, but it can be used to give an indication about the differences. Moreover, the low surface area CeO_2 based catalyst have higher activity pr. gram active NiCo oxide, which can be seen in table 4.7. Nevertheless, the dry reaction activity, which can be viewed in table 4.5, indicates the same behaviour between CeO_2 based catalysts and pure spinel as showed for wet reaction. Therefore, it is suggested that CeO_2 facilitates the reaction conditions for NiCo oxides in terms of CH_4 conversion better than pure spinel due to elevated oxygen transfer capacity of CeO_2 .

Further, the quantitative bulk activity of NiCo_2O_4 supported on high- and low surface area CeO_2 were examined through the long-term experiments obtained from two of the catalysts. As discussed previously, the activity of the catalyst supported on high surface area CeO_2 is likely to be higher than for NiCo_2O_4 on low surface area during dry reaction conditions. The opposite can be suggested regarding utilization of the available surface area. The result, which can be viewed in table 4.8 and figure 4.11, indicates superior surface utilization in favour of the low surface catalyst. Moreover, this could indicate that the catalyst has comparable distribution of NiCo oxide on the surface due to the IWI synthesis method. Likewise, the exploitation of available surface area could suggest that this method is not optimal in terms of surface scattering of NiCo_2O_4 on high surface area CeO_2/H . And that another method could have resulted in higher activity for the high surface area catalyst. Nevertheless, as previously discussed this may also be a result of CeO_2 distributing NiCo oxide equally, regardless of the support structure. And that it further reinforces the suspicion of an unknown interaction between CeO_2 and NiCo_2O_4 that has not yet been studied.

5.4.5. Carbon Deposits

As a result of the calculation of carbon error, where the results showed a continuous falling linear trend as seen in figure 4.12-4.13, the catalyst 6.5NiCoO/ CeO_2/L -S5 was selected for a carbon deposits survey. The first examination was performed with Raman in the range of $1200 - 2000 \text{ cm}^{-1}$ where any carbon deposits will be detectable. The result can be seen in figure 4.14. However, the result showed no traces of carbon when the Raman scatter of a fresh sample was compared to the support, SiC, and the used sample. Since Raman spectroscopy only focuses on a small part of the sample, the result could not debunk any carbon deposits. Therefore, further investigation with TGA was performed to confirm the result. Further, the TGA examination showed no signs of CO or CO_2 . Therefore, the result confirmed the Raman investigation. However, since the carbon error shows signs of missing carbon, the fault must lie somewhere else. It is conceivable that the error lies in the calibration of CO_2 , and that the GC should be re-calibrated.

6. Conclusion

In this master thesis the catalytic activity of catalysts comprised of nickel and cobalt mixed oxides supported by two different types of ceria have been investigated in terms of oxidation of methane at ambient pressure and low temperatures. The motivation behind the project was the opportunity to contribute with new information that can further be used to develop an effective exhaust gas treatment system for LNG driven vessels.

From the specialization project, catalysts containing a relatively small amount of active material supported on CeO_2/L showed positive signs of temperature stability and activity. Further, the results generated in the specialization project were reproduced to confirm the positive contribution that CeO_2 provided. Based on the results obtained for the test $6.5\text{NiCoO}/\text{CeO}_2/\text{L-S5}$, it can be concluded that the results obtained in the specialization project are correct, and that the activity of NiCo_2O_4 increases significantly when supported on CeO_2 .

Furthermore, catalysts supported on CeO_2 with different morphological properties were compared to see if the activity of the catalyst could be improved. The characteristic studies of catalyst $6.5\text{NiCoO}/\text{CeO}_2/\text{H-S7}$ showed that it was supported by CeO_2 which had a small crystalline size as well as a more defined pore system. Based on this, it was suggested that the support material consisted of smaller particles with a more amorphous structure, but this cannot be confirmed without further investigation with TEM. Comparison of activity results between $6.5\text{NiCoO}/\text{CeO}_2/\text{L-S5}$ and $6.5\text{NiCoO}/\text{CeO}_2/\text{H-S7}$ showed some increased activity in favour of $6.5\text{NiCoO}/\text{CeO}_2/\text{H-S7}$. In contrast, the catalyst showed signs of lower stability when some deactivation due to sintering was observed.

Examining the activity of the catalyst under wet reaction conditions and in a more realistic environment showed that H_2O led to irreversible deactivation. It is believed that the deactivation is caused by structural changes, but this must be further investigated before it can be confirmed. Moreover, comparison between low surface area catalyst and NiCo_2O_4 , showed higher activity pr. g NiCo_2O_4 in favour of the supported catalyst. Moreover, it is suggested that the higher activity is caused by the elevated O_2 transfer capacity of CeO_2 . In addition, the quantitative bulk activity analysis showed that NiCo_2O_4 based on low surface area CeO_2 utilized the support much better compared to NiCo_2O_4 synthesized on high surface area CeO_2 , since the activity was considerably higher pr. m^2 . This could further indicate that the IWI-impregnation method does not exploit available surface area for the benefit of NiCo_2O_4 , but it can also reinforce the suspicion of an unknown interaction between CeO_2 and NiCo_2O_4 that appears to lead to equal dispersion of NiCo_2O_4 on high and low surface area CeO_2 .

7. Further Work

During the project, it was discovered that $\text{NiCo}_2\text{O}_4/\text{CeO}_2$ based catalysts irreversibly deactivate under wet reaction conditions. Further, it would be appropriate to study the effect of different feed compositions of H_2O and CH_4 , and examine the change in activity to better understand the reaction mechanism of CeO_2 based catalysts. In addition, it will be of great importance to explore the NiCo distribution on CeO_2 more closely to follow up on the proposal of the unknown binding mechanism, which appears to lead to equal dispersion of NiCo_2O_4 on high and low surface area CeO_2 .

It will also be appropriate to perform a comparison of catalysts that contain different composition, and then conduct dry and wet activity experiments to see if a possible higher proportion of NiCo_2O_4 will result in lower deactivation, or not. Moreover, the long-term experiment with NiCo_2O_4 on low surface area CeO_2 should continue. This will provide a more reliable picture of the deactivation rate, which can contribute to a better comparison of the differences between supported-and unsupported NiCo_2O_4 .

Bibliography

- [1] *Climate Change: Global Temperature*. URL: <https://www.climate.gov/news-features/understanding-climate/climate-change-global-temperature> (visited on 03/13/2020).
- [2] *The Paris Agreement*. URL: <https://unfccc.int/process-and-meetings/the-paris-agreement/the-paris-agreement> (visited on 03/13/2020).
- [3] *Greenhouse Gas Emissions*. URL: <http://www.imo.org/en/OurWork/Environment/PollutionPrevention/AirPollution/Pages/GHG-Emissions.aspx> (visited on 03/13/2020).
- [4] *Klimagassutslipp fra transport*. URL: <https://miljostatus.miljodirektoratet.no/tema/klima/norske-utslipp-av-klimagasser/klimagassutslipp-fra-transport/> (visited on 03/13/2020).
- [5] *Utslipp til luft*. URL: <https://www.ssb.no/klimagassn> (visited on 03/13/2020).
- [6] “REDUKSJON AV KLIMAGASSUTSLIPP FRA NORSK INNENRIKS SKIPSFART”. In: (2016). URL: <https://www.regjeringen.no/contentassets/b3df5ceb865e42b48befdf132a95a8be/skipfsart-klimagasser-dnvg1.pdf>.
- [7] “Advances in clean hydrocarbon fuel processing; science and technology.” eng. In: *Reference and Research Book News* 26.6 (2011). ISSN: 08873763. URL: <http://search.proquest.com/docview/906484398/>.
- [8] *Contemporary environmental issues and challenges in era of climate change*. eng. Singapore, 2020.
- [9] M. Anderson, K. Salo, and E. Fridell. “Particle- and Gaseous Emissions from an LNG Powered Ship”. eng. In: *Environmental science and technology* 49.20 (2015), p. 12568. ISSN: 0013936X.
- [10] *Benefits of LNG*. URL: <https://www.primalng.com/about-lng/benefits-of-lng> (visited on 03/13/2020).
- [11] S. Ushakov, D. Stenersen, and P. Einang. “Methane slip from gas fuelled ships: a comprehensive summary based on measurement data”. eng. In: *Journal of Marine Science and Technology* 24.4 (2019), pp. 1308–1325. ISSN: 09484280. URL: <http://search.proquest.com/docview/2316455864/>.
- [12] J. A. Selnes. *TKP 4580-Methane Abatement for Natural Gas Engines*. eng. 2019.
- [13] H. M. Storrvik. *Catalysis for control of methane slip in marine machinery - Using platinum-based catalysts*. eng. 2016. URL: <http://hdl.handle.net/11250/2412888>.
- [14] H. M. Sandvik. *Catalysis for Control of Methane Slip in Marine Machinery - Using a Palladium based Catalyst*. eng. 2016. URL: <http://hdl.handle.net/11250/2412885>.
- [15] R. B. Lund-Johansen. “Nickel Cobalt Catalyst for Methane Abatement in Marine Machinery”. In: (2017).
- [16] H. Schuster. *Catalytic Methane Abatement for Natural Gas Engines*. 2019.

- [17] M. S. ; M. J. Y. ; V. J. V. ; W. D. A. *Handbook of Liquefied Natural Gas*. eng. Elsevier Science, 2013. ISBN: 0124045855.
- [18] *IMO Marine Engine Regulations*. URL: <https://dieselnet.com/standards/inter/imo.php> (visited on 02/27/2020).
- [19] P. Gélin and M. Primet. “Complete oxidation of methane at low temperature over noble metal based catalysts: a review”. eng. In: *Applied Catalysis B, Environmental* 39.1 (2002), pp. 1–37. ISSN: 0926-3373.
- [20] J. Chen et al. “Recent Advances in Catalysts for Methane Combustion”. eng. In: *Catalysis Surveys from Asia* 19.3 (2015), pp. 140–171. ISSN: 1571-1013.
- [21] F. F. Tao et al. “Understanding complete oxidation of methane on spinel oxides at a molecular level”. In: *Nature Communications* 6.1 (2015). ISSN: 2041-1723.
- [22] H. Li et al. “Catalytic Methane Combustion over $\text{Co}_3\text{O}_4/\text{CeO}_2$ Composite Oxides Prepared by Modified Citrate Sol–Gel Method”. eng. In: *Catalysis Letters* 141.3 (2011), pp. 452–458. ISSN: 1011-372X.
- [23] T. Montini et al. “Fundamentals and Catalytic Applications of CeO_2 -Based Materials”. In: *Chemical Reviews* 116.10 (2016), pp. 5987–6041. ISSN: 00092665.
- [24] K. S. Sing and R. T. Williams. “Physisorption Hysteresis Loops and the Characterization of Nanoporous Materials”. eng. In: *Adsorption Science & Technology* 22.10 (2004), pp. 773–782. ISSN: 0263-6174.
- [25] E. Tarleton. *Concepts of modern catalysis and kinetics*. Ed. by J. Niemantsverdriet. Wiley-VCH: Weinheim Germany, 2003.
- [26] G. Busca. *Heterogeneous Catalytic Materials: Solid State Chemistry, Surface Chemistry and Catalytic Behaviour*. eng. Elsevier, 2014. ISBN: 0444595244.
- [27] *New research trends of fluorite-based oxide materials : from basic chemistry and materials science to engineering applications*. eng. New York, 2015.
- [28] E. Marceau, X. Carrier, and M. Che. “Impregnation and Drying”. In: *Synthesis of Solid Catalysts*. Wiley-VCH Verlag GmbH & Co. KGaA, 2009, pp. 59–82. ISBN: 9783527320400.
- [29] N. J. Tro. *Chemistry : a molecular approach*. eng. Boston, 2011.
- [30] Y. Kamimura, M. Shimomura, and A. Endo. “Simple template-free synthesis of high surface area mesoporous ceria and its new use as a potential adsorbent for carbon dioxide capture”. eng. In: *Journal of Colloid And Interface Science* 436 (2014), pp. 52–62. ISSN: 0021-9797.
- [31] E. Marguá. *X-ray fluorescence spectrometry and related techniques : an introduction*. Ed. by R. Grieken. Momentum Press: New York, New York, 2013.
- [32] I. (Chorkendorff. *Concepts of modern catalysis and kinetics*. eng. Weinheim Germany2, 2003.
- [33] H. D. Young. *Sears and Zemansky’s University physics : with modern physics*. eng. 2015.

- [34] J. Niemantsverdriet. *Spectroscopy in Catalysis: An Introduction: Third Edition*. Wiley-VCH, 2007, pp. 1–325. ISBN: 9783527316519.
- [35] E. Tarleton. “Progress in filtration and separation”. In: (2015).
- [36] A. J. L et al. “Gas Chromatography: Theory and Definitions, Retention and Thermodynamics, and Selectivity”. eng. In: *Analytical Separation Science, 5 Volume Set*. John Wiley and Sons, 2015. ISBN: 9783527333745. URL: <https://app.knovel.com/hotlink/pdf/rcid:kpASSVS003/id:kt011CC9E1/analytical-separation/gas-chromatography-theory?kpromoter=Summon>.
- [37] H. M. McNair and J. M. Miller. *Basic Gas Chromatography*. eng. Hoboken, NJ, USA: John Wiley and Sons, Inc., 2008. ISBN: 9780470439548.
- [38] *Selecting a GC Column by a Specific Stationary Phase*. URL: <https://www.sigmaaldrich.com/technical-documents/articles/analytical-applications/gc/select-proper-stationary-phase-gc.html> (visited on 04/14/2020).
- [39] *MOLSIEVE 5 ÅNGSTRÖM PLOT COLUMNS*. URL: <http://www.chromedia.org/chromedia?waxtrapp=adwgrDsHqnOxmOIIeCbCsErD&subNav=tqfbmDsHqnOxmOIIeCbCsErDdB> (visited on 04/14/2020).
- [40] *Theory and Instrumentation of GC Introduction*. URL: https://www.chromacademy.com/lms/sco10/Theory_and_Instrumentation_Of_GC_Introduction.pdf (visited on 03/05/2020).
- [41] W. Matthias. “Thermogravimetric Analysis”. eng. In: *Thermal Analysis in Practice - Fundamental Aspects*. Hanser Publishers, 2018, pp. 1–1. ISBN: 9781569906439. URL: <https://app.knovel.com/hotlink/pdf/rcid:kpTAPFA001/id:kt011Q6SH1/thermal-analysis-in-practice/thermogravimetric-analysis?kpromoter=Summon>.
- [42] *TGA Beginners Guide*. URL: https://www.perkinelmer.com/CMSResources/Images/44-74556GDE_TGABeginnersGuide.pdf (visited on 02/14/2020).
- [43] A. Auroux. *Calorimetry and Thermal Methods in Catalysis*. eng. 1st ed.. Vol. 154. Springer Series in Materials Science Ser. 2013. ISBN: 9783642119545.
- [44] N. W. Hurst et al. “Temperature Programmed Reduction”. eng. In: *Catalysis Reviews* 24.2 (1982), pp. 233–309. ISSN: 0161-4940. URL: <http://www.tandfonline.com/doi/abs/10.1080/03602458208079654>.
- [45] *Calorimetry and Thermal Methods in Catalysis*. eng. Berlin, Heidelberg, 2013.
- [46] A. P. D. S. Peres et al. “Performance evaluation of NiCo₂O₄ spinel as a catalyst for partial oxidation of methane”. eng. In: *Matéria (Rio de Janeiro)* 24.1 (2019), p. 12313. ISSN: 1517-7076.

A. Catalyst Synthesis

In this appendix, equations related to catalyst synthesis as well as all the values used during the project can be viewed.

A.1. Calculation - IWI Impregnation Solution

$$m = n \cdot Mm \quad [g] \quad (A.1)$$

$$wt\% = \frac{m_{act.mat}}{m_{tot}} \cdot 100\% \quad (A.2)$$

Equation A.2 was used to calculate the amount of active material needed to meet the desired nominal weight percent.

$$m_{Ni} = \frac{wt\% * m_{CeO_2}}{3 * 100\%} \cdot \frac{1}{1 - \frac{wt\%}{100\%}} \quad [g] \quad (A.3)$$

Where:

- m_{CeO_2} is a known value.
- $wt\%$ is the desired weight percent of active material.
- and $m_{Co} = 2m_{Ni}$, which is based on the stoichiometric ratio of Ni to Co in $NiCo_2O_4$.

Further, the amount of nitrate needed to obtain the desired active material load can be calculated by combining the result from the expression A.3 with A.1, as shown in equation A.4.

$$m_{Ni-nitrate} = \frac{m_{Ni}}{Mm_{Ni}} \cdot Mm_{Ni-nitrate} \quad [g] \quad (A.4)$$

Due to the weighting of the material not always being correct in terms of the calculated value, the equation A.2 is used to correct the nominal weight percent. A calculation example is shown for sample 6.5NiCoO/CeO₂/H-S7, expression A.5. The values used for the calculation can be seen in table A.1.

$$\frac{0.178}{2.724} \cdot 100\% = 6.5\% \quad (A.5)$$

Table A.1.: Mass Ni, Co, and CeO₂ used for the synthesis of catalysts

ID S3-NiCo		
Substance	mass [g]	# mol
Ni(NO ₃) ₂ · 6 H ₂ O	0.269	0.001
Co(NO ₃) ₂ · 6 H ₂ O	0.527	0.002
Ni	0.054	0.001
Co	0.107	0.002
CeO ₂ /L	2.509	0.015
ID S4-NiCo		
Substance	mass [g]	# mol
Ni(NO ₃) ₂ · 6 H ₂ O	0.220	0.001
Co(NO ₃) ₂ · 6 H ₂ O	0.540	0.002
Ni	0.044	0.001
Co	0.109	0.002
CeO ₂ /L	2.563	0.015
S5-NiCo		
Substance	mass [g]	# mol
Ni(NO ₃) ₂ · 6 H ₂ O	0.292	0.001
Co(NO ₃) ₂ · 6 H ₂ O	0.573	0.002
Ni	0.059	0.001
Co	0.116	0.002
CeO ₂ /L	2.528	0.015
S6-NiCo		
Substance	mass [g]	# mol
Ni(NO ₃) ₂ · 6 H ₂ O	0.305	0.001
Co(NO ₃) ₂ · 6 H ₂ O	0.600	0.002
Ni	0.062	0.001
Co	0.121	0.002
CeO ₂ /L	2.593	0.015
S7-NiCo		
Substance	mass [g]	# mol
Ni(NO ₃) ₂ · 6 H ₂ O	0.295	0.001
Co(NO ₃) ₂ · 6 H ₂ O	0.583	0.002
Ni	0.060	0.001
Co	0.118	0.002
CeO ₂ /H	2.546	0.015

A.2. Deviation Between Nominal and Measured Mass Percentages

Equation A.6 was used to calculate the deviation between nominal mass percent and measured XRF value. A calculation example is shown for sample 6.5NiCoO/CeO₂/H-S7, table A.2, in expression A.7.

$$d = \frac{wt\%_1 - wt\%_2}{wt\%_2} \cdot 100 \% \quad (\text{A.6})$$

$$d = \frac{7.7 - 6.5}{6.5} \cdot 100 \% = 18.46\% \quad (\text{A.7})$$

Table A.2.: XRF analysis result of catalysts supported by high- and low surface area CeO₂.

ID	m [g]	wt % Ni	wt % Co	wt % Act
6.0NiCoO/CeO ₂ /L-S3	0.1008	1.5	2.7	4.2
6.0NiCoO/CeO ₂ /L-S3	0.105	1.5	2.7	4.3
6.0NiCoO/CeO ₂ /L-S3	0.1092	1.6	2.8	4.3
5.7NiCoO/CeO ₂ /L-S4	0.158	0.9	2.3	3.2
5.7NiCoO/CeO ₂ /L-S4	0.1129	0.8	2.1	2.9
5.7NiCoO/CeO ₂ /L-S4	0.1184	0.8	2.1	2.9
6.5NiCoO/CeO ₂ /L-S5	0.1046	2.5	4.6	7.0
6.6NiCoO/CeO ₂ /L-S6	0.1505	1.7	3.2	4.9
6.5NiCoO/CeO ₂ /H-S7	0.1106	2.9	4.8	7.7

B. Characterization

B.1. N₂ - Physisorption

Table B.1 contains the values used to generate the pore distribution plot which can be seen in Figure 4.1

Table B.1.: BJH: raw data from pore size investigation of CeO₂/H

Average Width (nm)	Incremental Pore Volume (cm ³ g ⁻¹)
S 253.0503325	0.002436887
200.1088515	0.003212959
156.6138819	0.003993512
130.5721851	0.002500549
117.471403	0.004571668
100.8664423	0.003518894
85.31066808	0.004567991
70.41193641	0.005061454
59.72376765	0.004243145
52.06451965	0.003506817
45.83084052	0.003288316
40.60983992	0.003412689
35.04306054	0.005952635
29.99051779	0.006089784
26.40816427	0.005153309
23.67107341	0.005210011
21.48528102	0.005012934
19.433	0.005905204
16.48344559	0.012052151
12.8443359	0.018509585
10.39455945	0.013131922
8.819189867	0.011119751
7.646939729	0.010336344
6.739474387	0.009816605
6.010814082	0.009479573
5.4148079	0.008958712
4.911018277	0.008445916
4.480031815	0.007815621
4.104915447	0.007203397
3.773685358	0.006755567
3.473668359	0.006366011
3.218075092	0.005222004
3.048703471	0.002750729
2.927117715	0.002666156
2.793121888	0.003183153
2.651151687	0.002973006
2.514440574	0.002812123
2.381408608	0.002663002
2.250480887	0.002278891
2.122761669	0.002068989
2.02207274	0.001162251
1.909029569	0.001067268
1.787511473	0.00055993

B.2. Raman

In the following section, Figure B.1-B.5 shows the Raman spectra for the catalysts: 6.0NiCoO/CeO₂/L-S3, 5.7NiCoO/CeO₂/L-S4, 6.6NiCoO/CeO₂/L-S6, 6.5NiCoO/CeO₂/L-S5 and 6.5NiCoO/CeO₂/H-S7.

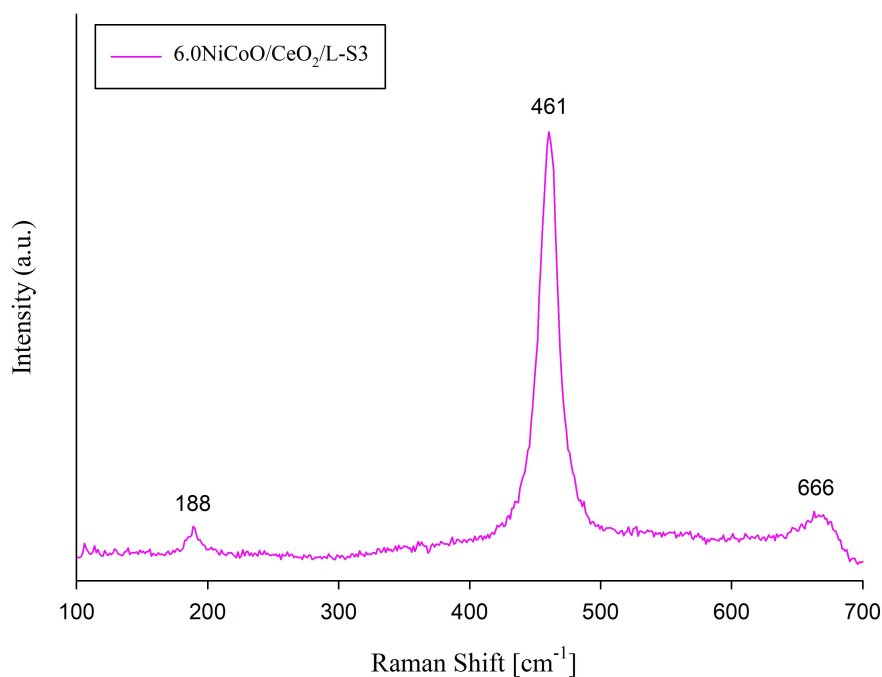


Figure B.1.: Raman spectrum of sample 6.0NiCoO/CeO₂/L-S3. Analysis parameters: Range = 100 - 3000 cm⁻¹, Accumulation = 4, Acc. Time = 4 min, Filter = 10 %, Hole = 200

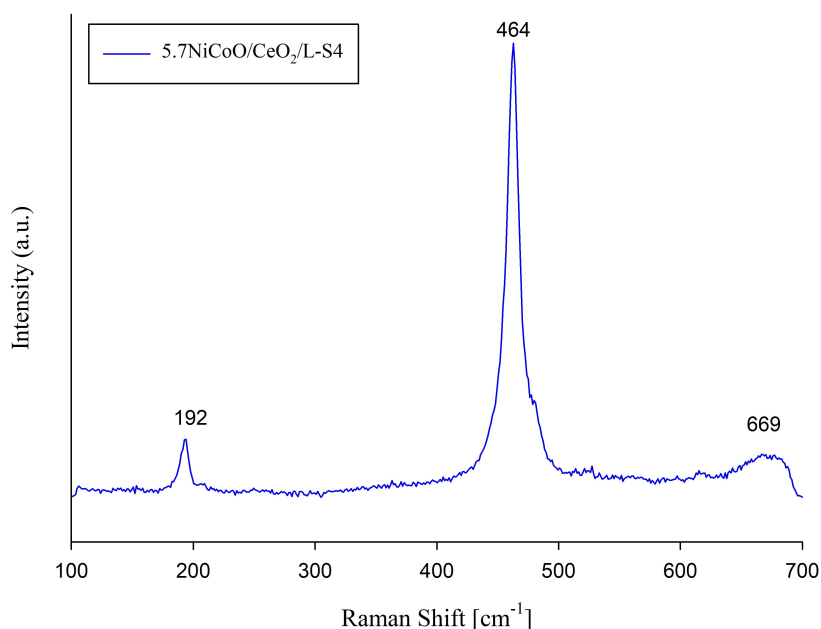


Figure B.2.: Raman spectrum of sample 5.7NiCoO/CeO₂/L-S4. Analysis parameters: Range = 100 - 3000 cm⁻¹, Accumulation = 4, Acc. Time = 4 min, Filter = 10 %, Hole = 200

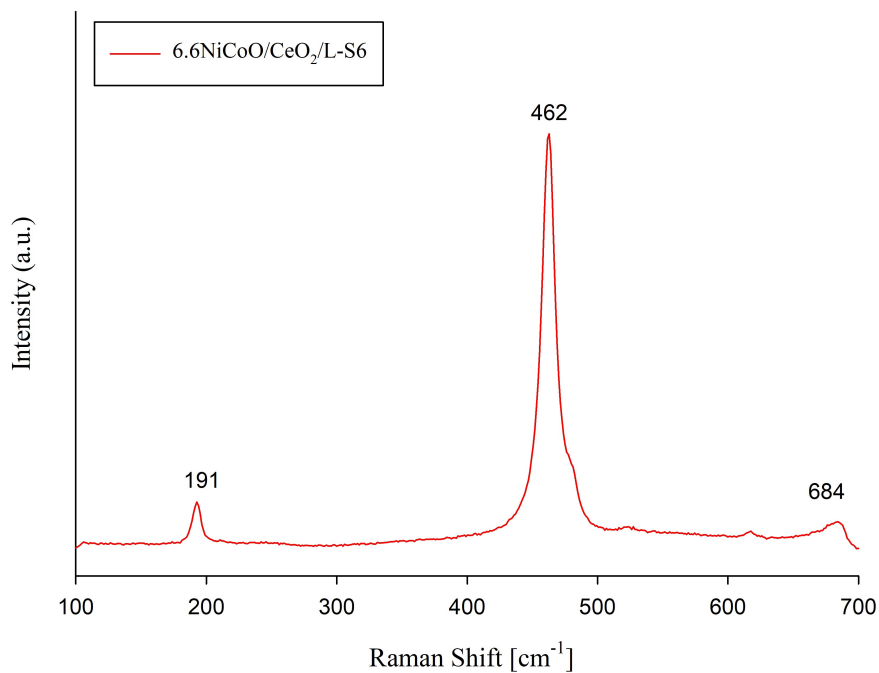


Figure B.3.: Raman spectrum of sample 6.6NiCoO/CeO₂/L-S6. Analysis parameters: Range = 100 - 3000 cm⁻¹, Accumulation = 4, Acc. Time = 4 min, Filter = 10 %, Hole = 200

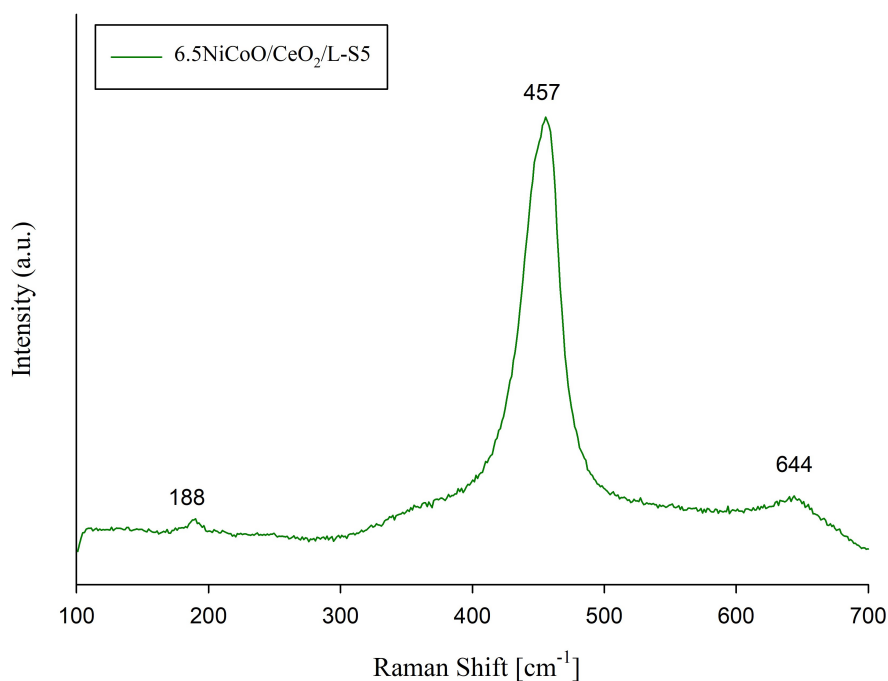


Figure B.4.: Raman spectrum of sample 6.5NiCoO/CeO₂/L-S5. Measurement parameters: Accumulation 4, Acc. Hour 4 min, filter 10 % and hole 200.

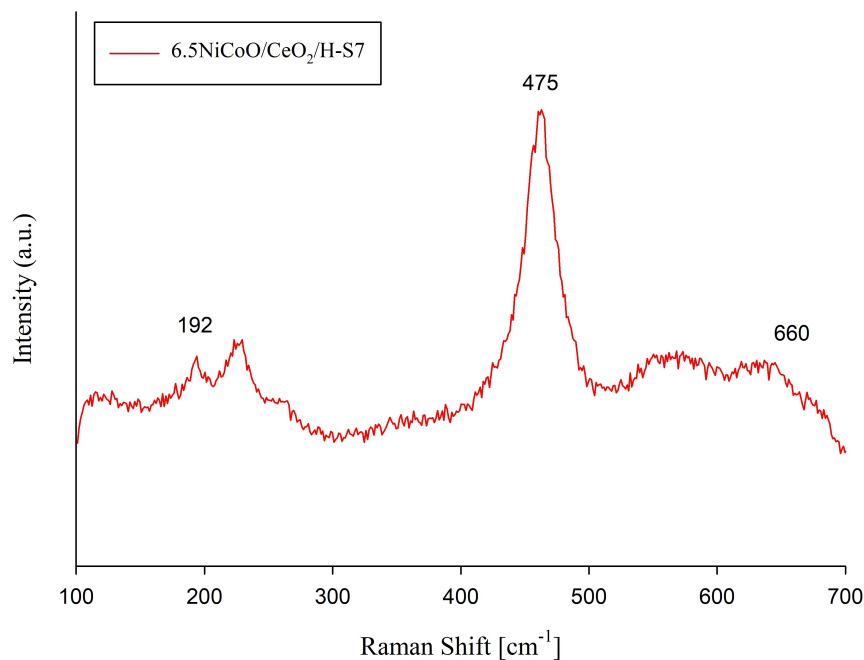


Figure B.5.: Raman spectrum of sample 6.5NiCoO/CeO₂/H-S7. Measurement parameters: Accumulation 4, Acc. Hour 4 min, filter 10 % and hole 200.

B.3. XRD

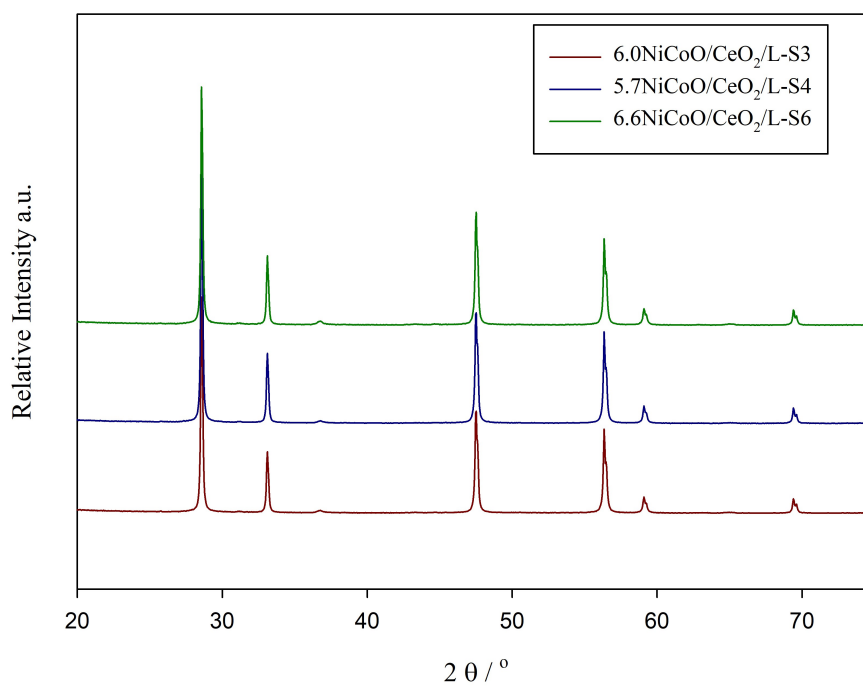


Figure B.6.: XRD spectre of 6.0NiCoO/CeO₂/L-S3, 5.7NiCoO/CeO₂/L-S4 and 6.6NiCoO/CeO₂/L-S6. Analysis parameters: $2\theta = 15-75^\circ$, time = 60 min, step change = $0.044^\circ\text{step}^{-1}$, permanent slit = 0.3 mm.

B.4. CeO₂ TPR-Profile

Figure B.7 contains the TPR profiles of CeO₂/H and CeO₂/L.

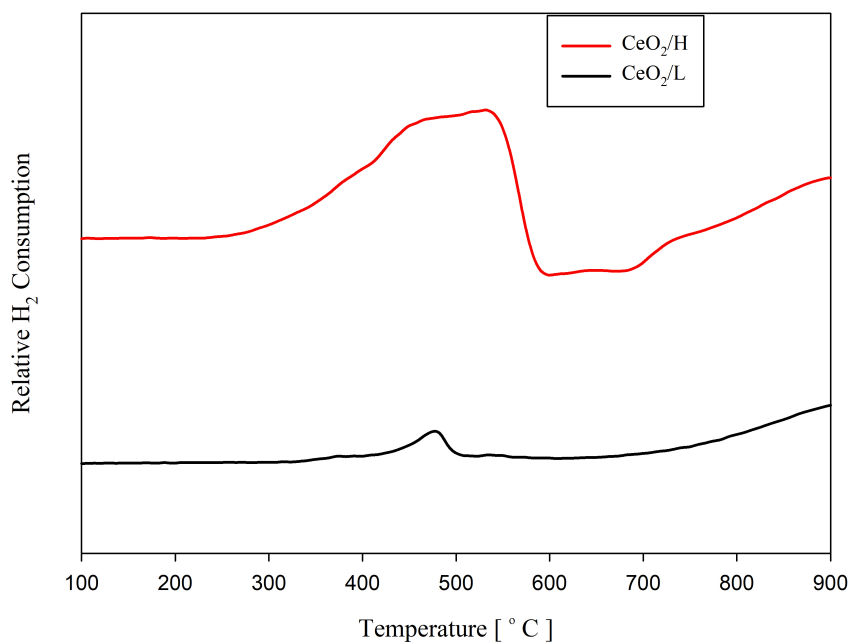


Figure B.7.: TPR-profile of high and low surface area CeO₂. Reaction conditions: H₂/Ar = 7 %, F_{H₂/Ar} = 20 ml min⁻¹, heating rate = 10 °C min⁻¹

C. Activity Tests

In following chapter reaction curves for catalysts supported by low surface area CeO_2 can be viewed. In addition, calculation of reaction rate and quantitative analysis can be reviewed.

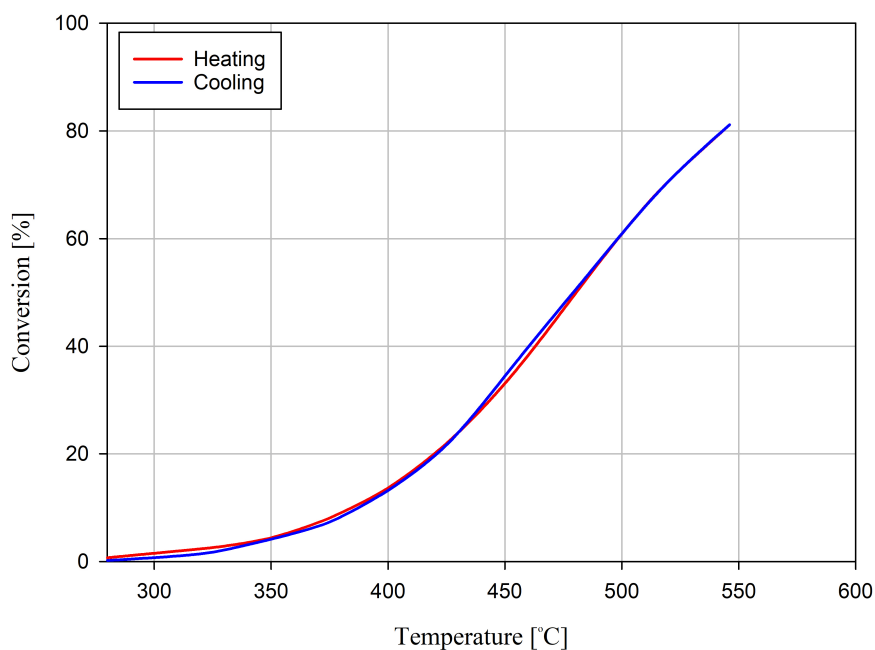


Figure C.1.: Methane conversion curve of sample 6.0NiCoO/CeO₂/L-S3. Reaction conditions: $F_{\text{CH}_4} = 4 \text{ ml min}^{-1}$, $F_{\text{N}_2} = 100 \text{ ml min}^{-1}$, $F_{\text{Air}} = 96 \text{ ml min}^{-1}$, amount of sample = 0.5074 g, $P = 1 \text{ bar}$.

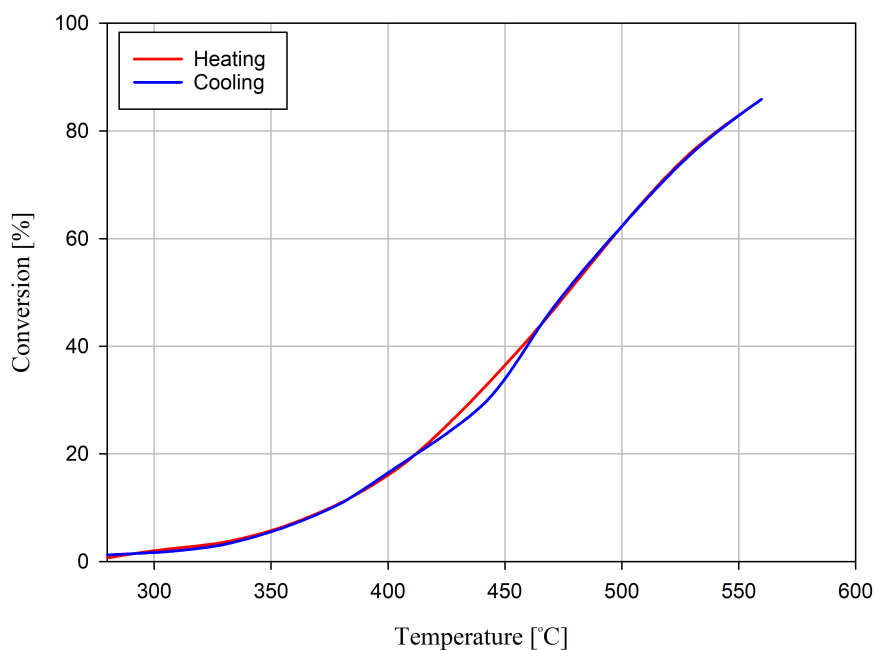


Figure C.2.: Reaction curve of catalyst 5.7NiCoO/CeO₂/L-S4. Reaction conditions: $F_{\text{CH}_4} = 4 \text{ ml min}^{-1}$, $F_{\text{N}_2} = 100 \text{ ml min}^{-1}$, $F_{\text{Air}} = 96 \text{ ml min}^{-1}$, amount of sample = 0.5035 g, $P = 1 \text{ bar}$.

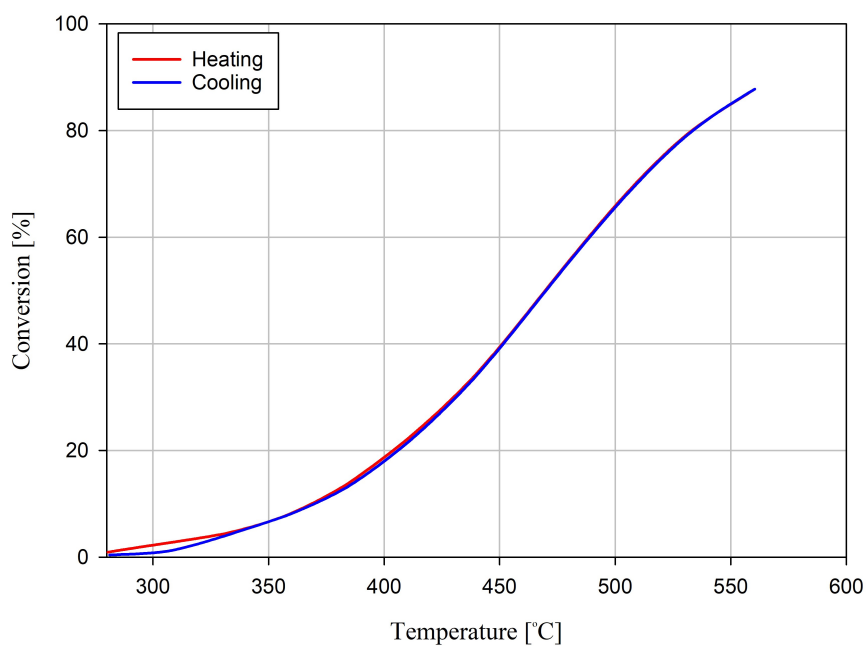


Figure C.3.: Reaction curve of catalyst 6.5NiCoO/CeO₂/L-S5. Reaction conditions: $F_{\text{CH}_4} = 4 \text{ ml min}^{-1}$, $F_{\text{N}_2} = 100 \text{ ml min}^{-1}$, $F_{\text{Air}} = 96 \text{ ml min}^{-1}$, amount of sample = 0.5012 g, $P = 1 \text{ bar}$.

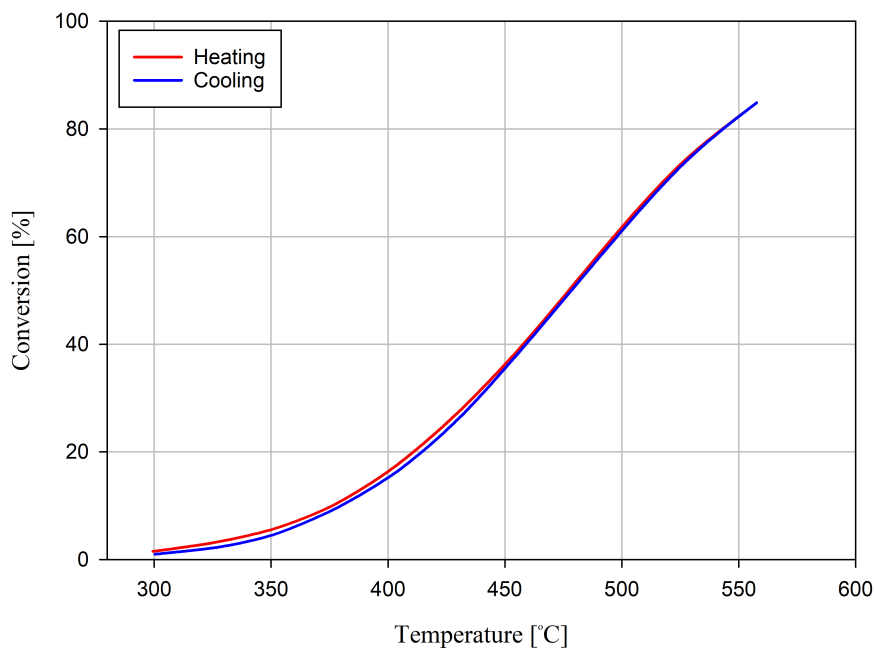


Figure C.4.: Methane conversion curve of sample 6.6NiCoO/CeO₂/L-S6. Reaction conditions: $F_{\text{CH}_4} = 4 \text{ ml min}^{-1}$, $F_{\text{N}_2} = 100 \text{ ml min}^{-1}$, $F_{\text{Air}} = 96 \text{ ml min}^{-1}$, amount of sample = 0.5009 g, $P = 1 \text{ bar}$.

C.1. H₂O Experiments

Figure C.5-C.7 shows the result from a long-term experiment conducted on two catalysts based on low surface area CeO₂/L, and from one based on high surface area CeO₂/H. In addition, a regression line was used to provide the relationship between conversion and time.

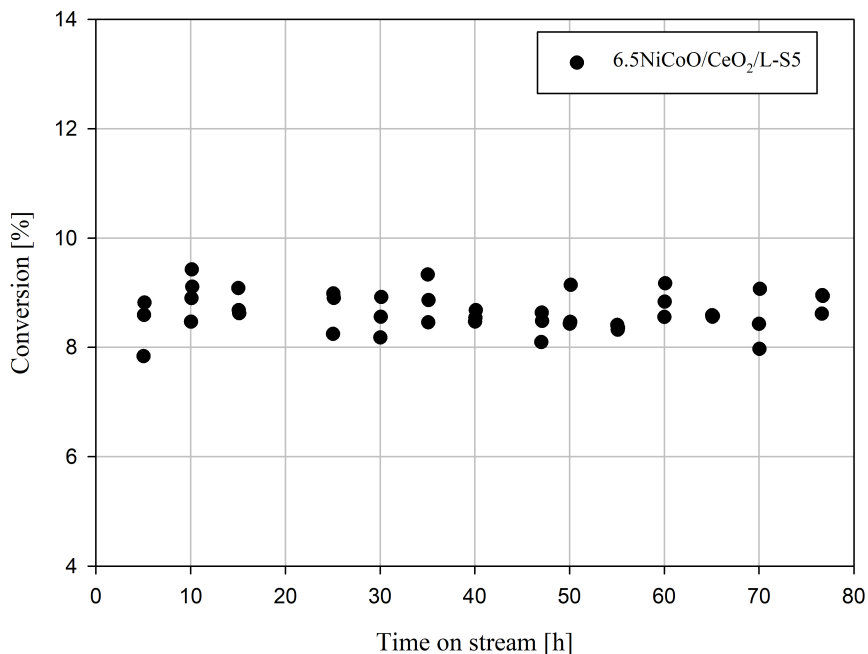


Figure C.5.: Long-term reaction 6.5NiCoO/CeO₂/L-S5. Reaction conditions: $F_{\text{CH}_4} = 4 \text{ ml min}^{-1}$, $F_{\text{N}_2} = 80 \text{ ml min}^{-1}$, $F_{\text{Air}} = 96 \text{ ml min}^{-1}$, $F_{\text{H}_2\text{O}} = 20 \text{ ml min}^{-1}$, amount of sample = 0.5051 g, proportion of active material = 0.033 g, $P = 1 \text{ bar}$, $T = 450 \text{ }^\circ\text{C}$.

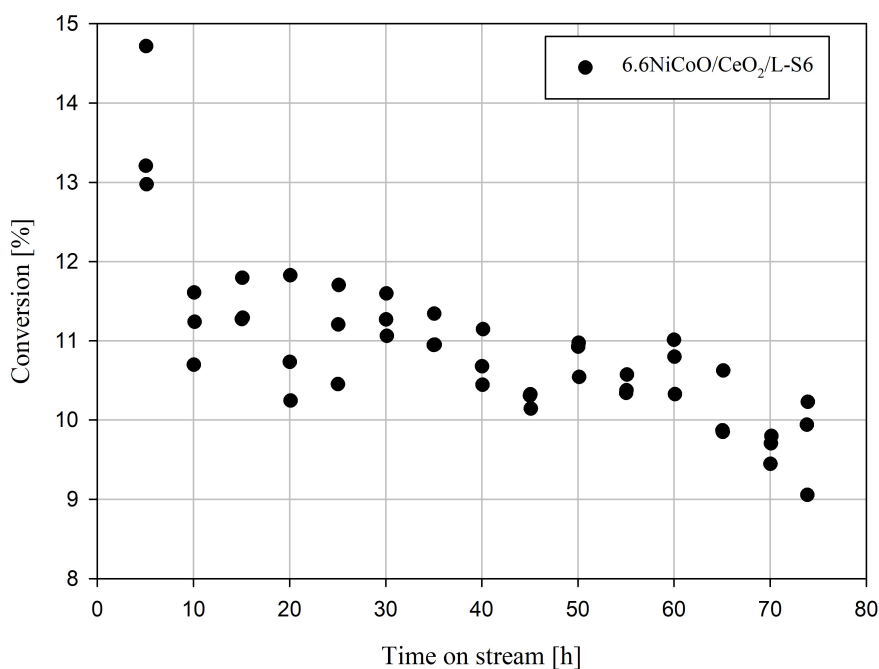


Figure C.6.: Long-term reaction 6.6NiCoO/CeO₂/L-S6. Reaction conditions: $F_{\text{CH}_4} = 4 \text{ ml min}^{-1}$, $F_{\text{N}_2} = 80 \text{ ml min}^{-1}$, $F_{\text{Air}} = 96 \text{ ml min}^{-1}$, $F_{\text{H}_2\text{O}} = 20 \text{ ml min}^{-1}$, amount of sample = 0.5036 g, proportion of active material = 0.033 g, $P = 1 \text{ bar}$, $T = 450 \text{ }^\circ\text{C}$.

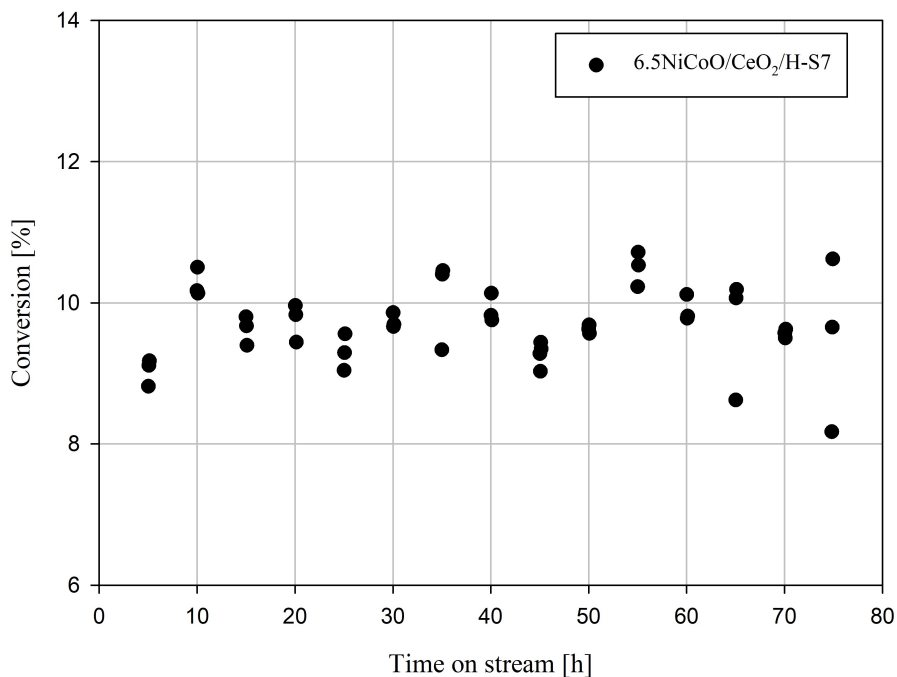


Figure C.7.: Long-term reaction 6.5NiCoO/CeO₂/H-S7. Reaction conditions: $F_{\text{CH}_4} = 4 \text{ ml min}^{-1}$, $F_{\text{N}_2} = 80 \text{ ml min}^{-1}$, $F_{\text{Air}} = 96 \text{ ml min}^{-1}$, $F_{\text{H}_2\text{O}} = 20 \text{ ml min}^{-1}$, amount of sample = 0.5060 g, proportion of active material = 0.033 g, $P = 1 \text{ bar}$, $T = 450 \text{ }^\circ\text{C}$.

C.2. Carbon Balance

The carbon plot of some of the samples synthesized is shown in figure C.8-C.10.

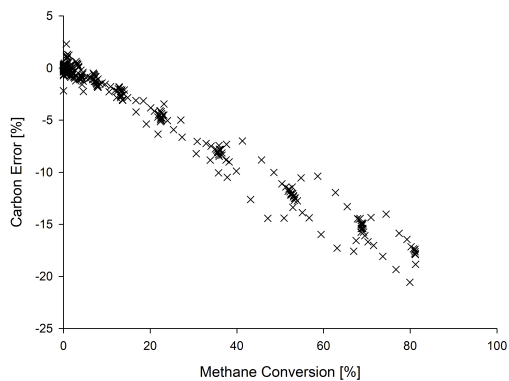


Figure C.8.: Carbon error sample 6.0NiCoO/CeO₂/L-S3.

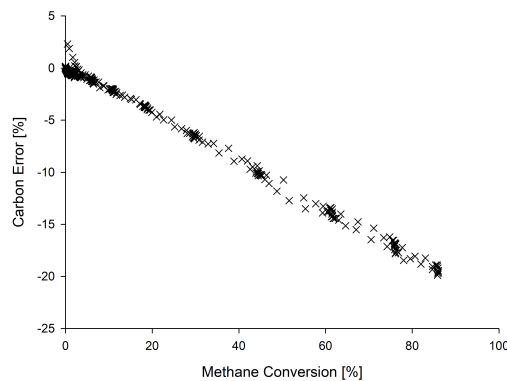


Figure C.9.: Carbon error sample 5.7NiCoO/CeO₂/L-S4.

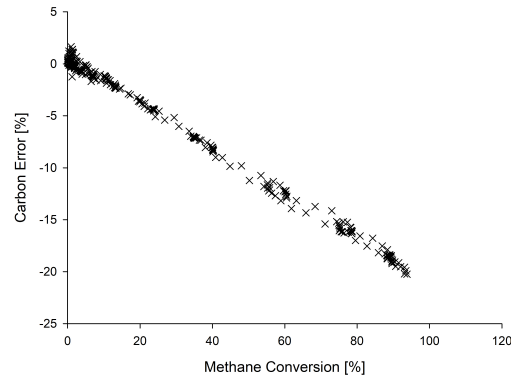


Figure C.10.: Carbon error sample
6.6NiCoO/CeO₂/L-S6.

C.3. Calculation of Reaction Rate and Quantitative Analysis

The following section shows the calculation of the reaction rate and the bulk activity pr. m² for the catalyst 6.5 NiCoO/CeO₂/H-S7. Further, some assumption considering S_{BET} were taken. For the catalysts supported on low surface area CeO₂, it were assumed that the S_{BET} of the catalyst 6.3NiCoO/CeO₂/L-S1 is representative of all the catalysts. In addition, the S_{BET} of high surface area catalyst is represented by the result obtained from a fresh specimen, regardless of the deactivation examination result.

Where:

- $\eta = 0.02$
- $X = 0.197$ at $T = 400$ [°C]
- $X = 0.451$ at $T = 450$ [°C]
- $m_{\text{act.m}} = 0.033$ [g]
- $m = 0.506$
- $S_{\text{BET}} = 100$ [m² g⁻¹]

$$\text{GHSW}_{\text{act} \cdot \text{m}} = \frac{12000}{0.033} = 363636 \text{ [ml h}^{-1}\text{g}_{\text{act} \cdot \text{cat}}^{-1}] \quad (\text{C.1})$$

For $T = 400$ [°C], the rate were calculated following:

$$r = \frac{363636}{22414} \cdot 0.02 \cdot 0.197 = 6.4 \cdot 10^{-2} \text{ [mol h}^{-1}\text{g}_{\text{act} \cdot \text{cat}}^{-1}] \quad (\text{C.2})$$

The bulk activity pr. m² at $T = 450$ [°C] were calculated following:

$$A = S_{\text{BET}} \cdot \frac{m}{m_{\text{act.m}}} = 100 \cdot \frac{0.506}{0.033} = 1533 \text{ [m}^2\text{ g}_{\text{act} \cdot \text{m}}] \quad (\text{C.3})$$

$$r_{\text{B}} = r \cdot \frac{1}{A} = 1.5 \cdot 10^{-1} \cdot \frac{1}{1533} = 9.6 \cdot 10^{-5} \text{ [mol m}^{-2}\text{ h}^{-1}] \quad (\text{C.4})$$

C.4. CeO₂ Blank Test and Activity Curve

Table C.1 and figure C.11 contain the results from the blank test of low surface area CeO₂.

Table C.1.: Reaction result from CeO₂/L test in rig 2.9. Reaction conditions: $F_{\text{CH}_4} = 4 \text{ ml min}^{-1}$, $F_{\text{N}_2} = 100 \text{ ml min}^{-1}$, $F_{\text{Air}} = 96 \text{ ml min}^{-1}$, amount of sample = 0.5000 g, $p = 1 \text{ bar}$.

Conversion _{Heating} [%]	T [°C]	Conversion _{Cooling} [%]	T [°C]
0	397.5	3.521	523.4
0.537	422.3	1.825	498.6
1.534	447.2	1.513	473.4
1.287	472.4	0.658	448.4
2.868	497.6	0.834	423.4
3.521	523.4	0.92	398.8

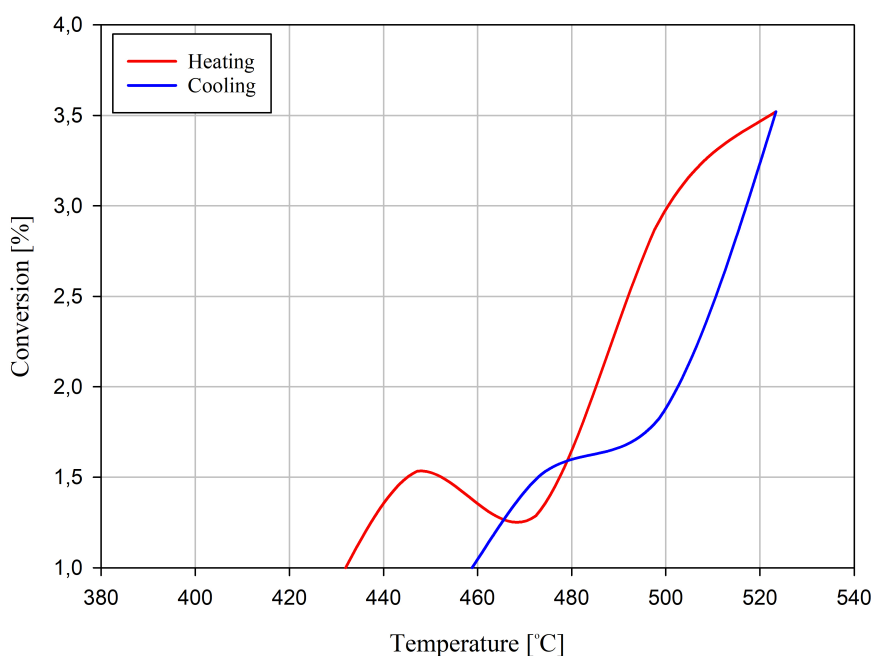


Figure C.11.: Methane conversion curve of low surface area CeO₂. Reaction conditions: $F_{\text{CH}_4} = 4 \text{ ml min}^{-1}$, $F_{\text{N}_2} = 100 \text{ ml min}^{-1}$, $F_{\text{Air}} = 96 \text{ ml min}^{-1}$, amount of sample = 0.5 g, $P = 1 \text{ bar}$.

D. Calibration Curve and Calculation of H₂O Flow

The calibration curve for LFC is shown in figure D.1, the values used for generating the plot can be seen in table D.1. Equation D.1 obtained from the calibration curve was used to calculate the H₂O flow.

$$F = 1.0584 \cdot Sp - 0.0298 \quad [\text{g h}^{-1}] \quad (\text{D.1})$$

Table D.1.: Calibration measurements obtained for LFC

Flow g h ⁻¹	Sp
0	0
0.44	0.5
1.06	1
1.56	1.5

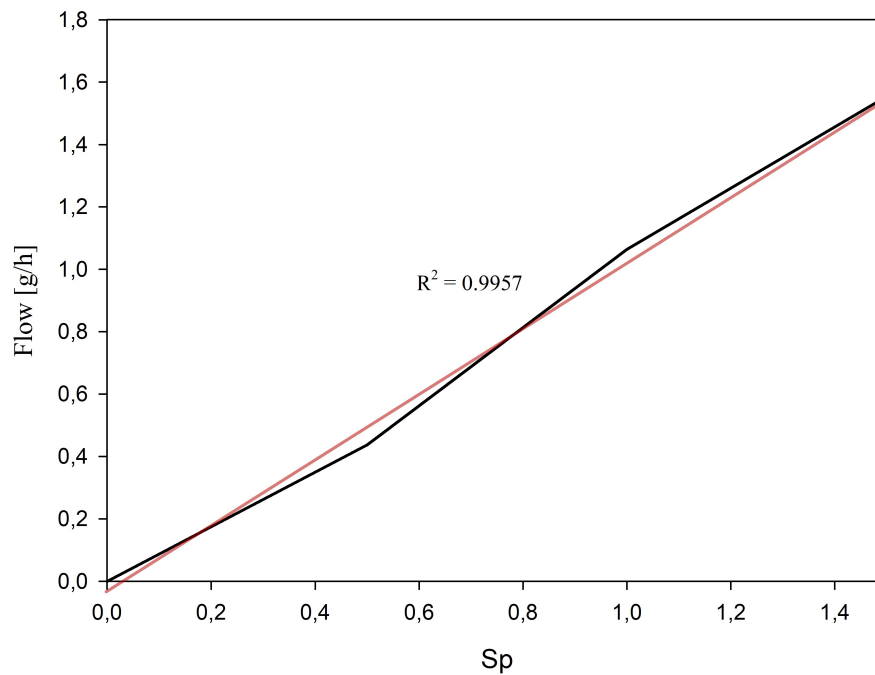


Figure D.1.: LFC calibration curve

E. MatLab Script

In the following section, the MatLab script for plotting conversion vs time and temperature vs time are showed.

```
-----  
clear all  
close all  
clc  
  
format long g  
  
[~,~,raw] = xlsread('file','Ark1','L4:M363');  
  
data = reshape([raw{:}],size(raw));  
  
time = data(:,2);  
Conv = data(:,1);  
  
figure(1)  
  
set(gcf,'color','w');  
plot(time,Conv,'b-','LineWidth',1)  
xlabel('\it Time t \rm / min')  
ylabel('\it Conversion \rm in %')  
-----  
  
-----  
clear all  
close all  
clc  
format long g  
[~,~,raw] = xlsread('file','Ark1','N2:O16321');  
  
data = reshape([raw{:}],size(raw));  
  
temp = data(:,2);  
conv = data(:,1);  
tempc = data(:,4);  
convc = data(:,3);
```

```
%conv_smooth=smooth(conv);
%convc_smooth = smooth(convc);
%plot(temp, conv_smooth); hold on
%plot(tempc, convc_smooth)

p = polyfit(temp,conv,6);
q = polyfit(tempc,convc,6);

T_plot = 234.0:0.1:565.1;
X_plot = polyval(p,T_plot);
T_plotc = 234:0.1:565.1;
X_plotc = polyval(q,T_plotc);
figure(1)
set(gcf,'color','w');
hold on
plot(temp,conv,'kx',...
T_plot,X_plot,'r-','linewidth',1);
plot(tempc,convc,'kx',...
T_plotc,X_plotc,'b-','linewidth',1)
xlabel('\it Temperature T \rm / min')
ylabel('\it Conversion X_C \rm / °C')
grid
legend('Experimental', ...
'Fitted Curve', ...
'Location', 'Northwest');
```

F. Risk Assessment

In the following chapter, the risk assessment conducted in relationship with the master thesis can be reviewed.



ID	34736	Status	Dato
Risikoområde	Risikovurdering: Helse, miljø og sikkerhet (HMS)	Opprettet	13.01.2020
Opprettet av	Jon Arve Selnes	Vurdering startet	13.01.2020
Ansvarlig	Jon Arve Selnes	Tiltak besluttet	
		Avsluttet	

Risikovurdering:**CAT_Master_student_2020_ Jon Arve Selnes**

Gyldig i perioden:

1/13/2020 - 12/18/2020

Sted:

Kjemi 5, Gløshaugen

Mål / hensikt

Development of catalysts intended for catalytic oxidation of methane from the exhaust gas (known as the methane slip).

BakgrunnChemical Engineering B.sc.
2nd year master student**Beskrivelse og avgrensninger**



Chemicals catalyst synthesis:
Ni(NO₃)₂·H₂O, Co(NO₃)₂·6H₂O, NaOH and Ceria

Catalyst synthesis:

Synthesis of NiCo₂O₄ are going to be performed at room temperature with Incipient wetness impregnation method.
Drying of catalyst at temperature between 40-130 °C for 24-48 h.

Calcination:

Calcination of the samples are going to be performed in a calcination oven at a temperature of 550°C. The catalyst is then sieved to obtain particles with a size of 200-400µm. If smaller particles are formed, they will be pelletized, crushed and sieved one more time to ensure the correct size. After the calcination step and the sieve step, the catalyst is tested within a fixed bed reactor that are feed with a diluted stream of CH₄, N₂ and air.

Catalyst characterization:

Methods: XRD, RAMAN, N₂-Physisorption, XRF, TPX

TPX:

H₂/Ar: 7% H₂ in Ar
Temt. prog. 200-1000 °C
Hall D

RAMAN:

Room K5-415

XRF:

Room K5-425

XRD:

Room K2-113

BET:

Room K5-425

Catalyst activity test rig 2.9 chemistry hall D:

- N₂, inert and support.
- CH₄ and air fuel for the reactor
- CO₂ and H₂O product gas
- H₂ for leak test
- He for GC

Parameters:

Pressure atm, Temperature 200-550 °C.
Temperature program Catalytic Testing: r.t.550°C with 5 K/min.

April-Mai 2020 - preventive measures towards Covid-situation

1) Switch off procedure for set-up rig 2.9 Hall D:

- Close all gas valves
- Turn off the heater
- Evacuate out through the nearest emergency exit

2) Risk related to shortage of personnel in the labs:

-When working alone, one must show caution to explosive gases such as H₂ and CH₄. Situations that can cause great danger to life and health must be avoided at all times.

3) Safety measures related to spread of covid19 infection:

- Avoid touching the face
- Disinfect all surfaces and especially common equipment before and after use. This applies to keyboards, computers, door handles and all other equipment as well as contact surfaces designed for the community.
- Keep 2m distance from colleagues
- Use nitrile gloves when touching shared lab set-ups and equipment
- Wash hands as often as possible

Forutsetninger, antakelser og forenklinger

The project will be a continuation of the work performed during the project " TKP 4580-Catalytic Methane Abatement for Natural Gas Engines ".

Vedlegg



CH4_en.pdf
He_en.pdf
Ni(NO3)2_en.pdf
O2_en.pdf
Co(NO3)2_en.pdf
CO2_en.pdf
Cu(NO3)2_en.pdf
HCl_en.pdf
H2O_en.pdf
Rig_2.9_Junbo_Jon.pdf

Referanser

[Ingen registreringer]

Oppsummering, resultat og endelig vurdering

I oppsummeringen presenteres en oversikt over farer og uønskede hendelser, samt resultat for det enkelte konsekvensområdet.

Farekilde: Catalyst synthesis

Uønsket hendelse: Ni(NO₃)₂

Konsekvensområde: Helse
Ytre miljø

Risiko før tiltak: Risiko etter tiltak:
Risiko før tiltak: Risiko etter tiltak:

Uønsket hendelse: Co(NO₃)₂

Konsekvensområde: Helse
Ytre miljø

Risiko før tiltak: Risiko etter tiltak:
Risiko før tiltak: Risiko etter tiltak:

Uønsket hendelse: NaOH

Konsekvensområde: Helse
Materielle verdier

Risiko før tiltak: Risiko etter tiltak:
Risiko før tiltak: Risiko etter tiltak:

Farekilde: TPX

Uønsket hendelse: Gas Leakage and Exposure of drierite during maintenance of the trap

Konsekvensområde: Helse
Materielle verdier

Risiko før tiltak: Risiko etter tiltak:
Risiko før tiltak: Risiko etter tiltak:

Farekilde: Raman

Uønsket hendelse: Eye damage due to laser scattering

Konsekvensområde: Helse

Risiko før tiltak: Risiko etter tiltak:

Farekilde: XRD

Uønsket hendelse: Chemical exposure during sample preparation

Konsekvensområde: Helse

Risiko før tiltak: Risiko etter tiltak:



Farekilde: XRF

Uønsket hendelse: Chemical exposure during sample preparation

Konsekvensområde: Helse

Risiko før tiltak:  Risiko etter tiltak: 

Farekilde: N2-Physisorption

Uønsket hendelse: Liquid N2-spill

Konsekvensområde: Helse

Risiko før tiltak:  Risiko etter tiltak: 

Farekilde: Rig 2.9



Uønsket hendelse: Gas leakage in the rig

Konsekvensområde: Helse
Materielle verdier

Risiko før tiltak:  Risiko etter tiltak: 
Risiko før tiltak:  Risiko etter tiltak: 

Uønsket hendelse: Skin burns

Konsekvensområde: Helse

Risiko før tiltak:  Risiko etter tiltak: 

Farekilde: Working in the lab during the covid-situation

Uønsket hendelse: Covid 19 infection

Konsekvensområde: Helse

Risiko før tiltak:  Risiko etter tiltak: 

Endelig vurdering

Involverte enheter og personer

En risikovurdering kan gjelde for en, eller flere enheter i organisasjonen. Denne oversikten presenterer involverte enheter og personell for gjeldende risikovurdering.

Enhet /-er risikovurderingen omfatter

- NTNU

Deltakere

Lesere

Hilde Johnsen Venvik

Jia Yang

Estelle Marie M. Vanhaecke

Andre involverte/interessenter

[Ingen registreringer]

Følgende akseptkriterier er besluttet for risikoområdet Risikovurdering: Helse, miljø og sikkerhet (HMS):

Helse



Materielle verdier



Omdømme



Ytre miljø



Oversikt over eksisterende, relevante tiltak som er hensyntatt i risikovurderingen

I tabellen under presenteres eksisterende tiltak som er hensyntatt ved vurdering av sannsynlighet og konsekvens for aktuelle uønskede hendelser.

Farekilde	Uønsket hendelse	Tiltak hensyntatt ved vurdering
Catalyst synthesis	Ni(NO ₃) ₂	Fume hood
	Ni(NO ₃) ₂	Lab coat
	Ni(NO ₃) ₂	Safety Goggles
	Ni(NO ₃) ₂	Gloves
	Co(NO ₃) ₂	Fume hood
	Co(NO ₃) ₂	Lab coat
	Co(NO ₃) ₂	Safety Goggles
	Co(NO ₃) ₂	Gloves
	NaOH	Fume hood
	NaOH	Lab coat
	NaOH	Safety Goggles
	NaOH	Gloves
TPX	Gas Leakage and Exposure of drierite during maintenance of the trap	Fume hood
	Gas Leakage and Exposure of drierite during maintenance of the trap	Lab coat
	Gas Leakage and Exposure of drierite during maintenance of the trap	Safety Goggles
	Gas Leakage and Exposure of drierite during maintenance of the trap	Gloves
	Gas Leakage and Exposure of drierite during maintenance of the trap	Closed Rig with ventilation
	Gas Leakage and Exposure of drierite during maintenance of the trap	Gas detector
	Gas Leakage and Exposure of drierite during maintenance of the trap	Leak detection spray
Raman	Eye damage due to laser scattering	
XRD	Chemical exposure during sample preparation	Fume hood
	Chemical exposure during sample preparation	Lab coat
	Chemical exposure during sample preparation	Safety Goggles
	Chemical exposure during sample preparation	Gloves
XRF	Chemical exposure during sample preparation	Fume hood
	Chemical exposure during sample preparation	Lab coat
	Chemical exposure during sample preparation	Safety Goggles



XRF	Chemical exposure during sample preparation	Gloves
N2-Physisorption	Liquid N2-spill	Lab coat
	Liquid N2-spill	Safety Goggles
	Liquid N2-spill	Gloves
Rig 2.9	Gas leakage in the rig	Safety Goggles
	Gas leakage in the rig	Closed Rig with ventilation
	Gas leakage in the rig	Gas detector
	Gas leakage in the rig	Leak detection spray
	Skin burns	Lab coat
	Skin burns	Safety Goggles
	Skin burns	Gloves
Working in the lab during the covid-situation	Covid 19 infection	Gloves

Eksisterende og relevante tiltak med beskrivelse:**Fume hood**

[Ingen registreringer]

Lab coat

[Ingen registreringer]

Safety Goggles

[Ingen registreringer]

Gloves

[Ingen registreringer]

Closed Rig with ventilation

[Ingen registreringer]

Gas detector

[Ingen registreringer]

Leak detection spray

[Ingen registreringer]

Risikoanalyse med vurdering av sannsynlighet og konsekvens

I denne delen av rapporten presenteres detaljer dokumentasjon av de farer, uønskede hendelser og årsaker som er vurdert. Innledningsvis oppsummeres farer med tilhørende uønskede hendelser som er tatt med i vurderingen.

Følgende farer og uønskede hendelser er vurdert i denne risikovurderingen:

- **Catalyst synthesis**
 - Ni(NO₃)₂
 - Co(NO₃)₂
 - NaOH
- **TPX**
 - Gas Leakage and Exposure of drierite during maintenance of the trap
- **Raman**
 - Eye damage due to laser scattering
- **XRD**
 - Chemical exposure during sample preparation
- **XRF**
 - Chemical exposure during sample preparation
- **N₂-Physisorption**
 - Liquid N₂-spill
- **Rig 2.9**
 - Gas leakage in the rig
 - Skin burns
- **Working in the lab during the covid-situation**
 - Covid 19 infection

Detaljert oversikt over farekilder og uønskede hendelser:

Farekilde: Catalyst synthesis

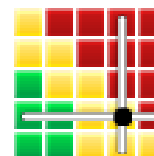
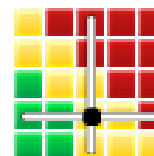
Uønsket hendelse: Ni(NO₃)₂

Spill and inhalation of Ni(NO₃)₂

Sannsynlighet for hendelsen (felles for alle konsekvensområder):

Lite sannsynlig (2)*Kommentar:*

The likelihood is low due to the provided measures. Lab coat, safety goggles and gloves will protect the skin and the eyes from a spill. Working in a fume hood will protect against the vapour.

Konsekvensområde: HelseVurdert konsekvens: **Svært stor (4)***Kommentar:* Inhalation of the chemical may cause cancer, and the substance is harmful for the skin.**Risiko:****Konsekvensområde: Ytre miljø**Vurdert konsekvens: **Stor (3)***Kommentar:* Very harmful for the environment.**Risiko:****Uønsket hendelse: Co(NO₃)₂**

Spill or inhalation

Sannsynlighet for hendelsen (felles for alle konsekvensområder):

Lite sannsynlig (2)*Kommentar:*

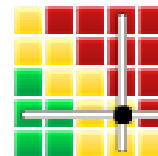
The likelihood is low due to the provided measures. Lab coat, safety goggles and gloves will protect the skin and the eyes from a spill. Working in a fume hood will protect against the vapour.

Konsekvensområde: HelseVurdert konsekvens: **Stor (3)***Kommentar:* The compound is harmful for the skin, and it could be harmful if swallowed. Inhalation of the chemical may cause cancer**Risiko:**

Konsekvensområde: Ytre miljø

Vurdert konsekvens: **Svært stor (4)**

Kommentar: The substance is very harmful for the environment.

Risiko:**Uønsket hendelse: NaOH**

Sannsynlighet for hendelsen (felles for alle konsekvensområder):

Svært lite sannsynlig (1)

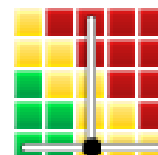
Kommentar:

When protective work clothes, gloves and goggles are used, the damage risk will be reduced. If glassware is avoided, the risk of decomposition of the equipment is eliminated. In case of spillage dilute with water.

Konsekvensområde: Helse

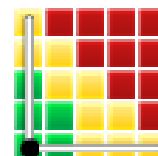
Vurdert konsekvens: **Stor (3)**

Kommentar: The substance can cause severe skin burns and eye damage.

Risiko:**Konsekvensområde: Materielle verdier**

Vurdert konsekvens: **Liten (1)**

Kommentar: Strong NaOH decomposes glass

Risiko:



Farekilde: TPX

Uønsket hendelse: Gas Leakage and Exposure of drierite during maintenance of the trap

Sannsynlighet for hendelsen (felles for alle konsekvensområder): **Svært lite sannsynlig (1)**

Kommentar:

The likelihood are kept low because of the provided measures. Working inside a fume hood reduces the risk of inhalation of the chemical. When a bucket are used to transport the trap, the risk of spilling is reduced and also exposure of the chemical. The rig has fixed ventilation that dilutes the gas if there is any leakage.

Konsekvensområde: Helse

Vurdert konsekvens: **Svært stor (4)**

Kommentar: The chemical are cancerogenic. Gas leakage in the rig can lead to an explosion. In worst case an explosion could be lethal.

Risiko:

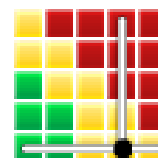


Konsekvensområde: Materielle verdier

Vurdert konsekvens: **Svært stor (4)**

Kommentar: The rig or other equipment can be damaged/destroyed.

Risiko:



Farekilde: Raman

Uønsket hendelse: Eye damage due to laser scattering

Sannsynlighet for hendelsen (felles for alle konsekvensområder): **Svært lite sannsynlig (1)**

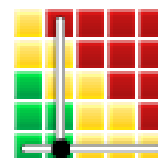
Kommentar:

This event can be avoided simply by not looking directly into the laser beam, or wearing protective goggles.

Konsekvensområde: Helse

Vurdert konsekvens: **Middels (2)**

Kommentar: The laser beam will not kill you, but it can harm the eyes and in worst case cause blindness.

Risiko:



Farekilde: XRD

Uønsket hendelse: Chemical exposure during sample preparation

Sannsynlighet for hendelsen (felles for alle konsekvensområder): **Svært lite sannsynlig (1)**

Kommentar:

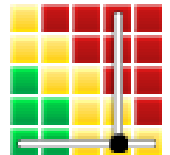
The likelihood are kept low because of the provided measures.

Konsekvensområde: Helse

Vurdert konsekvens: **Svært stor (4)**

Kommentar: The chemicals are canerogenic

Risiko:





Farekilde: XRF

Uønsket hendelse: Chemical exposure during sample preparation

Sannsynlighet for hendelsen (felles for alle konsekvensområder): **Svært lite sannsynlig (1)**

Kommentar:

The likelihood is low due to the provided measures. Working in a fume hood reduces the risk of inhalation and exposure.

Konsekvensområde: Helse

Vurdert konsekvens: **Svært stor (4)**

Kommentar: The chemicals are cancerogenic

Risiko:



**Farekilde: N2-Physisorption**

Uønsket hendelse: Liquid N2-spill

Sannsynlighet for hendelsen (felles for alle konsekvensområder): **Svært lite sannsynlig (1)**

Kommentar:

The likelihood are kept low because the provided measures

Konsekvensområde: Helse

Vurdert konsekvens: **Stor (3)**

Kommentar: Liquid N2 can scan cause serious harm to the skin/eyes, but exposure will probably not be deadly.

Risiko:



Farekilde: Rig 2.9

Uønsket hendelse: Gas leakage in the rig

Sannsynlighet for hendelsen (felles for alle konsekvensområder): **Svært lite sannsynlig (1)**

Kommentar:

The likelihood is kept low because of the provided measures. The gas detector and the leak detection spray will provide information about any leak. The ventilation system in the rig will ensure a low gas concentration if the rig has any leaks

Konsekvensområde: Helse

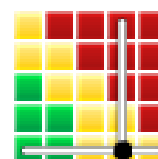
Vurdert konsekvens: **Katastrofal (5)**

Kommentar: The gas is extremely flammable, and it can explode if the conditions are right. In worst case this is lethal

Risiko:**Konsekvensområde: Materielle verdier**

Vurdert konsekvens: **Svært stor (4)**

Kommentar: A explosion in the rig due to a gas leak will destroy the equipment

Risiko:**Uønsket hendelse: Skin burns**

Sannsynlighet for hendelsen (felles for alle konsekvensområder): **Svært lite sannsynlig (1)**

Kommentar:

When working with equipment that have a high temperature, the provided measures should be used. This will reduce the likelihood of getting an injury from any hot surface

Konsekvensområde: Helse

Vurdert konsekvens: **Stor (3)**

Kommentar: Extent of injury is dependent on temperature, and exposure time.

Risiko:

Farekilde: Working in the lab during the covid-situation

Uønsket hendelse: Covid 19 infection

Infection of Covid 19 as a result of work done at a laboratory at NTNU.

Sannsynlighet for hendelsen (felles for alle konsekvensområder): **Lite sannsynlig (2)**

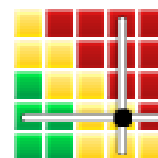
Kommentar:

The risk of being infected by Covid 19 by performing laboratory work is considered low. This is justified by the introduced measures that entail very limited contact with other persons working at NTNU. Keeping at least 2 m distance as well as washing hands and disinfecting all contact surfaces regularly reduces the risk of infection.

Konsekvensområde: Helse

Vurdert konsekvens: **Svært stor (4)**

Kommentar: For younger people with no underlying diseases, the risk of a Covid 19 infection is considered not harmful. The opposite applies to older people, as well as people with underlying illnesses such as high blood pressure or asthma. In a worst case scenario, a Covid 19 infection in such cases can be fatal.

Risiko:



Oversikt over besluttede risikoreducerende tiltak:

Under presenteres en oversikt over risikoreducerende tiltak som skal bidra til å reduseres sannsynlighet og/eller konsekvens for uønskede hendelser.

Detaljert oversikt over besluttede risikoreducerende tiltak med beskrivelse:



Detaljert oversikt over vurdert risiko for hver farekilde/uønsket hendelse før og etter besluttede tiltak